Evaluating the consistency between OCO-2 and OCO-3 XCO$_2$ estimates derived from the NASA ACOS version 10 retrieval algorithm

Thomas E. Taylor[1], Christopher W. O'Dell[1], David Baker[1], Carol Bruegge[2], Albert Chang[2], Lars Chapsky[2], Abhishek Chatterjee[2], Cecilia Cheng[2], Frédéric Chevallier[3], David Crisp[2], Lan Dang[2], Brian Drouin[2], Annmarie Eldering[2], Liang Feng[4], Brendan Fisher[2], Dejian Fu[2], Michael Gunson[2], Vance Haemmerle[2], Graziela R. Keller[2], Matthäus Kiel[2], Le Kuai[2], Thomas Kurosu[2], Alyn Lambert[2], Joshua Laughner[2], Richard Lee[2], Junjie Liu[2], Lucas Mandrake[2], Yuliya Marchetti[2], Gregory McGarragh[1], Aronne Merrelli[5], Robert R. Nelson[2], Greg Osterman[2], Fabiano Oyafuso[2], Paul I. Palmer[4], Vivienne H. Payne[2], Robert Rosenberg[2], Peter Somkuti[6], Gary Spiers[2], Cathy To[2], Brad Weir[7], Paul O. Wennberg[8], Shanshan Yu[2], and Jia Zong[2]

[1]Cooperative Institute for Research in the Atmosphere, Colorado State University, Fort Collins, CO, USA
[2]Jet Propulsion Laboratory, California Institute of Technology, Pasadena, CA, USA
[3]Laboratoire des Sciences du Climat et de l'Environnement/IPSL, CEA-CNRS-UVSQ, Université Paris-Saclay, 91198 Gif-sur-Yvette, France
[4]National Centre for Earth Observation, University of Edinburgh, Edinburgh, UK
[5]University of Michigan, Ann Arbor, MI, USA
[6]University of Oklahoma, Norman, OK, USA
[7]Morgan State University, Baltimore, Maryland and NASA Goddard Space Flight Center, Greenbelt, Maryland
[8]California Institute of Technology, Pasadena, CA, USA

Correspondence: Tommy Taylor (tommy.taylor@colostate.edu)

Abstract. The version 10 (v10) Atmospheric Carbon Observations from Space (ACOS) Level 2 Full Physics (L2FP) retrieval algorithm has been applied to multi-year records of observations from NASA's Orbiting Carbon Observatory -2 and -3 sensors (OCO-2 and OCO-3, respectively) to provide estimates of the carbon dioxide (CO$_2$) column-averaged dry-air mole fraction (XCO$_2$). In this study, a number of improvements to the ACOS v10 L2FP algorithm are described. The post-processing qual-
5 ity filtering and bias correction of the XCO$_2$ estimates against multiple truth proxies are also discussed. The OCO v10 data volumes and XCO$_2$ estimates from the two sensors for the time period August 2019 through February 2022 are compared, highlighting differences in spatiotemporal sampling, but demonstrating broad agreement between the two sensors where they overlap in time and space. A number of evaluation sources applied to both sensors suggest they are broadly similar in data and error characteristics. Mean OCO-3 differences relative to collocated OCO-2 data are approximately 0.2 ppm and -0.3 ppm
10 for land and ocean observations, respectively. Comparison of XCO$_2$ estimates to collocated Total Carbon Column Observing Network (TCCON) measurements show root mean squared errors (RMSE) of approximately 0.8 ppm and 0.9 ppm for OCO-2 and OCO-3, respectively. An evaluation against XCO$_2$ fields derived from atmospheric inversion systems that assimilated only near-surface CO$_2$ observations, i.e., did not assimilate satellite CO$_2$ measurements, yielded RMSEs of 1.0 ppm and 1.1 ppm for OCO-2 and OCO-3, respectively. Evaluation of uncertainties in XCO$_2$ over small areas, as well as XCO$_2$ biases across

land-ocean crossings, also indicate similar behavior in the error characteristics of both sensors. Taken together, these results demonstrate a broad consistency of OCO-2 and OCO-3 XCO_2 measurements, suggesting they may be used together for scientific analyses.

1 Introduction

Estimates of the column-averaged carbon dioxide (CO_2) dry air mole fraction (XCO_2) derived from global space-based measurements can be assimilated into atmospheric inversion systems to quantify CO_2 fluxes associated with both natural and anthropogenic sources and sinks (Gurney et al., 2002). However, these estimates must have both high precision and accuracy due to the long atmospheric lifetime of CO_2 (Archer et al., 2009), and the high background concentrations (≈ 415 parts per million by volume, ppm, in 2022), such that even the most intense sources and sinks produce only small (≈ 1 ppm) changes in XCO_2 (Miller et al., 2007).

The Orbiting Carbon Observatory -2 and -3 missions, OCO-2 and OCO-3, respectively, referred to collectively as OCO in this document, are NASA's primary operating assets for monitoring CO_2 concentrations from space. Both of these instruments measure reflected solar radiation at high spectral resolution in specific narrow spectral bands in the near and short-wave infrared regions (NIR and SWIR, respectively), where molecular oxygen (O_2) and CO_2 absorb sun light. A variety of physics based algorithms and sources of prior information are required to convert the measured spectra into estimates of XCO_2 in a series of steps. First, the individual soundings are geolocated and then radiometrically and spectrally calibrated. Then, these products are pre-screened to filter out scenes contaminated by clouds and heavy aerosol loading. A retrieval is then performed to estimate XCO_2 from the geolocated and calibrated radiances. Finally, a post-processing step is applied that quality screens the retrieval output and applies an empirically-based bias correction to the XCO_2 concentrations. Although estimates of solar-induced chlorophyll fluorescence (SIF) are also provided from OCO-2 and OCO-3 measurements, the focus of this paper is on the XCO_2 estimates. Readers are referred to Doughty et al. (2022) for an overview of the OCO SIF products.

Space-based measurements from OCO-2 and OCO-3 have already been successfully used to quantify CO_2 sources and sinks at global (e.g., Crowell et al., 2019; Peiro et al., 2022; Byrne et al., 2023), regional (e.g., Palmer et al., 2019; Byrne et al., 2021; Philip et al., 2022) and even local/urban scales (e.g., Lei et al., 2021; Kiel et al., 2021; Nassar et al., 2022). However, biases and random errors in the XCO_2 estimates relative to reference measurements persist, even after application of bias correction and filtering. These biases and random errors are associated with multiple factors, such as instrument measurement noise, uncertainties in instrument calibration, error in CO_2 and O_2 gas absorption cross sections, complications in accurately representing aerosols and surface characteristics in the retrieval, and lack of accurate knowledge of the prior estimates of the atmospheric state that are used in the retrieval algorithm (Connor et al., 2016; Kulawik et al., 2016; Hobbs et al., 2017; Kulawik et al., 2019). Numerous studies have demonstrated that small, but regionally coherent, biases in CO_2 concentrations can result

in flux estimate errors (e.g., Chevallier et al., 2005, 2007, 2014; Basu et al., 2013; Feng et al., 2016). It is therefore essential to quantify, as best as possible, the remaining biases present in the satellite XCO_2 products.

The paper is organized as follows: The OCO instruments, spectral measurements, and calibration are reviewed in Section 2. Section 3 discusses updates to the v10 L2FP retrieval algorithm and other components of the data processing pipeline. In Section 4, the OCO-2 and OCO-3 v10 XCO_2 data volumes are analyzed for the overlapping time period August 2019 through February 2022, while Section 5 compares the XCO_2 estimates from the two sensors. Section 6 compares the satellite XCO_2 estimates from both sensors to XCO_2 estimates derived from Total Carbon Column Observing Network (TCCON), atmospheric inversion systems (models), as well as to small areas and coastal crossings. A summary of the findings are presented in Section 7. A deeper examination of the full 7+ year OCO-2 v10 record is provided in Appendix A. Finally, in Appendix B, several aspects of the OCO-3 v10 data set are explored in detail, including the application of a time-dependent correction to the OCO-3 v10 XCO_2 estimates to correct a calibration artifact using a set of soundings collocated to OCO-2.

2   The OCO-2 and OCO-3 instruments and calibration

There are many similarities between the OCO-2 and OCO-3 sensors, as the latter was built as a flight spare for the former. Both are three-channel grating spectrometers with a common telescope used to direct reflected solar radiation from the field of view through a dispersion grating onto a focal plane array (FPA). The FPA electronics convert analog signals into measured digital numbers (DN). Predetermined calibration information is used to convert DN into radiances (photons s^{-1} m^{-2} sr^{-1} μm^{-1}) in the three spectral channels: (i) the Oxygen-A band centered at $0.765\,\mu m$, (ii) a weak CO_2 band centered at $1.61\,\mu m$, and (iii) a strong CO_2 band centered at $2.06\,\mu m$, referred to as the ABO2, WCO2, and SCO2, respectively, all with high spectral resolving power ($\lambda/\Delta\lambda > 17,000$) and 1016 spectral channels. A single OCO-2/3 measurement frame contains 8 along-slit "footprints", which are acquired at 3 Hz, yielding 24 individual soundings per second. The exact footprint size of each OCO-2 sounding varies by observation mode and latitude, but is of order 1.3 km cross-track and 2.25 km along-track ($2.9\,km^2$) near nadir viewing. The orbit altitude of OCO-3 aboard the International Space Station (ISS) is lower than that of OCO-2 ($\approx 400\,km$ and $\approx 705\,km$ for OCO-3 and OCO-2, respectively), necessitating an enlargement of the instrument's field of view from $0.8°$ to $1.8°$ in order to maintain a similar footprint size. Even so, OCO-3 footprints are typically slightly larger, at 1.6 km cross-track by 2.2 km along-track ($3.5\,km^2$).

75

OCO-2 began science operations in September, 2014 (Crisp et al., 2017; Eldering et al., 2017). It flies in a sun-synchronous polar orbit on a dedicated satellite bus in the Afternoon constellation, i.e., A-train (L'Ecuyer and Jiang, 2010), which has a local overpass time of approximately 13:36 and a 16-day orbit repeat cycle. OCO-2 science measurements are made in one of three observation modes: (i) down-looking nadir (ND), (ii) sun-glint (GL), or (iii) target (TG). For routine science observations, a full day-side orbit is acquired in one of the two primary observation modes (nadir or glint), in an alternating fashion. However,

for orbits that pass largely over ocean, the satellite orients the instrument to view the sun's specular glint spot, which maximizes the signal over water (Miller et al., 2007). In addition, a small number (order 30) of pre-determined target sites are viewed as conditions allow. Most of the targeted observations are collected over Total Carbon Column Observing Network (TCCON) stations, whose up-looking observations are used to validate the OCO-2 XCO_2 estimates (Wunch et al., 2011a, 2017). Other targets include surface calibration sites (e.g., Bruegge et al., 2019), large urban areas (e.g., Rißmann et al., 2022), and power plants (e.g., Nassar et al., 2017).

OCO-3 began science operations in August, 2019 (Taylor et al., 2020). The OCO-3 instrument is mounted as an external payload on the Japanese Experimental Module Exposed-Facility (JEM-EF) aboard the ISS. The ISS flies in a precessing orbit with a varying time-of-day local overpass across a 63-day illumination cycle. To provide agile pointing from the ISS, a 2-axis Pointing Mirror Assembly (PMA) was added to the fore-optics of OCO-3 (Eldering et al., 2019). For routine science observations, OCO-3 acquires measurements in nadir mode over land and glint mode over large water bodies. A much larger set of target observations are possible compared to OCO-2 due to the more up-to-date on-board electronics control system and the rapid re-pointing allowed by the PMA. In addition, a new observation mode called Snapshot Area Mapping (SAM) allows the instrument to compile contiguous images as large as 80 by $80\,km^2$, over sites of interest such as mega-cities, power plants, volcanoes, flux towers, and field campaigns. The spatially contiguous nature of the SAMs is already showing tremendous promise for both carbon cycle science (e.g., Kiel et al., 2021; Wu et al., 2022; Roten et al., 2022; Nassar et al., 2022) and for investigating sources of bias within the L2FP retrieval (Bell et al., 2023).

The precision and accuracy requirements for OCO-2 and OCO-3 were originally applied to regional scales, roughly defined as 10° latitude by 10° longitude. Early Observation System Simulation Experiments (OSSEs) indicated that an XCO_2 precision and accuracy better than 1 ppm (less than 0.25%) is needed at this scale to constrain typical natural and anthropogenic sources and sinks of CO_2 (Miller et al., 2007). In practice, the spatial scale for precision and accuracy requirements is determined by the distribution of the validation reference measurements. This is defined by the approximately two dozen TCCON stations and a comparable number of EM27/Sun and Aircore stations distributed over the globe. The system performance on finer scales has also been assessed through comparisons with data collected by aircraft campaigns, e.g. ACT-America (Bell et al., 2020) and ATom (Kulawik et al., 2019), and multi-instrument EM27/SUN Campaigns (Rißmann et al., 2022).

The precision and accuracy requirements place strict demands not only on the instrument sensitivity, but also on its calibration and the accuracy of the retrieval algorithm. Both OCO-2 and OCO-3 were radiometrically calibrated prior to launch using integrating sphere sources calibrated with respect to the National Institute of Standards and Technology (NIST) reference standards. Observations of the integrating spheres yielded pre-launch gain coefficients used to convert measured digital numbers into radiances. The radiometric calibration of OCO-2 and OCO-3 is frequently updated in-flight through the use of on-board calibration systems (Crisp et al., 2017; Keller et al., 2022), which are analyzed to update Ancillary Radiometric Products (ARPs) covering three to seven days, where gain degradation coefficients are provided to correct radiances based on prelaunch

gains.

For OCO-2, in-flight updates to the pre-launch calibration are derived from observations of the sun through a transmissive diffuser and from its primary on-board lamp. While the sun observations track the overall change in instrument response with time, lamp observations provide corrections of relative changes in the response of the individual samples, which are comprised of twenty detector pixels each (see Fig. 2 of Crisp et al. (2017) for the readout scheme). Lunar observations taken throughout the mission have been used to track and account for the degradation of the solar diffuser. Details of the pre-flight and on-orbit calibration of OCO-2 Level 1b (L1b) can be found in Rosenberg et al. (2017); Lee et al. (2017); Crisp et al. (2017); Marchetti et al. (2019). In general, the instrument calibration and the full physics retrieval algorithm for OCO-2 have reached relatively mature states. For example, updates to the OCO-2 v10 calibration algorithms used to produce calibrated L1b spectra were limited to an improved treatment of radiometric degradation using lunar calibration observations, a small refinement in the spectral dispersion coefficients, and the identification of additional spectral sample outliers (Crisp et al., 2021).

Keller et al. (2022) describes the current state of the calibration for the L1b OCO-3 v10 data products. OCO-3, unlike OCO-2, cannot view the sun from the ISS, making solar calibration impossible (Rosenberg et al., 2020). Therefore, as compared to OCO-2, more emphasis has been placed on the internal lamp calibration system, which is comprised of three tungsten halogen lamps and a reflective diffuser. The three calibration lamps are illuminated with different cadences and thus age at different rates. For v10 L1b, an algorithm was developed to use information from all three lamps with the goal of mitigating lamp aging while still allowing changes in instrument response to be tracked with the necessary temporal resolution. This is particularly important for OCO-3, as it has exhibited significant, abrupt changes in its overall instrument response. In addition, an update was made to the OCO-3 stray light model used for v10 L1b to account for spatial variability on the detectors. More detail is provided in Section 2.1 of the OCO-3 v10.4 data quality statement (Chatterjee et al., 2022). Because of initial difficulties in reducing geolocation errors for OCO-3, plans to perform lunar calibration, intercomparison of L1b radiances with OCO-2, and vicarious calibration using the Railroad Valley Playa were delayed. These are now all underway and will inform the in-flight calibration for the next OCO-3 product version. Additional OCO-3 calibration details are contained in the L1b Algorithm Theoretical Basis Document (ATBD) (Crisp et al., 2021).

3 The ACOS v10 XCO$_2$ retrieval pipeline

Beginning with the geolocated and calibrated L1b spectra, the ACOS pipeline consists of three distinct steps to produce the final estimates of XCO$_2$. First, due to the computational demands of the L2FP retrieval algorithm, which requires about five minutes per sounding on a single processor, and the inability to reliably estimate XCO$_2$ in the presence of clouds and heavy aerosol loadings, a pre-screening step is performed to identify and remove these soundings (Taylor et al., 2016). The soundings that are identified as likely to yield good quality results are then input to the ACOS Level 2 full physics (L2FP) retrieval

algorithm, which utilizes a Bayesian optimal estimation framework to derive estimates of XCO_2 by combining information from the L1b spectra with prior information about the state of the atmosphere and measurement geometry (Rodgers, 2004; Connor et al., 2008; O'Dell et al., 2012). In a post-processing step, each sounding that successfully converges within the L2FP is assigned either a good or bad quality flag based on a set of empirically-derived filters. Furthermore, an empirical, parametric bias correction, derived from comparisons with multiple truth proxies, is applied to each sounding (O'Dell et al., 2018). The quality-filtered and bias-corrected XCO_2 estimates are included in the L2 Lite files, which also contain essential retrieval, time and geometry information. A brief summary of recent changes specific to v10 is provided in Section 3.1.

3.1 Level 2 full physics retrieval algorithm updates for v10

ACOS v10 is the fourth major reprocessing of the OCO-2 record, which began with the v6 release in December 2014, followed by v7 in 2015, and v8 in 2017 (O'Dell et al., 2018). The v9 XCO_2 product, released in 2018, was a post-processing-only effort to correct XCO_2 errors introduced by a small error in the instrument boresight pointing and geolocation (Kiel et al., 2019). Since there were no changes to the L2FP code from v8 to v9, for the remainder of this document the nomenclature "v8/9" will be used to refer to the previous version of the algorithm. For OCO-3, the v10 XCO_2 product is only the second public release. It is a substantial improvement over the first release, vEarly, which employed the ACOS v10 algorithm, but had significant instrument calibration and geolocation errors, and was quality-filtered and bias-corrected against a very short data record of only a few months (Taylor et al., 2020). Table 1 summarizes the four substantial changes that were made to ACOS L2FP retrieval algorithm from v8/9 to v10. More detail can be found in the v10 L2FP ATBD (Crisp et al., 2020).

Each new release of ACOS uses the latest gas absorption coefficient (ABSCO) tables produced at NASA's Jet Propulsion Laboratory (JPL). For v10, the ABSCO tables were updated from v5.0 (Oyafuso et al., 2017) in ACOS v8/9 to ABSCO v5.1 in ACOS v10 (Payne et al., 2020). The most significant changes occurred in the ABO2 spectral band (Drouin et al., 2017; Payne et al., 2020) related to consistency between oxygen line shapes and collision induced absorption. This update yielded reduced spatial variability of the bias between the L2FP retrieved surface pressure and the prior value from 3.3 hPa in v9 to 2.8 hPa in v10. ABSCO v5.1 also includes an update to the water vapor continuum model, which affects the WCO2 and SCO2 spectral bands.

A second important change between ACOS v8/9 and v10 was an update of the prior values adopted for aerosol types, optical depths (AOD), vertical distribution and the uncertainties. In previous versions, the aerosol priors were compiled from a monthly climatology derived from the NASA Goddard Modeling and Assimilation Office (GMAO) Modern-Era Retrospective analysis for Research and Applications version 2 (MERRA-2) product (Rienecker et al., 2008, 2011; Gelaro et al., 2017). For v10, these monthly aerosol priors were replaced with daily estimates derived from the GEOS-5 Forward Product for Instrument Teams (FP-IT) product. Furthermore, the AOD prior variance (expressed in log(AOD)) were reduced from 2 to 0.5 in v10. These changes lead to significant improvements in both retrieved aerosol values and estimates of XCO_2 from OCO-2, especially in

aerosol-laden regions. Full details on the v10 aerosol formulation, including tests on its efficacy, are provided in Nelson and O'Dell (2019) and Section 3.3.2.3 of Crisp et al. (2020).

185

A third significant change from v8/9 to v10 was replacing the source of the CO_2 prior profiles from that developed by the TC-CON team for use in the GGG2014 algorithm (Wunch et al., 2015) to the newest version used in GGG2020 (Laughner et al., 2023). A complete description of the calculation of the v10 CO_2 priors is provided in Sec. 3.3.2.1 of the L2FP ATBD (Crisp et al., 2020). In short, the priors are calculated from a scaling of the NOAA monthly averaged flask values (Lan et al., 2022)

190 measured at the Mauna Loa and American Samoa sites to individual sounding dates and locations. The tropopause altitude is derived from data contained in the 3-hourly GOES-FPIT meteorology, which has a nominal one-day lag and provides diagnosed potential vorticity, allowing for better representation of latitudinal CO_2 transport in the stratosphere. A previous study using measurements from the Japanese Greenhouse Gases Observing Satellite (GOSAT, Kuze et al. (2009)) processed with the ACOS v9 L2FP retrieval showed that a correction to account for the difference in the CO_2 prior from v8/9 to v10 yielded a

195 global mean adjustment in XCO_2 of approximately 0.2 ppm, with 95% of changes falling between -0.1 and +0.5 ppm (Taylor et al., 2022).

The last significant change to the v10 L2FP was replacement of the solar continuum model used to simulate the top-of-atmosphere (TOA) solar spectrum. For the OCO missions, a high-resolution TOA solar spectrum is derived by combining a

200 high-spectral resolution solar transmission spectrum for solar Fraunhofer lines with an observed, low-spectral resolution TOA solar spectrum. The solar transmission spectrum is derived from an empirical solar line list (Toon, 2014). In earlier versions of the L2FP model, the solar continuum was derived to fit the ATLAS 3 SOLSPEC measurements (Thuillier et al., 2003) when the OCO solar spectrum was convolved with the SOLSPEC spectral response function (SRF). For v10, this continuum was replaced by one derived to fit new measurements from the Total Solar Irradiance Sensor (TSIS) Spectral Irradiance Monitor

205 (SIM) aboard the ISS (Richard et al., 2020) when convolved with the TSIS-SIM SRF. The new solar model reduced the solar continuum values by $\approx$ -1.3%, -3.0%, and -6.5%, in the ABO2, WCO2, and SCO2 spectral bands, respectively. These results are consistent with the more recently derived TSIS-1 Hybrid Solar Reference Spectrum (Coddington et al., 2021). L2FP tests indicated that these changes had a minimal impact to XCO_2 estimates. This is most likely because the solar flux differences were relatively small in the ABO2 channel, which is most sensitive to the accuracy of the solar illumination and absolute

210 radiometric calibration. However, even these small differences shifted the retrieved surface pressures by $\approx$ -0.2 hPa for land and $\approx$ +0.2 hPa for ocean soundings, which has a small impact on the bias correction.

3.2 Preprocessor and sounding selection for v10

The ACOS software includes two preprocessors to flag soundings that are likely to fail to converge in the full physics retrieval due to cloud and aerosol: the A-Band Preprocessor (ABP) (Taylor et al., 2012, 2016) and the IMAP-DOAS Preprocessor (IDP)

215 (Frankenberg et al., 2005; Taylor et al., 2016). For v10, an update was made to the ABP state vector to include a zero level offset to the calculated top of the atmosphere radiances to account for instrument stray light and SIF. The v10 ABP uses v5.1

Table 1. Updates to the ACOS L2FP retrieval algorithm from v8/9 to v10. N/C indicates no change.

		ACOS v8/v9	ACOS v10
1	Spectroscopy	ABSCO v5.0	ABSCO v5.1
2	Aerosol prior source	MERRA monthly climatology	3-hourly GEOS-5 FP-IT with tightened prior AOD uncertainty
3	CO_2 prior source	TCCON GGG2014	TCCON GGG2020
4	Solar continuum model	ATLAS 3 SOLSPEC	TSIS-SIM

ABSCO to be consistent with the L2FP retrieval. To accommodate changes to the ABSCO and L1b, updates were made to tune the ABP surface pressure vs. solar zenith angle and chi-squared vs. signal-to-noise ratio parameterizations, both of which are used as individual filters to determine scenes contaminated by clouds and aerosols as first described in (Taylor et al., 2012) for application to GOSAT, and more recently in Taylor et al. (2016) as applied to OCO-2.

The IDP algorithm serves two purposes in the ACOS pipeline: (i) single band retrievals of CO_2 and H_2O are used for cloud screening, and (ii) the ABO2 spectral band is used to estimate SIF (Frankenberg et al., 2012; Doughty et al., 2022). For v10, no changes were made to the IDP. In fact, the code has remained unaltered for many versions, including use of the older v4.2 ABSCO (Drouin et al., 2017).

The sounding selection strategy, which determines if a sounding should be run through the L2FP, remains roughly consistent for v10 compared to previous versions. Details are provided in Table 2. For both sensors, the single difference between land and ocean-glint selection criteria is that for OCO-2, the solar zenith angle (SZA) cutoff is slightly more strict at $80°$ for ocean-glint, compared to $85°$ for land. For OCO-3, the SZA cutoff is $80°$ for both land and ocean-glint. For OCO-2 v10, target mode observations were filtered using the satellite observation angle to remove soundings more oblique than $50°$. This criterion was removed for OCO-3 target (and SAM) observations, so that the same set of selection criteria is used for all land observations. Because there is minimal information content in ocean-nadir measurements due to a low signal-to-noise ratio (SNR), no ocean-nadir soundings were selected for OCO-2 v10. However, the early part of the OCO-3 record contains a large fraction of ocean-nadir observations prior to tuning of the PMA. To maximize the selection of potentially good quality soundings, the L1b SNR filters in both the ABO2 and SCO2 spectral bands were relaxed. However, the scientific merit of the ocean-nadir observations is as of yet undetermined and therefore ocean-nadir soundings are not considered further in this work.

3.3 Postprocessing: quality filtering and bias correction for OCO v10 XCO$_2$ estimates

All selected soundings, as described in Section 3.2, are subsequently processed by the L2FP retrieval, which primarily estimates XCO$_2$. Soundings that converge (typically $\approx 85\text{-}90\%$ of the attempts), are reported in the L2 Standard product files

Table 2. Sounding selection criteria for OCO-2 and OCO-3 v10. Soundings are categorized as either land (land fraction $\geq 80\%$), water (land fraction $\leq 20\%$), or indeterminate ($20\% <$ land fraction $< 80\%$). N/U = Not Used. N/P = Not Processed. In addition to the criteria defined in the table, all soundings must have a "sounding quality flag" = 0.

OCO-2 v10	Land (all except TG)	TG	Ocean-Glint	Ocean-Nadir
Solar zenith angle	≤ 85	≤ 85	≤ 80	N/P
Observation zenith	N/U	< 50	N/U	N/P
ABP cloud flag	$= 0$	$= 0$	$= 0$	N/P
IDP CO_2 ratio	[0.985, 1.045]	N/U	[0.985, 1.045]	N/P
L1b ABO2 SNR	> 100	N/U	> 100	N/P
L1b SCO2 SNR	> 75	N/U	> 75	N/P

OCO-3 v10	Land (all)		Ocean-Glint	Ocean-Nadir
PMA motion flag	$= 0$		$= 0$	$= 0$
Solar zenith angle	≤ 80		≤ 80	≤ 80
Observation zenith	N/U		N/U	N/U
ABP cloud flag	$= 0$		$= 0$	$= 0$
IDP CO_2 ratio	[0.980, 1.055]		[0.980, 1.055]	[0.980, 1.055]
IDP H_2O ratio	[0.80, 1.25]		[0.80, 1.25]	[0.80, 1.25]
L1b ABO2 SNR	> 100		> 100	> 225
L1b SCO2 SNR	> 50		> 50	> 125

(L2Std), which are organized into granules, which typically include full orbits or partial orbits, yielding about 15 files per day. The L2Std files are in HDF5 format, and are about 20 MB each (≈ 300 MB per day). Next, a post-processing step assigns to each sounding a binary quality flag (QF=0 indicates the best data), as well as a bias correction adjustment to XCO_2 (O'Dell et al., 2018). The results are aggregated into daily output L2 Lite XCO_2 files. Lite files are in NetCDF format and are typically about 50-70 MB each. It is highly recommended that only the good quality (QF $= 0$) soundings contained in the L2 Lite XCO_2 product be used in global and regional scale studies, although local scale studies may benefit from the use of some of the lower quality (QF > 0) soundings.

3.3.1 Quality filtering and bias correction truth proxies

The quality filtering and bias correction procedure requires XCO_2 truth proxies, with which to compare the retrieved estimates. The term truth-proxies is used to describe sources of data which can be used as an independent estimate of the atmospheric CO_2 abundance. For OCO v10, three truth proxies were used. The first was estimates of XCO_2 derived from TCCON measurements. Table 3 provides a list of TCCON stations, locations, operational ranges, and data citations. Although TCCON XCO_2

255   estimates have relatively high precision and accuracy, while providing good temporal coverage at most sites, they are very limited in spatial extent, especially outside of the northern mid-latitudes.

To augment the sparse spatial coverage of TCCON, atmospheric inversion models are used in the OCO XCO_2 quality filtering and bias correction process to provide full global coverage (O'Dell et al., 2018). For ACOS v10, the median XCO_2 was derived
260   from the 4-dimensional (4D) CO_2 fields of models that assimilated only in-situ CO_2 data. To ensure consistency in the models, for each OCO sounding, only the models with XCO_2 that deviated by less than ± 1.5 ppm from the initial median value were retained. Furthermore, soundings were excluded if more than one of the models had been rejected, or if the standard deviation amongst the valid models was >1 ppm. Tables 4, 5, and 6 provide information about the suite of models. An asterisk is used in Table 6 to identify the specific models and data versions used in the quality filtering and bias correction procedure: three for
265   OCO-2 and four for OCO-3 v10. Some of the same models were also used in the XCO_2 evaluation, but using a different model data version and a different evaluation period. A few of the models were used only for the XCO_2 product evaluation.

An averaging kernel correction was applied to both the TCCON and the model XCO_2 values to account for differences in the vertical profiles compared to the ACOS prior. The general form of the equation is:

$$270 \quad \mathrm{XCO}_{2,ak} = \sum_{i=1}^{20} \mathbf{h}_i \{ \mathbf{a}_i \mathbf{u}_{m,i} + (1 - \mathbf{a}_i) \mathbf{u}_{a,i} \}. \tag{1}$$

Here, $\mathbf{h}_i$ is the pressure weighting function on the $i = 1...20$ ACOS model levels, defined as the pressure intervals assigned to the state vector normalized by the surface pressure and corrected for the presence of atmospheric water vapor. See Appendix A of O'Dell et al. (2012) for details. The vector $\mathbf{a}$ is the CO_2 column averaging kernel, which relates the sensitivity of the retrieved CO_2 to the true atmospheric state of CO_2 at each vertical level, as described in Connor et al. (2008). The vector $\mathbf{u}_m$ is
275   the retrieved TCCON or model profile of CO_2, linearly interpolated from the native vertical resolution to the 20 ACOS levels. The vector $\mathbf{u}_a$ is the ACOS prior profile of CO_2. Generally the averaging kernel corrections are on the order of 0.5 ppm or less.

Finally, a third truth proxy for training the v10 quality filtering and bias correction was the "small area approximation" (SAA). Each small area is a collection of OCO XCO_2 soundings over < 100 km sections within single orbits, where, in the absence of
280   strong localized sources, the real uncertainty in XCO_2 is expected to be well under 0.1 ppm (Worden et al., 2017). A median value of each small area provides a truth proxy to which each sounding in the small area can be compared. While small areas are not suitable for determining large-scale biases in the satellite data, they provide a measure of the uncertainty in the XCO_2 estimates, due to both instrument noise and systematic errors that act on smaller scales. This "actual" uncertainty can be compared to the "theoretical" uncertainty derived from the L2FP retrieval and stored in the L2Lite files as *xco2_uncertainty*. For
285   the v10 quality filtering and bias correction training, approximately 750×10^3 and 280×10^3 small areas were identified for OCO-2 and OCO-3, respectively.

Table 3. TCCON stations used in the quality filtering and bias correction of OCO-2 and OCO-3 v10. Sites used only for OCO-2 are indicated with a dagger (†) in the first column. Sites located on an island are indicated with an asterisks (*) in the second column.

TCCON Station Name	Continent	Latitude (degrees)	Altitude (meters)	Operational Date Range (YYYYMM - YYYYMM)	Data Citation
Sodankylä[†]	Europe	67.4 N	188	200901 – present	Kivi et al. (2020)
East Trout Lake	North America	54.4 N	502	201610 – present	Wunch et al. (2018)
Bialystok[†]	Europe	53.2 N	180	200903 – 201810	Deutscher et al. (2017)
Bremen[†]	Europe	53.1 N	27	200407 – present	Notholt et al. (2019)
Karlsruhe	Europe	49.1 N	116	200909 – present	Hase et al. (2015)
Paris	Europe	48.8 N	60	201409 – present	Te et al. (2014)
Orleans	Europe	48.0 N	130	200908 – present	Warneke et al. (2014)
Garmisch	Europe	47.5 N	740	200707 – present	Sussmann and Rettinger (2018a)
Zugspitze	Europe	47.4 N	2960	201204 – present	Sussmann and Rettinger (2018b)
Park Falls	North America	45.9 N	440	200405 – present	Wennberg et al. (2017a)
Rikubetsu	Asia	43.5 N	380	201311 – present	Morino et al. (2018c)
Lamont	North America	36.6 N	320	200807 – present	Wennberg et al. (2016)
Anmyeondo[†]	Asia	36.5 N	30	201408 – present	Goo et al. (2017)
Tsukuba	Asia[*]	36.1 N	30	200812 – present	Morino et al. (2018a)
Nicosia	Europe[*]	35.1 N	185	201908 – present	Petri et al. (2020)
Edwards	North America	35.0 N	699	201307 – present	Iraci et al. (2016)
JPL[†]	North America	34.2 N	390	201103 – 201307	Wennberg et al. (2017b)
				201706 – 201805	Wennberg et al. (2017b)
Caltech	North America	34.1 N	230	201209 – present	Wennberg et al. (2015)
Saga	Asia[*]	33.2 N	7	201106 – present	Shiomi et al. (2014)
Izana	Africa[*]	28.3 N	237	200705 – present	Blumenstock et al. (2017)
Burgos	Asia[*]	18.5 N	35	201703 – present	Morino et al. (2018b)
Ascension[†]	Africa[*]	7.9 S	10	201205 – present	Feist et al. (2017)
Darwin	Australia	12.4 S	30	200508 – present	Griffith et al. (2014a)
Reunion	Africa[*]	20.9 S	87	201109 – present	De Mazière et al. (2017)
Wollongong	Australia	34.4 S	30	200805 – present	Griffith et al. (2014b)
Lauder	Australia[*]	45.0 S	370	200406 – present	Pollard et al. (2017)

Table 4. Names, institutions and citations of the atmospheric inversion systems used in the quality filtering and bias correction and XCO$_2$ evaluation of OCO v10.

Model Name	Institute	Citations
CAMS-REAN	European Centre for Medium-range Weather Forecasts	Agustí-Panareda et al. (2014); CAMS-REAN (2021)
CAMS-INV	Copernicus Atmosphere Monitoring Service	Chevallier et al. (2010); CAMS-INV (2021)
CarbonTracker	NOAA Global Monitoring Laboratory	Peters et al. (2007); Jacobson et al. (2021)
CarboScope	Max Planck Institute for Biogeochemistry	Rödenbeck et al. (2018); CarboScope (2021)
LoFI	NASA Goddard GMAO	Weir et al. (2021)
UoE	University of Edinburgh Atmospheric Composition Modelling Group	Feng et al. (2009); UoE (2021)

Table 5. Characteristics of models used for quality filtering, bias correction, and evaluation of OCO v10. N/A indicates Not Applicable.

Model Short Name	Spatial Resolution [lat×lon]	Temporal Resolution	Transport Model	Inverse Method	Meteorology Source
CAMS-REAN	0.75°×0.75°	3 h	Integrated Forecast System (IFS)	4D-Var	ECMWF
CAMS-INV	1.9°×3.75°	3 h	LMDZ	Variational	ERA-Interim
CarbonTracker	2°×3°	3 h	TM5	EnKF	ERA-Interim
CarboScope	4°×5°	6 h	TM3	4D-Var	NCEP
LoFI	0.5°×0.625°	3 h	GEOS GCM	N/A	MERRA-2
UoE	2°×2.5°	3 h	GEOS-Chem	EnKF	GEOS-FP

3.3.2 Quality filtering and bias correction methodology

Details of the OCO quality filtering procedure were described in Sec. 4.2 of Kiel et al. (2019) for the OCO-2 v9 product and in Sec. 6.2 of Taylor et al. (2020) for OCO-3 vEarly. Here, the method is summarized and differences in the v10 implementation for OCO-2 and OCO-3 are highlighted. In short, the quality filtering procedure assigns to each sounding in the L2Std XCO$_2$ product a good (QF = 0) or bad (QF = 1) binary quality flag based on comparison to truth proxies. A number of retrieval parameters (32 for OCO-2 v10 and 30 for OCO-3 v10.4) are assigned threshold cutoff values, outside of which a sounding is considered unreliable, although all soundings in the L2Std product are retained in the L2 Lite XCO$_2$ files. The selected variables and their threshold values can be found in Sec. 3.2.4 of the OCO-2 v10 Data User's Guides (DUG) (Osterman et al., 2020), and Sec. 5.1.2 of the OCO-3 v10.4 DUG (Payne et al., 2022). Training for the quality filtering and bias correction procedure takes place on a Quick Test Set (QTS), which is an intelligently selected subset of approximately 5% of the full

Table 6. Model versions used for the quality filtering and bias correction (indicated by asterisk *) and XCO$_2$ evaluation of OCO v10. N/A means not applicable.

Model Name	QF/BC Version	QF/BC Time period	Evaluation Version	Evaluation Time period
		OCO-2		
CAMS-INV*	2018-v2	20140906 - 20190304	v20r2	20190806 - 20201231
CarbonTracker*	CT-NRT.v2019-2	20140906 - 20190329	N/A	N/A
CarboScope*	s04oc-v4	20140906 - 20190304	s10oc-v2021	20190806 - 20201231
Lo-Fi	N/A	N/A	m2ccv1sim	20190806 - 20201231
UoE	N/A	N/A	v5	20190806 - 20201231
		OCO-3		
CAMS-REAN*	v11899	20190806 - 20210223	N/A	N/A
CAMS-INV*	v20r3	20190806 - 20210223	v20r2	20190806 - 20201231
CarbonTracker*	CT-NRT.v2021-3	20190806 - 20200731	N/A	N/A
Lo-Fi	m2ccv1	20190806 - 20210223	m2ccv1sim	20190806 - 20201231
CarboScope*	N/A	N/A	s10oc-v2021	20190806 - 20201231
UoE	N/A	N/A	v5	20190806 - 20201231

OCO data record that is available at the time of the training.

300   The methodology for the empirical bias correction of the XCO$_2$ estimates was first described in Wunch et al. (2011b), and later in more detail by O'Dell et al. (2018), where the fundamental equation for OCO is defined as:

$$\text{XCO}_{2,\text{bc}}\,(\text{mode}, j) = \frac{\text{XCO}_{2,\text{raw}} - C_P\,(\text{mode}) - C_F\,(j = 1 \dots 8)}{C_0\,(\text{mode})}. \tag{2}$$

Here, C_P is the mode-dependent parametric bias, C_F is a mode and footprint-dependent bias for each of the eight footprints, and C_0 represents a mode-dependent global scaling factor. Bias correction coefficients are derived using only soundings that

305   have been assigned a good quality flag. Many details related to the v10 quality filtering and bias correction can be found in the DUGs (Osterman et al., 2020; Payne et al., 2022).

For ACOS OCO-2 v10, the selected bias correction parameters are similar to those used in previous versions. For land, the parameters are (i) a term related to the deviation in the retrieved CO_2 profile from the prior: "CO_2 grad del", (ii) the difference between the elevation adjusted retrieved surface pressure and the prior surface pressure: dP_{frac}, (iii) the combined aerosol optical depth (AOD) of coarse-mode particles: $\log\left(\mathrm{AOD}_{\mathrm{dust}} + \mathrm{AOD}_{\mathrm{water\,cloud}} + \mathrm{AOD}_{\mathrm{sea\,salt}}\right)$, and (iv) the AOD of fine-mode particles: $\mathrm{AOD}_{\mathrm{fine}}$. Ocean retrievals use two terms: (i) CO_2 grad del, and (ii) the difference between the retrieved and prior surface pressure in the SCO2 band: dP_{SCO2}. The bias correction is very similar for OCO-3 v10, with the exception that the coefficients are slightly different, and over land, the $\mathrm{AOD}_{\mathrm{fine}}$ term has been replaced with a criteria based on the retrieved albedo in the weak CO_2 channel.

Table 7 provides a statistical summary of the results from the quality filtering and bias correction for both OCO-2 and OCO-3 for each of the three truth proxies. Results are given separately for land observations (combined nadir and glint) and for ocean-glint observations. The number of soundings contained in each truth proxy data set that was used in the quality filtering and bias correction procedure is listed, along with the fraction of the total soundings contained in the L2 Lite XCO_2 product that were assigned a good quality flag, i.e., the throughput. The standard deviation (σ) of the difference between the satellite XCO_2 estimates and the truth proxy values are derived relative to (i) the raw XCO_2 prior to bias correction, (ii) the quality-filtered XCO_2, and (iii) the combined quality-filtered and bias-corrected XCO_2. The two right-most columns of the table show the percent of the variance explained by the quality filtering (compared to the raw XCO_2) and the bias correction (compared to the quality filtered XCO_2), respectively. The variance explained is calculated as $1 - (\sigma_2/\sigma_1)^2$, where σ_1 is the original uncertainty (standard deviation) in the ΔXCO_2 and σ_2 is the remaining uncertainty. For each sensor and for both land and ocean-glint observations, the mean values from the three truth proxies are provided to help summarize the statistics.

Table 7. Summary of the OCO-2 and OCO-3 v10 quality filtering (QF) and bias correction (BC) results versus the individual XCO_2 truth proxies.

Mode	Sensor	Truth Proxy	N (10^3 soundings)	Fraction Good QF	Sigma (ppm) Raw	QF	QF & BC	Variance Explained by QF	by BC
Land	OCO-2	TCCON	700	67%	2.74	1.74	1.15	60%	56%
		Models	3950	44%	3.77	1.67	1.09	80%	57%
		SAA	1400	69%	2.18	1.53	0.84	51%	71%
mean=			2017	60%	2.90	1.65	1.03	64%	61%
Land	OCO-3	TCCON	200	69%	2.02	1.50	1.33	45%	24%
		Models	2150	56%	2.76	1.49	1.16	71%	34%
		SAA	870	67%	1.70	1.11	0.97	57%	43%
mean=			1073	64%	2.16	1.37	1.30	58%	34%
Ocean-Glint	OCO-2	TCCON	240	71%	1.73	1.07	0.82	62%	41%
		Models	2030	52%	2.52	1.12	0.73	80%	58%
		SAA	750	72%	1.52	0.90	0.46	65%	74%
mean=			1006	65%	1.92	1.03	0.67	69%	58%
Ocean-Glint	OCO-3	TCCON	170	54%	2.05	1.15	1.01	69%	23%
		Models	1560	55%	2.22	1.21	0.72	70%	65%
		SAA	910	73%	1.59	0.97	0.47	63%	77%
mean=			880	61%	1.95	1.11	0.73	67%	55%

Overall, the fraction of good-quality soundings remains the same at approximately 60% for both sensors for land and ocean-glint. XCO_2 estimates from both sensors exhibit comparable uncertainties in raw XCO_2 against the three truth proxies of $\approx$ 2-3 ppm. Estimates from both sensors show a reduction in uncertainties after application of first, the quality filter, and then the combined quality filter and bias correction to approximately 1 ppm for land and 0.7 ppm for ocean-glint. Even though the mean of the uncertainties for the OCO-2 raw XCO_2 versus truth proxies for land was higher (2.9 ppm) compared to OCO-3 (2.2 ppm), the mean of the uncertainties for the OCO-2 quality-filtered and bias-corrected XCO_2 of 1.0 ppm is somewhat smaller than for OCO-3 at 1.3 ppm. This implies that the bias correction is more effective for OCO-2 than for OCO-3 over land. This is evidenced in the right-most column of the table, which indicates that the OCO-2 bias correction explains, 56%-71% of the variance (mean of 61%) across the truth proxies, while only 24%-43% of the variance (mean of 34%) is explained by the OCO-3 bias correction. For ocean-glint observations, the variance explained by the bias correction is similar for OCO-2 and OCO-3 at 58% and 55%, respectively.

The lower variance explained by the OCO-3 bias correction seems to originate from a combination of both a less effective dP correction, and a much less effective CO_2 grad del correction, a term related to the deviation in the retrieved CO_2 profile from the prior. It is likely that the residual pointing errors in OCO-3 v10 of up to 1-2 km (median of ≈ 0.5 km), shown in Appendix B, produce a less accurate surface pressure prior, which in turn yields larger dP uncertainties from the L2FP retrieval. In addition,
345   remaining radiometric calibration issues in the OCO-3 ABO2 spectral band may affect the retrieved surface pressure. Both of these factors could explain the less effective OCO-3 dP bias correction term. No viable explanation has yet been formulated for why the OCO-3 CO_2 grad del bias correction term is so much less effective relative to that for OCO-2.

Improvements in successive versions of the ACOS L2FP retrieval are demonstrated in Fig. 1, which compares RMS errors in
350   XCO_2 from v9 and v10 OCO-2 and v10 OCO-3 versus the three truth-proxies for land and ocean-glint observations. There are substantial decreases in the RMSE for OCO-2 from v9 to v10 as compared to both TCCON and to the MMM for both land and ocean-glint. The changes in the OCO-2 RMSE from v9 to v10 for the small area analysis were insignificant between versions, which is to be expected because errors at very small spatial scales are primarily driven by instrument noise, which cannot be further reduced. For all three truth metrics versus land observations, OCO-3 compares worse than OCO-2. The discrepancy is
355   likely driven by both OCO-3 residual pointing errors and L1b calibration errors, both of which are expected to improve in the next data version. The worse agreement of OCO-3 v10 with TCCON as compared to OCO-2 v10 can be explained in part by the limited number of TCCON collocations with OCO-3 that were available at the time of creation of the QTS. Incidentally, the data also demonstrate that for all truth proxies and for both sensors, ocean-glint errors are lower than land errors, indicating higher precision relative to land observations. This result is at odds with previous findings showing unrealistic features in global
360   inversion models which assimilate OCO-2 ocean-glint data (e.g. Peiro et al., 2022; Byrne et al., 2023).

4   OCO v10 XCO_2 data volumes

Global maps showing the spatial distribution of the native sounding densities for a single year (2020) and a single footprint, are shown in panels (a) and (c) of Fig. 2, for OCO-2 and OCO-3, respectively. The data here have been aggregated to $2.5°$ by $5°$
365   latitude/longitude grid cells, whereas the actual swath width of each sensor is on the order of 10 km. Although the total number of soundings collected is very similar (≈ 40 million), the distinct difference in latitudinal extent of the two sensors due to the orbital characteristics is evident. The polar orbit of OCO-2 provides nearly continuous latitudinal coverage. There is somewhat less coverage for orbit tracks over the northeastern Pacific because these orbits are used for data down-link, during which the OCO-2 instrument does not acquire science measurements. The precessing orbit of OCO-3 on the ISS limits coverage to
370   latitudes less than $\approx 52°$, near which there is a high density of soundings at the orbit inflection points. In other words, OCO-3 produces a similar overall number of soundings compared to OCO-2, but the soundings are restricted into a smaller area, thus producing a higher density.
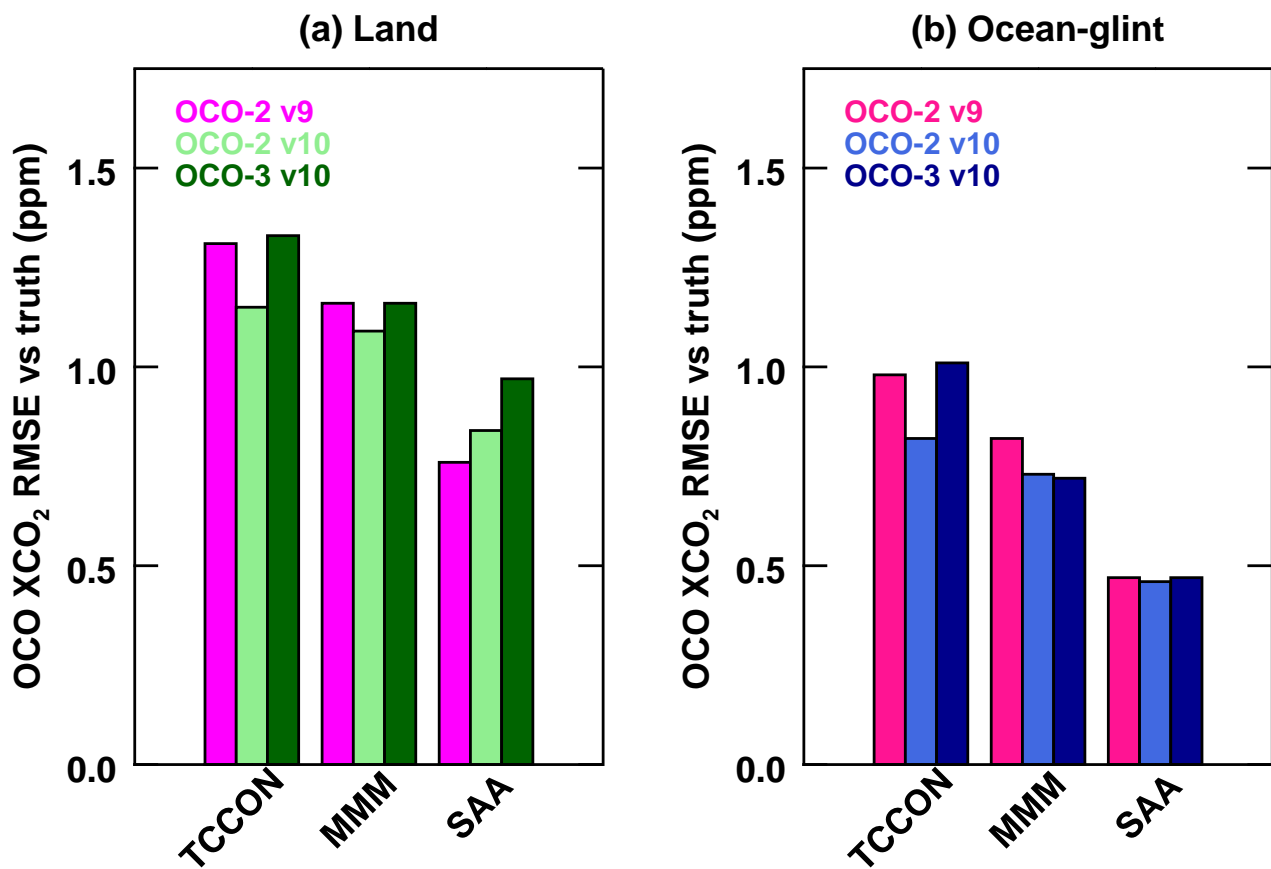
Figure 1. RMS errors for different versions of OCO-2 and OCO-3 XCO_2 versus three truth proxies: TCCON, multi-model-median (MMM), and small area approximations (SAA). Results are derived from single sounding statistics using quality-filtered and bias corrected XCO_2 from the QTS. Results for land observations are shown in panel (a), while panel (b) shows results for ocean-glint observations.

The soundings that pass the preprocessor checks for cloud and aerosol loading and then converge in the L2FP algorithm are assigned either a good (QF=0) or a bad (QF>0) quality flag in post-processing. Typically, is is recommend that only the good quality flag soundings are used in atmospheric inversion systems to deduce CO_2 fluxes. Panels (b) and (d) of Fig. 2 show the sounding densities of the good quality-flagged data for OCO-2 and OCO-3, respectively. Qualitatively, the distributions of good soundings from the two sensors resemble clear-sky fraction maps, as expected. Over land, OCO-3 provides more good soundings than OCO-2, especially near 50° latitude as a result of the ISS orbit. Furthermore, OCO-3 operates almost exclusively in nadir mode over land, which may also contribute to a higher good quality sounding throughput relative to OCO-2 land-glint observations, which have higher optical pathlengths and thus sensitivity to clouds and aerosols. Conversely, OCO-3 provides less good soundings over the oceans compared to OCO-2 due to lower sampling rates in glint observation mode as constrained by operations aboard the ISS. Mechanical and operational constraints on the OCO-3 instrument frequently preclude pointing towards the glint spot. During these periods, the instrument collects ocean data in nadir mode, for which the signal-to-noise ratio is too low to provide accurate estimates of XCO_2.
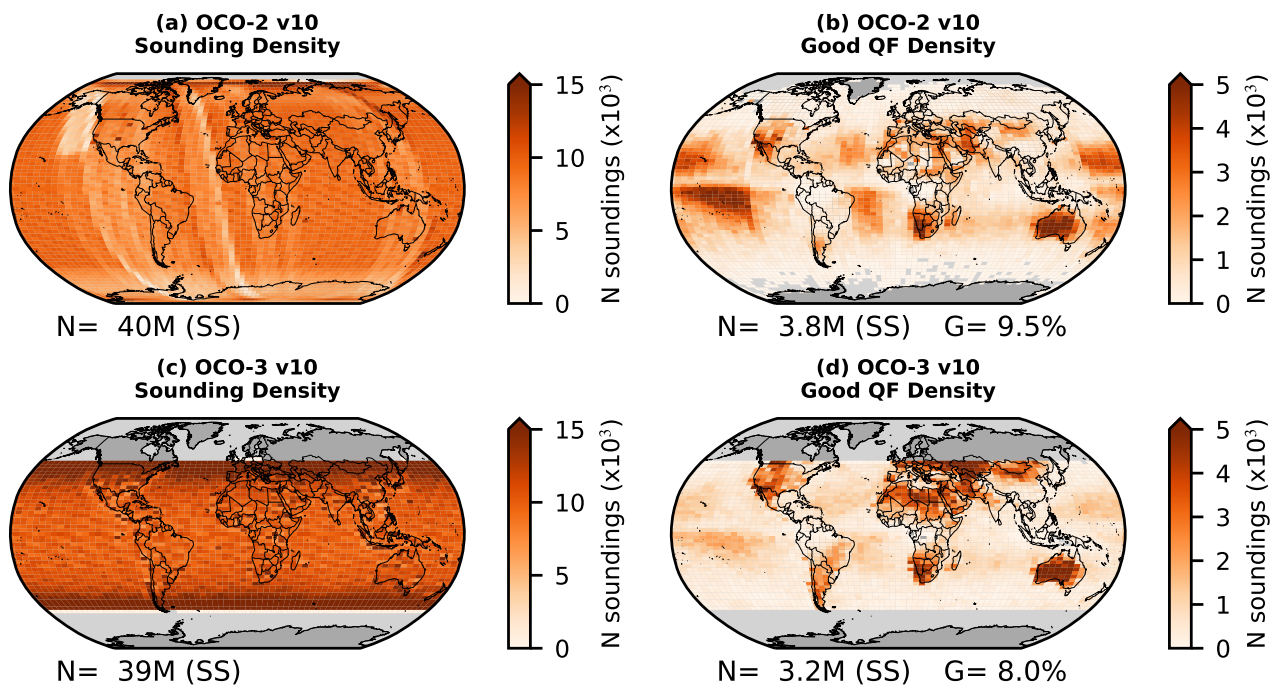
Figure 2. Version 10 data volumes from a single detector footprint (4 of 8, 1-based) for the year 2020 gridded at 2.5° latitude by 5° longitude resolution for OCO-2 (top row) and OCO-3 (bottom row). The total number of measured soundings (N) for each sensor are shown in panels (a) and (c). Panels (b) and (d) show the number of soundings (N) that were assigned a good quality flag in the L2 Lite XCO_2 product. The percent of the total number of measurements is given as G. Grid cells containing less than 10 soundings are colored gray.

Figure 3 shows bar plots quantifying the number of good soundings by month for each observation mode for the overlapping time period August 2019 through February 2022 for OCO-2 (a) and OCO-3 (b). These plots help to visualize the difference in the ratio of land to ocean-glint observations for the two sensors. OCO-2 collects a much larger and more stable fraction of monthly ocean-glint compared to OCO-3. The lack of good quality ocean-glint OCO-3 observations early in the mission is evident, as observations were often restricted to nadir viewing mode due to safety concerns related to early uncertainties in the effects of polarization and signal levels for OCO-3, which were mitigated by revised PMA pointing with respect to the glint spot (Taylor et al., 2020). The plot also highlights the higher relative fraction of OCO-3 TG and SAM data (8% of the total), compared to only 1% TG data for OCO-2, a distinguishing characteristic that sets the two missions apart.

390

395
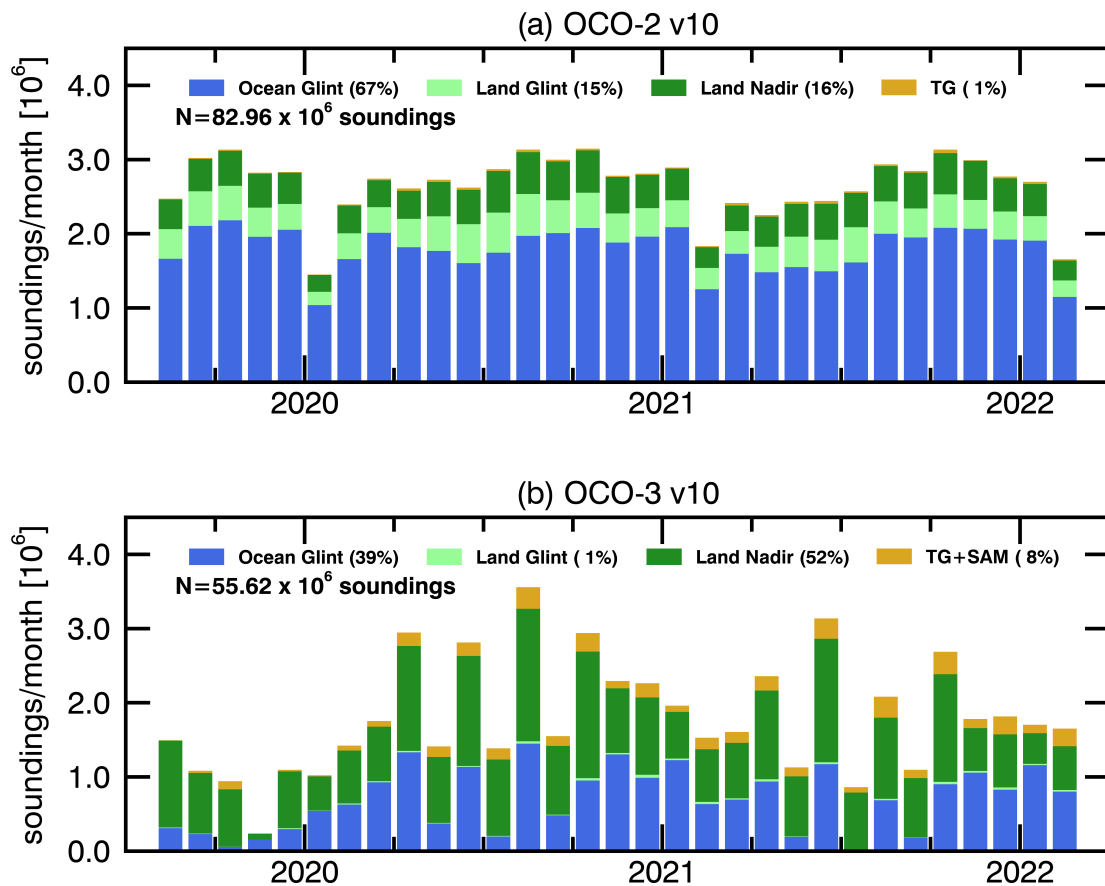
Figure 3. Bar plots of the monthly number of good quality-flagged soundings for OCO-2 (a) and OCO-3 (b) by observation mode (colors) for the time period August 2019 through February 2022. The fractional percent for each observation mode is listed in the legend, along with the total number of good quality-flagged soundings (N).

Figure 4 presents the densities of good data (QF=0) gridded in time (10 day) and latitude (10°) for OCO-2 (top) and OCO-3 (bottom). This again effectively demonstrates the difference in spatial coverage between the two sensors. The time-latitudinal coverage of OCO-2 is much smoother than OCO-3 due to the repeating sun-synchronous polar orbit. In contrast, OCO-3 has a sinusoidal-like pattern of alternating high and low densities over mid-latitudes, with the maximum value alternating in time between the northern and southern hemispheres. This is due to the precessing orbit of OCO-3 aboard the ISS, which introduces periodic variations in the portion of the earth that is viewed during daylight hours. In addition, OCO-3 is subject to both predictable and unpredictable periods during which science measurements either cannot be collected at all, or are limited to nadir viewing, as discussed in Appendix B. Predictable data gaps occurs rather frequently for ocean-glint observations, due to physical viewing constraints aboard the ISS JEM-EF. Periods of missing data that are longer than 10 days can be seen in panel (d) as columns that are fully grey.
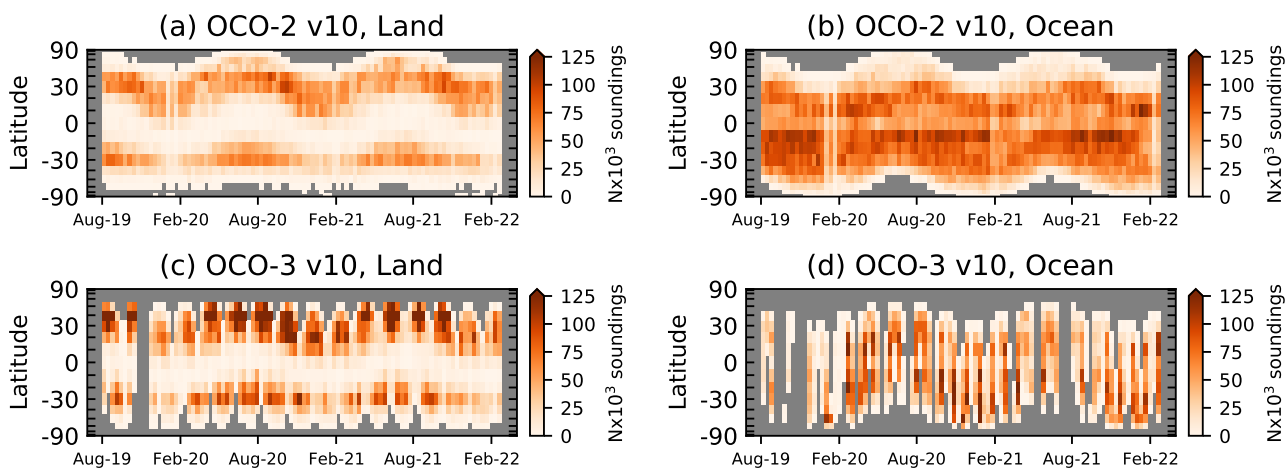
Figure 4. Data density (10^3) of the number of good quality flagged soundings for v10 OCO-2 (top) and OCO-3 (bottom) for land (left) and ocean (right) at 10° latitude by 10 days resolution for the time period August 2019 through February 2022. The ordinate axis is scaled by the cosine of the latitude to elucidate the decreasing fractional surface area of the earth with increasing latitude. Grid cells containing less than 10 soundings are colored gray.

5 Comparing v10 XCO$_2$ estimates from OCO-2 and OCO-3

As described in Section 1 of the OCO-3 v10.4 data quality statement (Chatterjee et al., 2022), early in the production of the OCO-3 v10 XCO$_2$ Lite product, an analysis of XCO$_2$ estimates collocated to OCO-2 soundings suggested that there was a diverging trend that was correlated with time since the last OCO-3 instrument decontamination cycle. After development and application of an "ad hoc" bias correction to the OCO-3 XCO$_2$, the drift was eliminated, bringing the two sensors into

agreement within the expected uncertainties of a few tenths of a ppm. A new set of OCO-3 L2 Lite XCO_2 files (v10.4) was generated and distributed to the NASA Goddard Earth Sciences (GES) Data and Information Services Center (DISC) website OCO Science Team et al. (2022). A full discussion of the ad hoc correction is provided in Appendix B. The remainder of the analysis that follows uses the OCO-3 v10.4 XCO_2.

Figure 5 shows maps of the magnitude of the bias correction (ppm) for both sensors for April and August, 2020. The patterns look qualitatively similar, with bias corrections ranging from zero to ≈ 2 ppm in the midlatitudes and polar regions, and bias corrections of up to ≈ 4 ppm over the Sahara and dust outflow regions, as well as the tropical oceans. The mean global bias corrections are slightly larger for OCO-2 compared to OCO-3 for both months, but the uncertainties are slightly smaller for OCO-3. The 2020 annual median bias correction was 1.81 ppm for OCO-2 and 2.11 ppm for OCO-3. Note that, the OCO-3 v10.4 time-dependent ad hoc bias correction discussed in Appendix B3 has been removed.
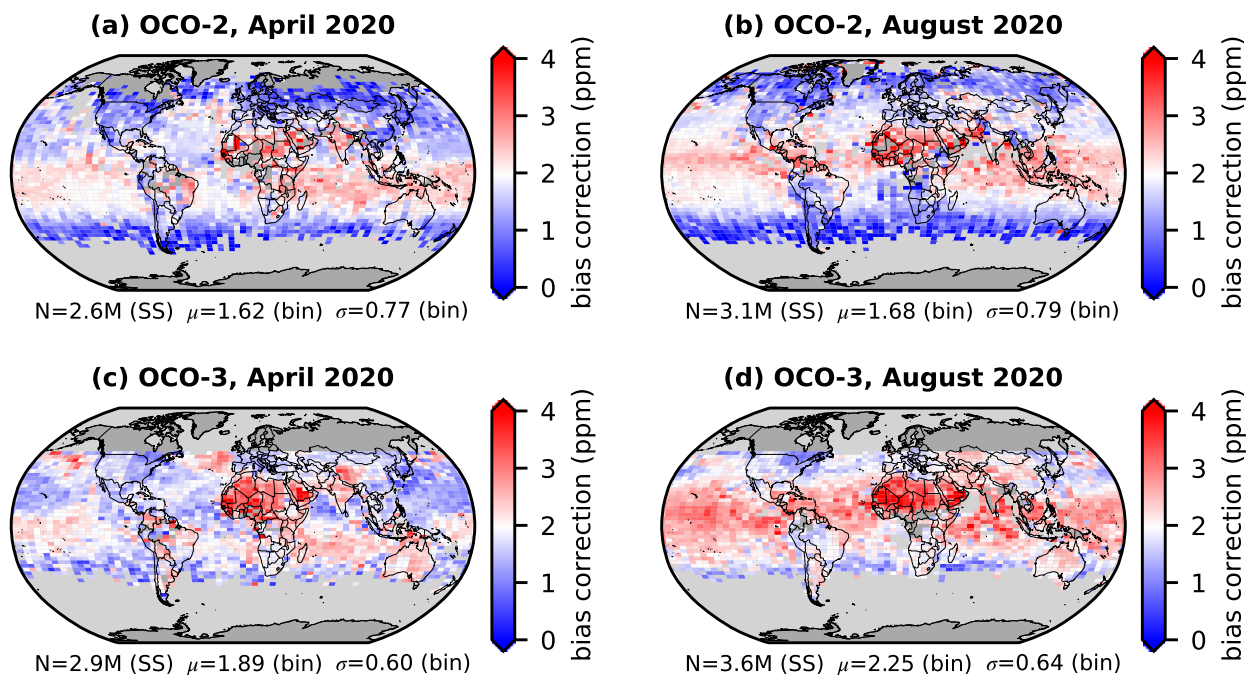
Figure 5. Monthly maps of the bias correction for OCO-2 (top row) and OCO-3 (bottom row) for April 2020 (left) and August 2020 (right) gridded in 2.5° latitude by 5° longitude bins. The number of single soundings (SS) are given by N, while the mean (μ) and standard deviation (σ) of the gridded (bin) data are reported. Grid cells with less than 10 soundings are colored gray.

Figure 6 shows the spatial maps of OCO-2 and OCO-3 gridded quality-filtered and bias corrected XCO_2 for the months of April 2020 and August 2020. The well-known features of the atmospheric distribution of CO_2 are present. For example, high values

are observed in the northern hemisphere (NH) spring when the land biosphere is still quiescent (≈ 415 ppm), followed by lower values at high northern latitudes in August when the biosphere is most active (≈ 405 ppm). Since the seasonal cycle of CO_2 is driven primarily by biospheric activity on land, the difference in April and August XCO_2 in the southern hemisphere (SH) is much smaller compared to the NH. Although the distribution of XCO_2 between the two sensors is qualitatively similar, the fig-

430   ures illustrate the difference in latitudinal coverage due to the differing orbit characteristics. This has meaningful consequences for the interpretation of flux estimates derived from inverse modeling of the OCO-2 and OCO-3 XCO_2 concentrations. For example, OCO-3 cannot directly capture the strong summer draw down of CO_2 in the northern boreal forests. For this time and location, an inversion of OCO-3 CO_2 fluxes must rely more on the model prior values since there is no information provided by satellite measurements, whereas an assimilation of OCO-2 XCO_2 for this same time and location would provide information to

435   the models since the satellite observed this location at this time. It is worth noting that it is challenging to produce a meaningful difference in XCO_2 for the two sensors at the global scale due to the spatial and temporal differences in sampling. Generally, such maps look qualitatively like differences in CO_2 driven by synoptic-scale weather patterns, as for any given grid box, there might be a difference of several days in observations from the two sensors. However, a direct comparison in XCO_2 on a small set of collocated observations is provided in Appendix B3.

440
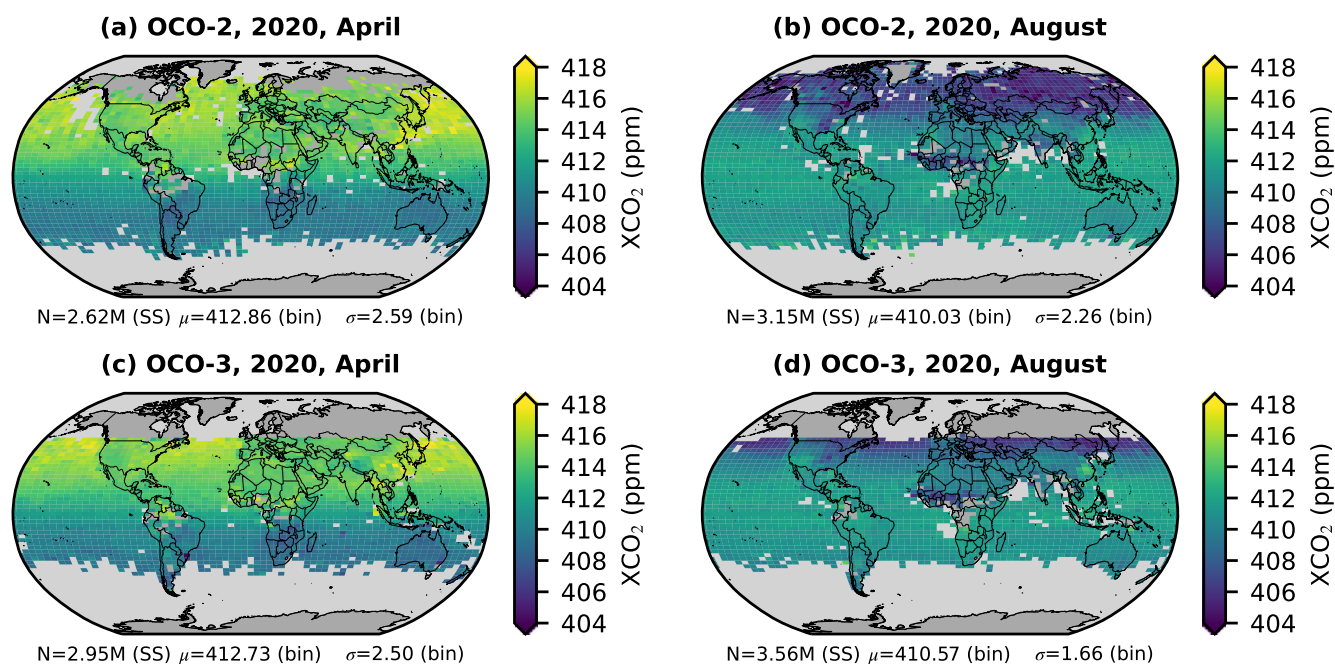
Figure 6. Monthly maps of quality-filtered and bias corrected XCO_2 for OCO-2 (top) and OCO-3 (bottom) for April 2020 (left) and August 2020 (right) at 2.5° latitude by 5.0° longitude resolution. The number of single soundings (SS) are given by N, while the mean (μ) and standard deviation (σ) of the gridded (bin) data are reported. Grid cells with less than 10 soundings are colored gray.

To further demonstrate the agreement between the two sensors, panels (a) and (c) of Fig. 7 show the meridional behavior of XCO_2 for both sensors and observation modes for April and August 2020, respectively. Here, the resolution is $5°$ latitude bins, and the monthly median OCO-2 XCO_2 has been subtracted. In April, when XCO_2 concentrations are near their annual maximums in the extra-tropical northern hemisphere, the meridional gradients are strong over both land and ocean. In August, when

445 the northern hemisphere biosphere is fully active, XCO_2 is within $\approx 1\,ppm$ of the global median for latitudes below approximately $40°\,N$, but much lower than the global average at higher northern latitudes. The difference plots (OCO-3 − OCO-2), shown in panels (b) and (e), indicate that OCO-3 ocean-glint is generally biased low relative to OCO-2 by about 0.3 to 0.4 ppm with uncertainty, σ, of approximately $0.2\,ppm$. For land observations, the differences vary significantly with latitude, making inferences difficult. Panels (c) and (f) show the zonally averaged differences between land and ocean observations, which are

450 expected to be close to zero for both sensors. Based on the results for these particular months, OCO-2 and OCO-3 are in approximate agreement, with land/ocean biases ranging $\approx \pm 2\,ppm$, with significant variation by latitude. These same behaviors were observed for most months in 2020. This latitudinally-dependent land/ocean bias is an unexpected feature of the data set that requires further investigation. The analysis for April and August 2021 (not shown) was qualitatively very similar.

455 Figure 8 shows XCO_2 binned at 10 day by $10°$ latitude for the overlapping time period August 2019 through February 2022 for OCO-2 (top row) and OCO-3 (middle row). Results are shown separately for land (left column) and ocean (right column). Qualitatively, the XCO_2 patterns at this spatiotemporal resolution look very similar, as expected, with maximum XCO_2 in NH spring just before the biospheric drawdown begins, and minimums in NH summer. The plots highlight the secular trend of $\approx 2.2\,ppm/year$, and the seasonal variation in the latitudinal gradient of XCO_2, both important features of the carbon cycle.

460 Again, the substantial time periods where no ocean data is collected by OCO-3 are evident in panel (e).

Due to the vastly different sampling strategies of OCO-2 and OCO-3, coupled with spatial changes in XCO_2 over short time periods, a direct comparison of observed XCO_2 at a global scale is extremely difficult, and can only be used to obtain a rough idea of how the sensors agree. Using the gridded values, the differences for land observations (c) have a mean value of $0.0\,ppm$,

465 standard deviation of $0.67\,ppm$, and a range of $+5$ to $−4\,ppm$. The ocean observations (f) exhibit a mean bias of $−0.26\,ppm$ (OCO-3 lower than OCO-2), with significantly lower uncertainty ($0.45\,ppm$) and min/max ($−1.9/+1.7\,ppm$), compared to land. A more direct and accurate comparison between the two sensors, reported on a small subset of observations with tight spatial and temporal collocation, is discussed in Appendix B3.

470 # 6 Evaluation of OCO v10 XCO_2 estimates versus truth-proxies

This section discusses the evaluation of the OCO v10 good quality-flagged XCO_2 estimates against the truth-proxies used in the quality filtering and bias correction procedure. Although there is some circularity in evaluating the satellite data against the same truth-proxies used for filtering and bias correction, the multi-parameter parametric bias correction is general enough so
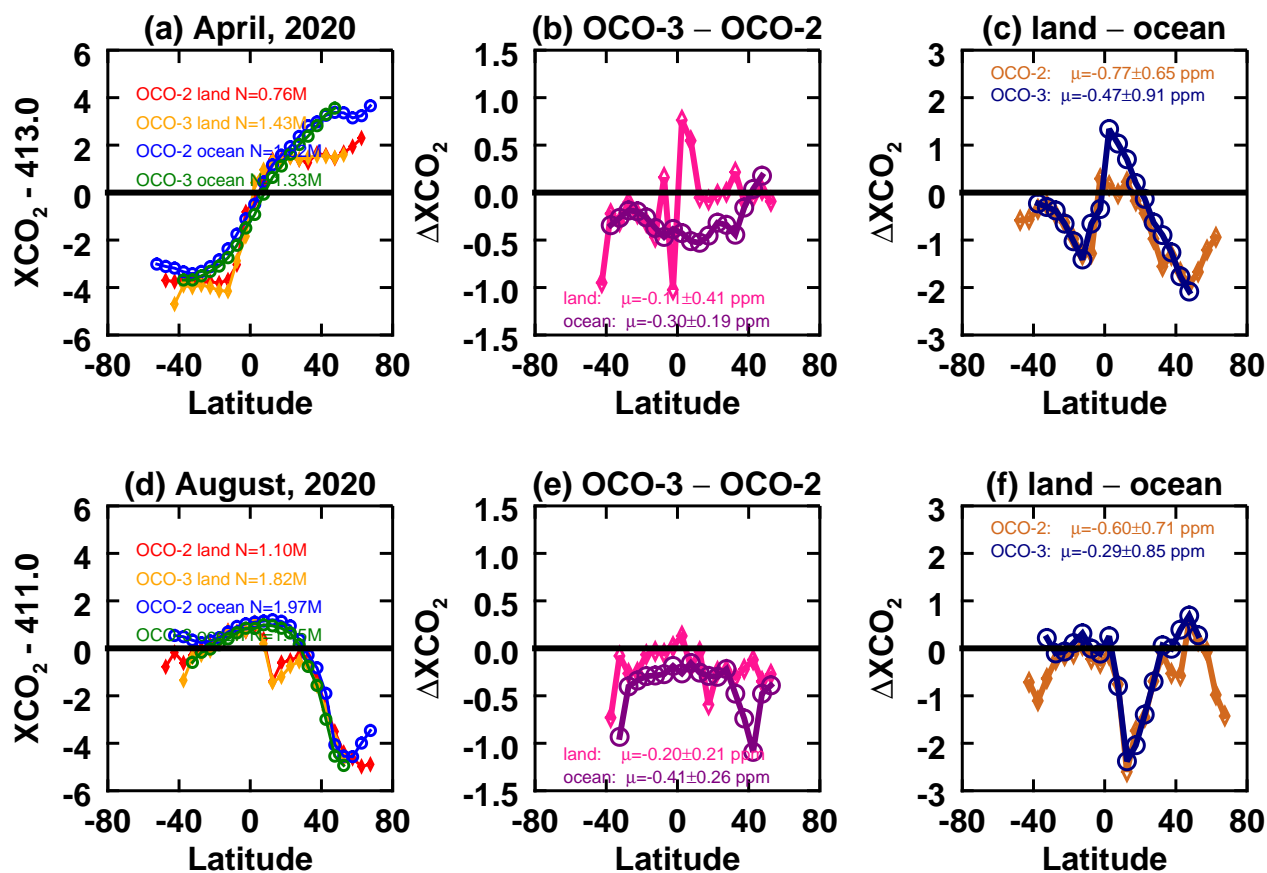
Figure 7. Meridional XCO$_2$ gradients at 5° latitude resolution by sensor and observation mode for April 2020 (a), and August 2020 (d). Only latitude bins containing at least 1000 soundings are shown. The total number of soundings (N) for each sensor and observation mode is given in the legend. Panels (b) and (e) show the differences in the monthly binned values (OCO-3 − OCO-2) for both land (pink diamonds) and ocean (purple circles) observations. Panels (c) and (f) show the differences in the monthly binned values (land − ocean) to demonstrate the land/ocean bias. The mean (μ) and standard deviation (σ) of the binned differences are given in the legend. Here, land observations include land-nadir, land-glint, land-TG and land-SAM, while ocean includes ocean-glint observations.
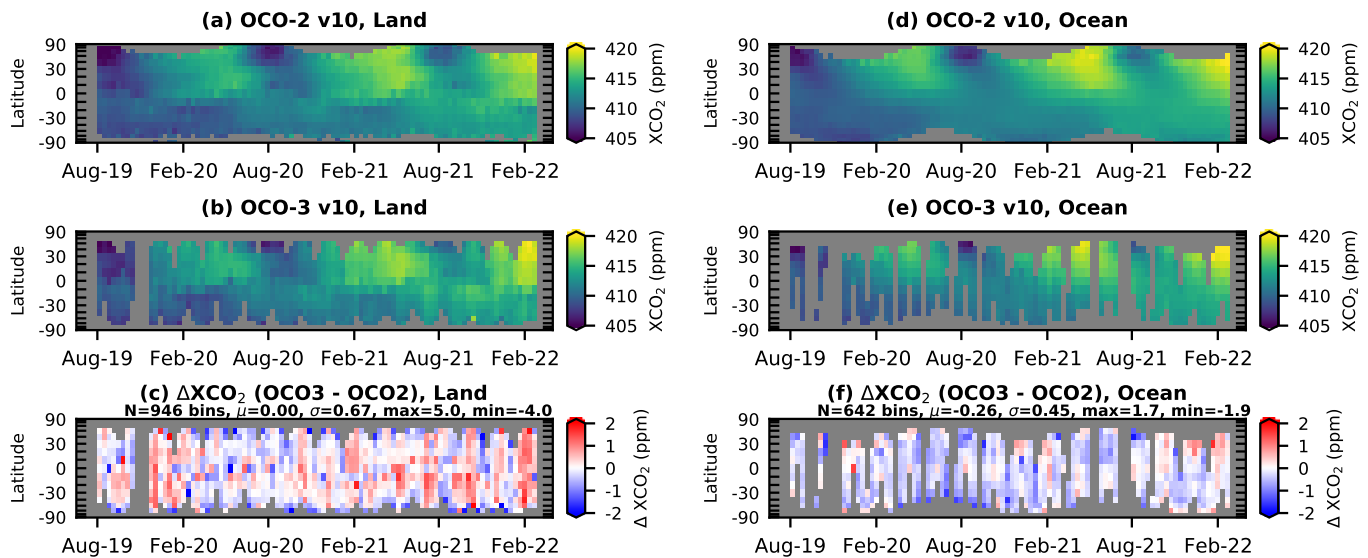
Figure 8. Good quality-flagged and bias corrected XCO$_2$ gridded at 10° latitude by 10 days for the overlapping time period August 2019 through February 2022 for OCO-2 land (a) and OCO-3 land (b). The gridded differences for land observations (includes land-nadir, land-glint, land-TG and land-SAM) are shown in panel (c). Panels (d), (e), (f) are the same, except for ocean-glint observations. The ordinate axis is scaled by the cosine of the latitude to elucidate the decreasing fractional surface area of the earth with increasing latitude. Data cells with less than 10 soundings are colored gray. In panels (c) and (f) the number of valid grid cells (N) is given, along with the mean (μ), standard deviation (σ), and maximum (max) and minimum (min) differences in the gridded values.

as to not over-fit the OCO data. Furthermore, the truth-proxies used for evaluation have been extended in time compared to the data sets used to train the filtering and bias correction. Although it is outside the scope of the current work, OCO-2 data have been validated against a range of other datasets, including in-situ, and NOAA and Aircore vertical observations (Rastogi et al., 2021), aircraft campaigns, e.g. ATom (Kulawik et al., 2019) and ACT-America (Bell et al., 2020), ship-borne and airborne measurements (Müller et al., 2021), and EM27/SUN measurements (Jacobs et al., 2020).

6.1 OCO v10 XCO$_2$ estimates versus TCCON

Section 3.3.1 introduced and discussed the TCCON data as used in the OCO v10 quality filtering and bias correction. Both OCO-2 and OCO-3 were quality filtered and bias corrected against TCCON GGG2014 data, while here TCCON GGG2020 XCO$_2$ estimates are used in the comparison. Key changes to the retrieval algorithm between GGG2014 and GGG2020 are available on the TCCON wiki page (TCCON). The OCO quality-filtering and bias corrections were trained using data through December 2018 for OCO-2 and December 2020 for OCO-3, whereas the validation data extends through February 2022 for OCO-2 and August 2022 for OCO-3. This provides some degree of independence in the evaluation.

Figure 9 shows one-to-one correlation plots of the OCO-2 and OCO-3 v10 XCO_2 estimates versus TCCON GGG2020 estimates, as well as the direct correlation between OCO-2 and OCO-3 using the collocated soundings that are presented in Appendix B. Each point on the graphs represents, for OCO, the mean XCO_2 of the individual soundings acquired on a single overpass within a box 2.5° latitude by 5.0° longitude around a TCCON station. Only overpasses with at least one hundred good quality-flagged OCO soundings within the 2.5° latitude by 5.0° longitude grid box were retained. The TCCON values are the median of the XCO_2 acquired within $\pm 1\,h$ of the OCO overpass.

For the 1121 OCO-2 land collocations (includes land-nadir, land-glint, and land-target) shown in panel (a), and the 259 OCO-3 land collocations (includes land-nadir and land-target) shown in panel (b), the mean biases versus TCCON are 0.24 ppm and 0.12 ppm, respectively, while the uncertainties are 0.77 ppm and 0.90 ppm, respectively. In comparison, the OCO-3 vs. OCO-2 results, using the satellite collocations described in Appendix B, show a mean bias of 0.16 ppm with uncertainty of 0.74 ppm for land (panel (c)). This suggests that OCO-2 and OCO-3 agree with each other about as well as they agree with TCCON for land observations.

For the ocean-glint observations, OCO-2 exhibits a relatively high bias against TCCON of 0.43 ppm, with uncertainty of 0.73 ppm (panel d), while for OCO-3, the bias is 0.09 ppm with uncertainty of 0.90 ppm (panel e). It is important to note however that several of the TCCON stations that provide the bulk of the ocean-glint collocations had not yet processed their measurements through the GGG2020 version of the algorithm to provide estimates of XCO_2. These stations include Ascension Island, Darwin, and Wollongong. When those data are available, more robust statistics will be calculated. Comparison of the OCO-2/3 ocean-glint collocations in panel (f) indicates that the bias between OCO-3 and OCO-2 ocean-glint is -0.34 ppm, with uncertainty 0.44 ppm. This again suggests that the two sensors agree with each other in ocean-glint viewing approximately as well as they agree with TCCON.

6.2 OCO v10 XCO_2 estimates versus models

To assess the impact of OCO XCO_2 estimates on atmospheric inverse models, it is useful to compare the v10 product to results generated by an ensemble of carbon flux inverse models constrained by in situ measurements alone (e.g., O'Dell et al., 2018). This is done by calculating the difference between OCO retrievals from a reference XCO_2 field, where this difference is referred to as the "signal". In the current work, the reference field is computed as the median of posterior concentrations from multiple models constrained by in-situ measurements, and is hereafter referred to as the multi-model-median (MMM). The MMM provides a reasonable representation of XCO_2 with seasonality and trends consistent with information derived from in-situ measurements of atmospheric CO_2, and does not necessarily represent the actual atmosphere at all spatiotemporal scales. This technique for looking at differences between satellite retrievals and modeled fields over broad, zonal regions is not new, and has been employed in the literature for sanity checks (e.g., Chahine et al., 2008; Buchwitz et al., 2017; Zhang et al.,
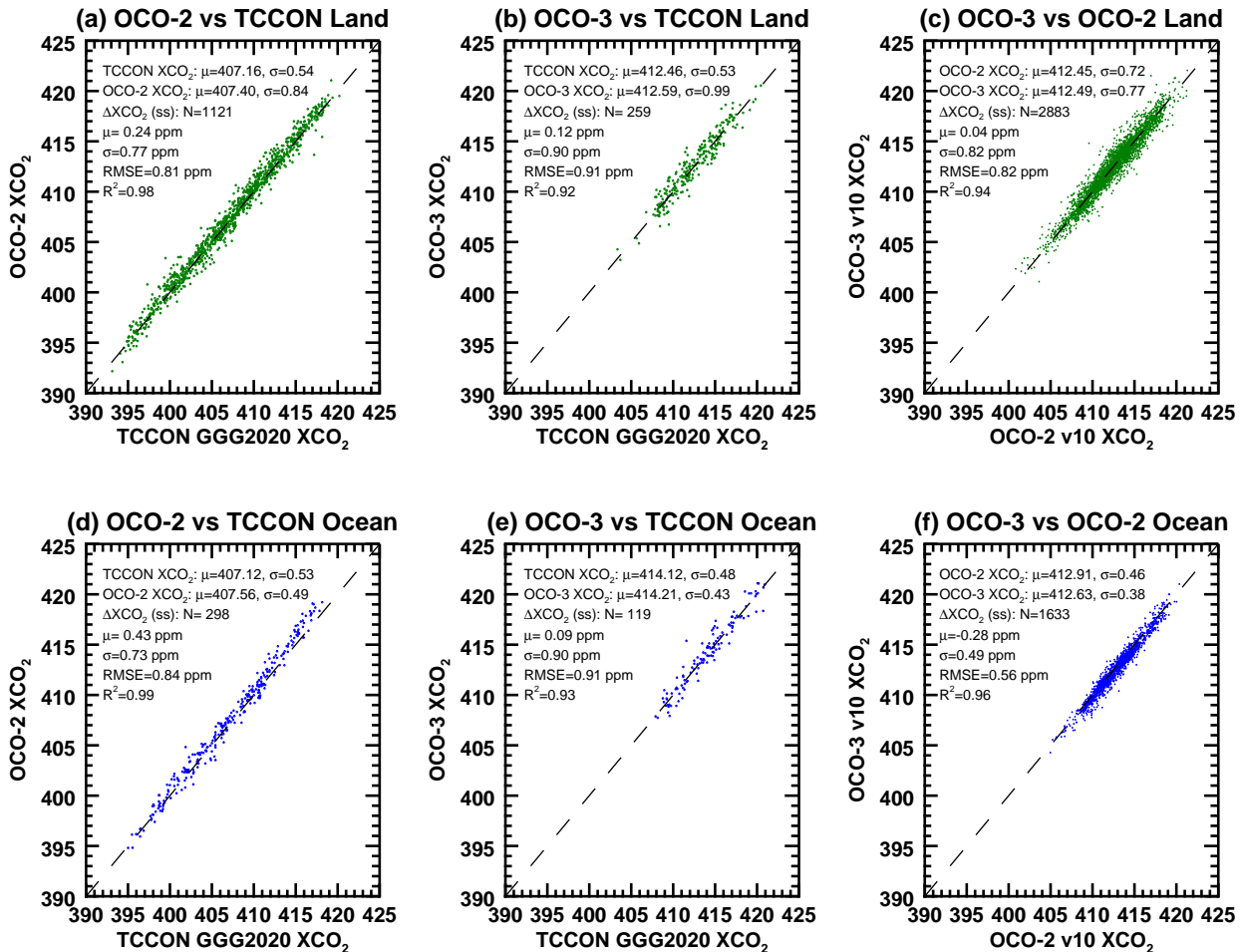
Figure 9. One-to-one XCO_2 correlation plots for land (top row) and ocean (bottom row) observations. Panels (a) and (d) show OCO-2 v10 versus collocated TCCON GGG2020 estimates, while panels (b) and (e) show OCO-3 v10 versus TCCON. Panels (c) and (f) show the correlation in OCO-3 versus OCO-2 XCO_2, respectively, for the set of collocated soundings described in Appendix B3. In each panel, the top two rows of statistics give the mean (μ) of the XCO_2 from all of the collocations, and the mean standard deviation in the XCO_2 (σ) from all of the collocations. The third through seventh rows of statistics give the number of collocations (N), the mean ΔXCO_2, the standard deviation of the ΔXCO_2, the RMSE ($\sqrt{\mu^2 + \sigma^2}$), and the coefficient of determination (R^2 = the squared Pearson linear correlation coefficient).

2017).

One of the contributions of satellite XCO_2 estimates, such as those from OCO-2 and OCO-3, towards improving atmospheric flux inversion estimates is their ability to increase the density of global observations. A well-calibrated and precise satellite data record should offer the potential to reduce some of the uncertainties in the flux estimation associated with sparse sampling.

However, the global atmospheric transport models used in current-generation inversion studies have spatial resolutions of order $2°$ to $6°$ of latitude and longitude. Such models cannot provide information with variability finer than several hundred kilometers. Rather than ingesting each individual OCO-2 XCO_2 estimate falling inside a model grid box, down sampling of the data into ten-second-averages (10-sec-avg) prior to assimilation into inversion systems has become common, e.g., (Crowell et al., 2019; Peiro et al., 2022; Byrne et al., 2023). This provides an even more compact data set with reduced random sounding-to-sounding errors in the XCO_2 estimates and mitigates the potential impact of correlated errors on $\approx 10\,\mathrm{km}$ spatial scales, such as those driven by surface features or the presence of aerosols and clouds (Massie et al., 2021; Mauceri et al., 2023; Massie et al., 2023). Care is taken to specify an appropriate measurement uncertainty, calculated as a function of the number of soundings within the 10-sec-avg bin, individual uncertainties associated with the soundings, coverage across the grid box and correlations between their individual errors (Baker et al., 2022). In this study, XCO_2 from the 10-sec-avg files is used to compare against the relatively spatially coarse model fields.

The models chosen for evaluation of the OCO v10 signal, identified in Section 3.3 and Table 6, all fit the following criteria: (i) each is constrained only by in-situ measurements of CO_2 concentrations in the atmosphere, (ii) each has been evaluated and vetted against independent data in the peer-reviewed literature, (iii) the simulated CO_2 fields and surface fluxes are publicly available, and (iv) each simulation uses different atmospheric transport models and unique inverse modeling framework (Table 5), thus sampling the full range of uncertainties in our present-day state-of-the-art knowledge of the atmospheric CO_2 field.

Figure 10 shows maps of the signal at $2.5°$ by $5°$ lat/lon resolution for April (top row) and August (bottom row), 2020, for OCO-2 (right column) and OCO-3 (middle column). Both sensors exhibit spatially coherent biases against models on the order of half of a ppm. Over oceans, the satellite estimates of XCO_2 are generally biased low relative to the models in the SH and biased high in the NH. However, in the OCO-2 data, which extends further pole-ward compared to OCO-3, the high bias seems to occur at higher latitudes, both north and south. Following expectations, the uncertainty in the gridded data for both sensors in both months is higher for land ($\approx 1\,\mathrm{ppm}$) due to biases associated with topographic and surface albedo variability than it is for ocean ($\approx 0.5\,\mathrm{ppm}$), where these effects are minimal.

The differences in the gridded sensor signals are shown in Fig. 10 panel (c) for April and panel (f) for August. Mathematically, the calculation is expressed as $\Delta\mathrm{signal} = \mathrm{signal}^{\mathrm{OCO\text{-}3}} - \mathrm{signal}^{\mathrm{OCO\text{-}2}}$. Since the satellites sample the models at different times for individual soundings within a grid box, this calculation is not equivalent to a direct difference in the XCO_2 between the

sensors. Rather, it quantifies how different the satellite signals are from the MMM. The Δsignal values demonstrate that the two sensors agree better with each other than they do with the model suite in the region of overlap, as seen by the reduction in uncertainty to ≈ 0.45 ppm, with mean biases around 0.25 ppm in both months. Generally, OCO-3 is biased slightly higher against the MMM over land compared to OCO-2, while over ocean, OCO-3 is biased low against the MMM compared to OCO-2.
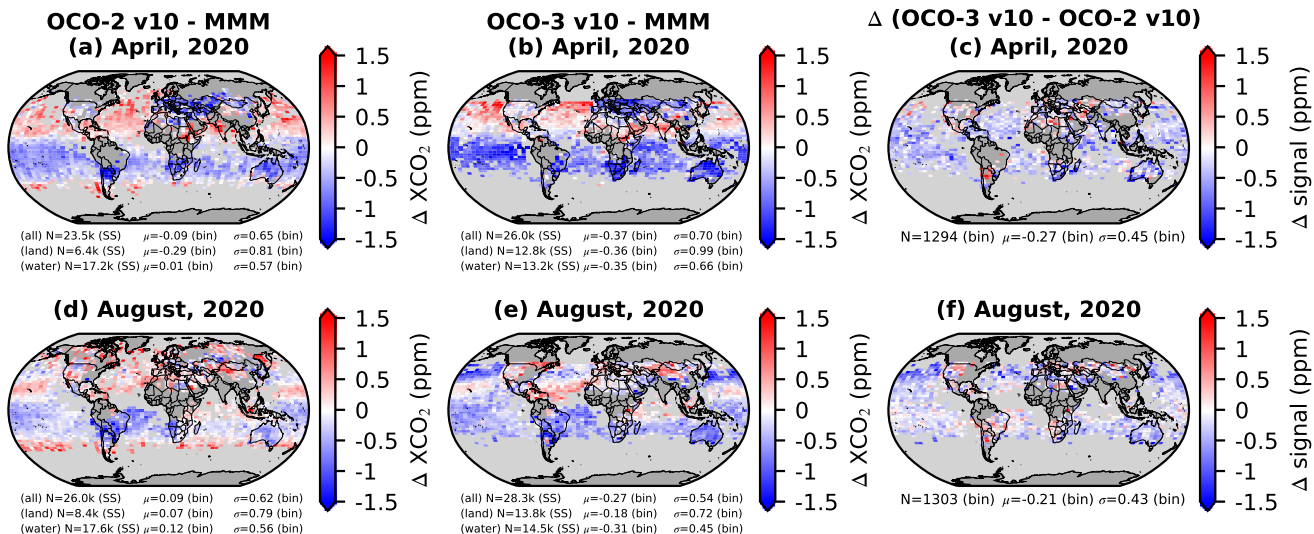
Figure 10. Maps of XCO_2 signal ($XCO_2^{OCO} - XCO_2^{MMM}$) at 2.5° latitude by 5° longitude resolution for April 2020 (top row) and August 2020 (bottom row), for OCO-2 (left) and OCO-3 (middle). The number of single soundings (N SS) for all observation modes combined (all), combined land-nadir, land-glint, land-TG and land-SAM (land), and water-glint (water) are given. The mean (μ) and standard deviation (σ) of the binned values (bin) are also given for each observation mode. Grid cells containing less than 5 soundings are colored gray. Panels (c) and (f) show the Δsignal (OCO-3 $-$ OCO-2), for grid cells in which both sensors have valid data. Here, the statistics are given only for all observation modes combined.

A useful way to investigate the characteristics of the signal is by binning values into zonal (10° latitude) and 10 day bands, as seen in Fig. 11. Here, land observations, which include land-nadir, land-glint, land-TG, and land-SAM, are shown in the left column, and ocean-glint observations on the right, with OCO-2 on the top row and OCO-3 in the middle. The model suite runs only through December of 2020, so the graphs cover a 16 month period, starting in August, 2019. While the zonal mean tends to de-emphasize certain spatial features visible in the global maps, it brings out the temporal variations in the signal. Based on these results, coherent seasonal and latitudinal patterns in the signal are observed for both sensors. For land observations, both sensors tend to have positive signals in the NH and negative signals in the SH, while for ocean-glint observations, the signals tend to be positive poleward of the tropics in both hemispheres, and negative in the tropics. The statistics calculated on the gridded signal data indicate that OCO-3 has higher uncertainty than OCO-2 (0.62 ppm vs. 0.46 ppm) and a larger bias

(-0.30 ppm vs. -0.15 ppm) than OCO-2 for land observations, as seen in panels (a) and (b). The statistics for ocean-glint signals indicate similar uncertainties between the two sensors of 0.53 ppm and 0.59 ppm for OCO-2 and OCO-3, respectively, with mean biases of 0.24 and -0.23 ppm, as seen in panels (d) and (e).

575 The lower two panels of Fig. 11 show the differences in the gridded values (Δ signal) between the two sensors for land observations in panel (c) and for ocean-glint observations in panel (f). The gridded mean difference between the two sensors for land observations is -0.08 ppm. The largest differences for land occur in December 2019, immediately following the OCO-3 PMA calibration that was described in Sec. 2.1.2 of Taylor et al. (2020), and continuing through January 2020 when the next OCO-3 decontamination cycle occurred. The origin of this feature in the OCO-3 v10.4 XCO_2 record is not currently understood. The

580 gridded differences for ocean-glint observations, shown in panel (f) indicate a mean low bias of -0.3 ppm for OCO-3 relative to OCO-2. Overall, as was demonstrated with the maps in Fig. 10, these plots suggest that the two sensors tend to agree better with one another than they do with the model suite.
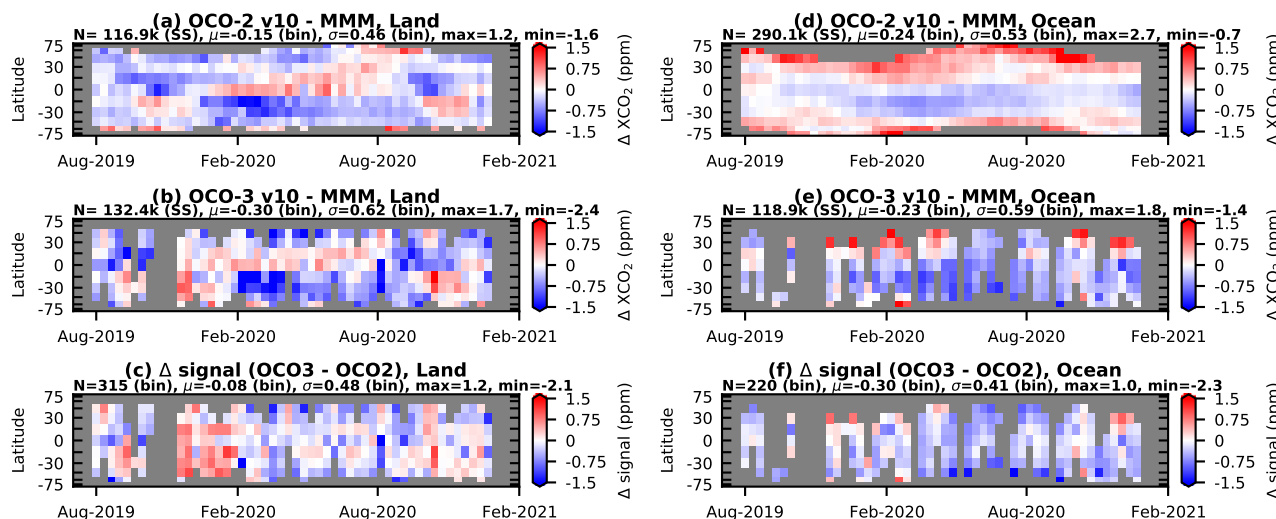
Figure 11. The XCO_2 signal ($XCO_2^{OCO} - XCO_2^{MMM}$) gridded at $10°$ latitude by 10 days for the time period August 2019 through December 2020 for OCO-2 land (a) and OCO-3 land (b). The Δsignal for land observations (includes land-nadir, land-glint, land-TG and land-SAM) are shown in panel (c). Panels (d), (e), (f) are the same, except for ocean-glint observations. The ordinate axis is scaled by the cosine of the latitude to elucidate the decreasing fractional surface area of the earth with increasing latitude. Data cells with less than 10 soundings are colored gray. In panels (a), (b), (d), and (e) the number of single soundings (N SS) is given, along with the mean (μ), standard deviation (σ), and maximum (max) and minimum (min) values of the gridded (bin) values. In panels (c) and (f) the number of valid grid cells (N) is given, along with the mean (μ), standard deviation (σ), and maximum (max) and minimum (min) differences in Δsignal.

6.3 OCO v10 XCO$_2$ estimates over small areas

Small areas, as introduced in Sec. 3.3.1, were used as XCO$_2$ truth-proxies in the development of the v10 quality filtering and bias correction. Small areas can also be used to derive realistic estimates of XCO$_2$ uncertainties for assimilation into inversion systems (Baker et al., 2022; Peiro et al., 2022). For each small area, the "theoretical" uncertainty is calculated as the median value of the XCO$_2$ uncertainties, which are described in Appendix B of O'Dell et al. (2012) and recorded in the L2Lite files. The "actual" uncertainty is calculated as the standard deviation of the retrieved XCO$_2$ in each small area. A minimum of 40 OCO soundings are required for each small area. Ideally, the actual uncertainties are highly correlated to the theoretical uncertainties, with the relationship having a one-to-one dependence (slope, m=1), and the y-intercept falling at zero (y=0). Figures 12 and 13 show the results of an analysis on the small area XCO$_2$ uncertainties for land-nadir and ocean-glint observations, respectively.

The frequency distributions of the XCO$_2$ uncertainties over land-nadir small areas, as shown in panels (a) and (c) of Fig. 12 for OCO-2 and OCO-3, respectively, indicate that the actual uncertainties (green curves) are slightly larger with a wider distribution of values compared to the L2FP noise-driven theoretical uncertainties (blue curves). Although the actual uncertainties tend to be biased high, they are highly correlated with the theoretical uncertainties, having R values of 0.95 and 0.98 for OCO-2 and OCO-3, respectively, as seen in panel (b) and panel (d) for OCO-2 and OCO-3, respectively. Here, the median binned values are shown, rather than the uncertainties for individual small areas, to highlight deviations from the expected one:to:one relationship. These results imply that there are additional spatially-correlated systematic uncertainties in the ACOS retrieval over small areas, and these additional uncertainties are similar for both sensors.

For ocean-glint observations, shown in Fig. 13, XCO$_2$ uncertainties in small areas have different characteristics compared to land observations. The frequency distributions of the XCO$_2$ uncertainties, shown in panels (a) and (c) for OCO-2 and OCO-3, respectively, indicate that the actual uncertainties (green curves) are often lower than the L2FP noise-driven theoretical uncertainties (blue curves), especially for OCO-3. Furthermore, even though the actual uncertainty correlates reasonably well with the theoretical uncertainty (R=0.53 for OCO-2 and R=0.89 for OCO-3), the line-of-best-fit falls well off of the expected one:to:one relationship, with a slope of 0.18 for OCO-2 and 0.31 for OCO-3. For the lowest theoretical uncertainties, the actual uncertainty is near or somewhat higher than anticipated, but when the theoretical uncertainties are large, the actual uncertainties are significantly lower than anticipated. This is unexpected for a well-characterized retrieval, and indicates that there is some non-linearity or other systematic behavior in the v10 ocean-glint retrieval. Early efforts to develop the OCO-2 v11 product suggest this is due to the parameterization of the ocean surface reflectance model. Additional investigation is underway.
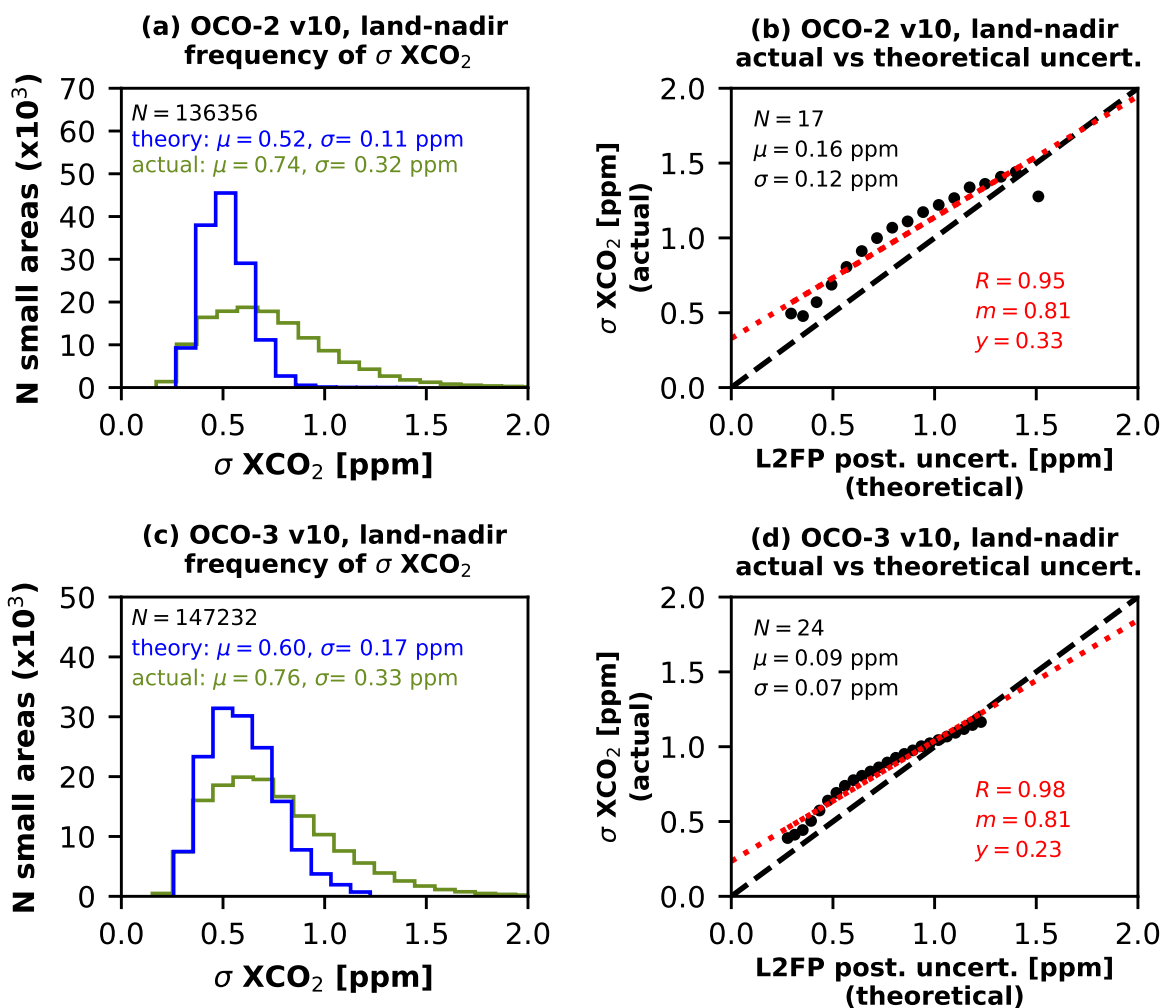
Figure 12. Analysis of XCO_2 uncertainties for land-nadir small areas for OCO-2 (top) and OCO-3 (bottom). Panels (a) and (c) provide the frequency distributions of both the theoretical uncertainties (blue curves) of the retrieved XCO_2 as reported in the L2Lite file product (variable *xco2_uncertainty*) and the actual uncertainties (green curves) calculated from the standard deviation in the XCO_2 for individual small areas. The number of small areas (N) and the mean (μ) and standard deviation (σ) of the theoretical and actual uncertainties are given in the legend. Panels (b) and (d) show the correlation of the actual uncertainties against the theoretical uncertainties, using binned median values (black filled circles) to highlight deviations from the one-to-one line (dashed black line). A least-squares linear fit to the binned data is shown (dotted red line), along with the correlation coefficient (R), the slope of the fit (m) and the fit offset (y).
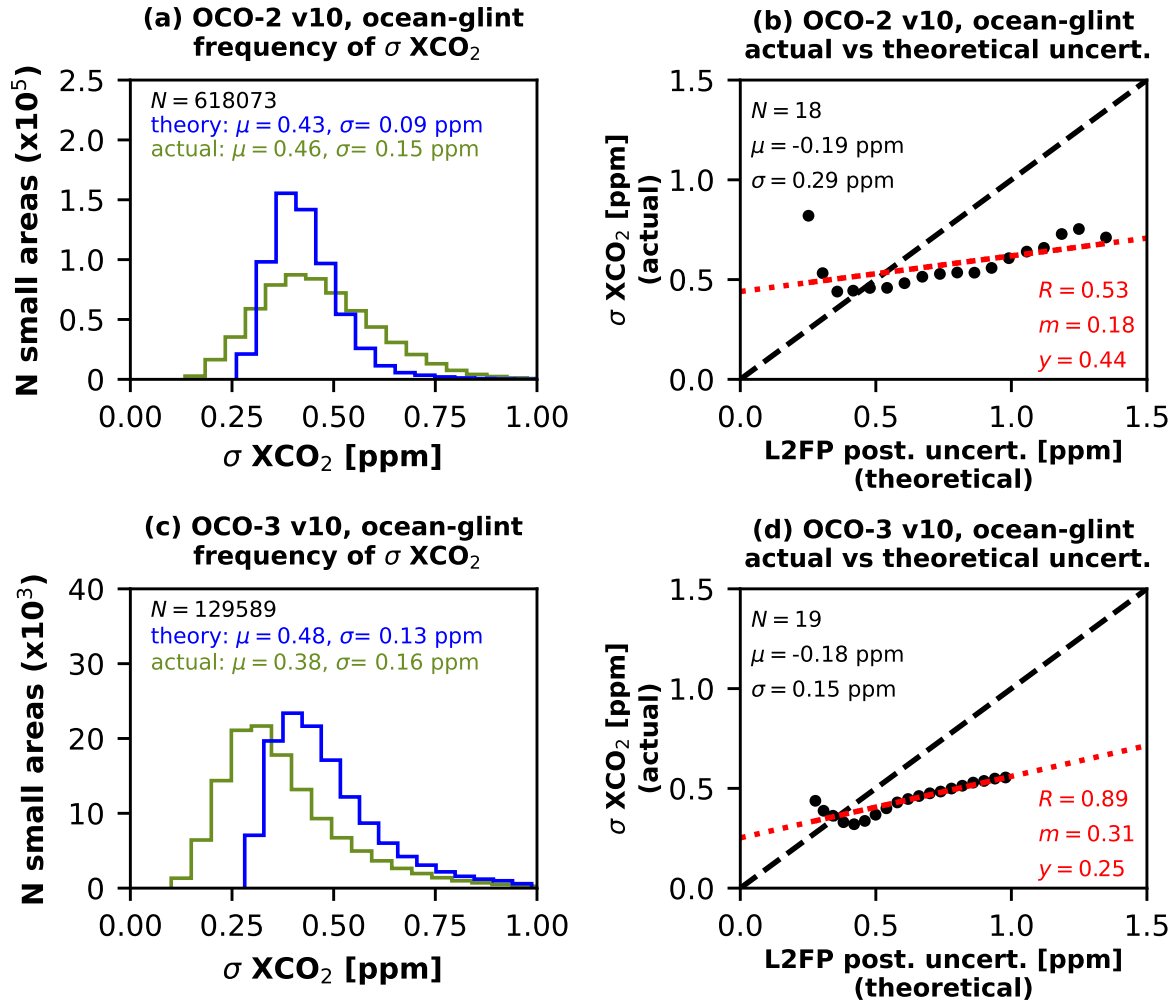
Figure 13. Same as Fig. 12, but for ocean-glint small areas.

6.4 OCO v10 XCO$_2$ estimates along coastal crossings

Although not used in the parametric bias correction, the continuity of XCO$_2$ estimates across coastlines (coastal crossings) provides a metric for detecting and correcting biases between land and ocean estimates of XCO$_2$. Barring strong carbon sources or sinks, the true XCO$_2$ should not change significantly at this transition, so the retrieved estimates should agree quite well. Here, a coastal crossing is defined as a set of contiguous soundings, spanning approximately 50 km on either side of a land/water interface. The XCO$_2$ values are quality filtered and bias corrected and include only glint viewing mode observations for both land and water. For OCO-2 v10, the coastal crossings were used, along with TCCON collocations and model fields, to determine the ocean-glint global scaling factor of 0.995, as described in Section 3.2.3 of the DUG (Osterman et al., 2020). For OCO-3 v10, the coastal crossings alone were used to determine the ocean-glint global scaling factor of 0.9997, as described in Section 4.2.3 of the DUG (Payne et al., 2022).

Figure 14 shows analysis of the coastal crossings data set for the v10 OCO-2 (top row) and OCO-3 (bottom row), containing $\approx 20 \times 10^3$ and 0.5×10^3 crossings, respectively. Panels (a) and (c) show ΔXCO$_2$ in 5° latitude bins with one standard deviation error bars as thin vertical lines. The mean land-ocean difference tends to be positive (negative) in the southern (northern) extra-tropical latitudes for both sensors. Panels (b) and (d) show the frequency distributions of ΔXCO$_2$ for the individual coastal crossings. The means are biased -0.10 ± 0.83 and -0.11 ± 0.88 ppm for OCO-2 and OCO-3, respectively. The uncertainties are due presumably to local geometry, aerosol, and surface effects. In the future, an assessment should be made as to whether these biases can be explained by any retrieved parameters or other independent information such as population centers, which may help to shed light on the cause of these ubiquitous land-ocean XCO$_2$ differences.

7 Summary

This work presents updates to the ACOS v10 retrieval algorithm used to derive estimates of XCO$_2$ from the data collected by both the NASA OCO-2 and OCO-3 sensors. Four substantial changes were made to the L2FP code to provide better estimates of XCO$_2$ relative to v9: (i) use of the ABSCO v5.1 absorption tables, (ii) calculation of more realistic prior aerosol information derived from daily GMAO GEOS-5 FP-IT model output, (iii) an update to the calculation of the CO$_2$ vertical priors based on the GGG2020 algorithm, and (iv) implementation of a new solar continuum model based on TSIS-SIM measurements.

The quality filtering and bias correction implemented in the post-processing of the raw XCO$_2$ estimates for v10 were briefly described. Overall, both the quality filtering and bias correction parameters selected from the training were similar to previous versions. It was shown that, while the efficacy of the quality filtering was similar for both sensors, the bias correction is more effective for OCO-2 than it is for OCO-3 for land observations. The remaining OCO-3 v10 pointing errors (median value of ≈ 0.5 km), coupled with residual instrument calibration errors, may introduce a less accurate surface pressure prior, which affects the efficacy of the dP bias correction term. The cause of a less effective CO$_2$ grad del term in the OCO-3 v10 bias
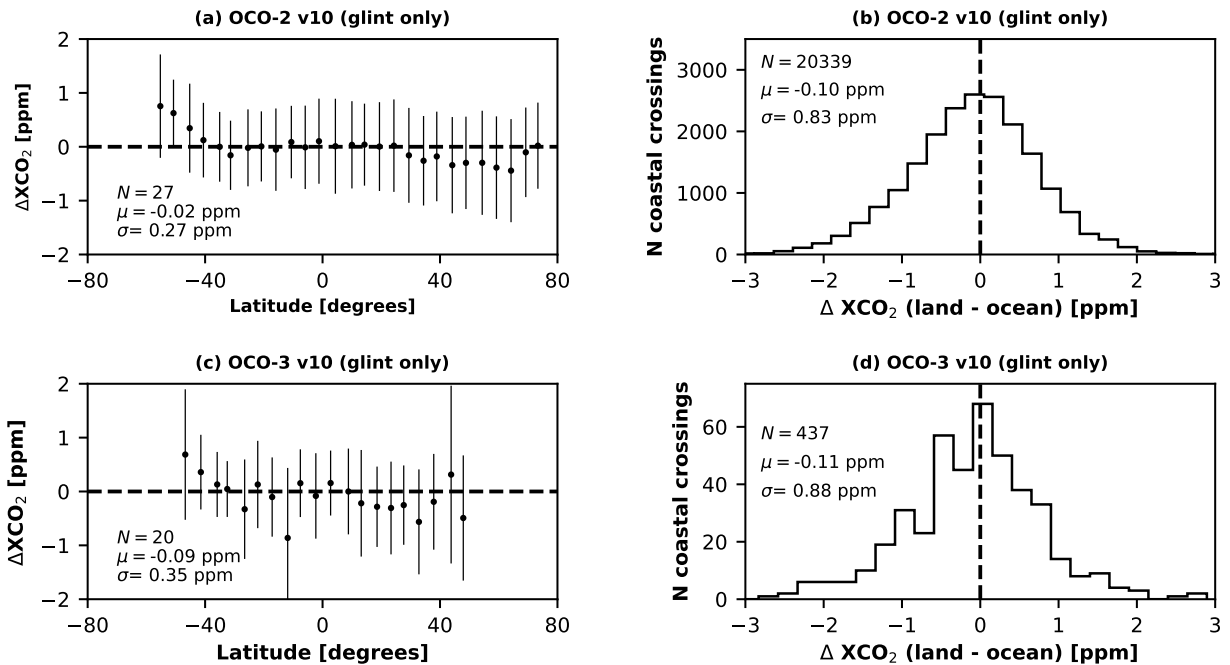
Figure 14. Analysis of the coastal crossings data set for OCO-2 v10 (top row) and OCO-3 v10 (bottom row). Panels (a) and (c) show ΔXCO_2 (land-glint $-$ ocean-glint) in $5°$ latitude bins with one standard deviation error bars as thin vertical lines. The number of latitude bins (N), and the mean (μ) and standard deviation (σ) of the binned values are given in the legend. Panels (b) and (d) show the frequency distributions of ΔXCO_2 for the individual coastal crossings. The number of coastal crossings (N), and the mean (μ) and standard deviation (σ) of the XCO_2 values for the individual crossings are given in the legend.

correction is still not understood.

Although the OCO-2 and OCO-3 sensors are similar, they provide different spatiotemporal coverage from their polar, sun-synchronous (OCO-2) and precessing (OCO-3) orbits. In particular, OCO-2 provides nearly full latitudinal coverage with a local sampling time of $\approx 1{:}36PM \pm 0.25\,h$, while OCO-3 is limited to latitudes $\approx\,\leq 52°$ with variable local sampling time across a 63-day cycle. This work demonstrates, however, that the number of good quality XCO_2 estimates from the two sensors are approximately equal, albeit with different spatiotemporal coverage and quite different splits in observation modes. The OCO-3 sensor provides a larger fraction of good quality soundings in nadir viewing over land, especially around $50°$ N latitude at the orbit inflection point. In addition, for OCO-3, nearly 10% of its good quality-flagged XCO_2 estimates are taken in TG or SAM observation mode, allowing additional opportunities for targeting sites of interest, such as mega-cities and power plants

(Wu et al., 2022; Roten et al., 2022; Lei et al., 2021; Nassar et al., 2022; Chevallier et al., 2022).

In this work, it has been demonstrated that the spatial and temporal distributions of XCO_2 estimates from the OCO-2 and OCO-3 v10 products display the well-known features of the atmospheric distribution of CO_2, including the northern hemisphere spring draw-down, the expected seasonal meridional gradients, and the secular trend of ≈ 2.2 ppm/year. After application of an ad-hoc bias correction to the OCO-3 XCO_2 by way of an L2 Lite file reprocessing to account for a time-dependent drift due to an L1b calibration artifact, the OCO-3 product agrees with OCO-2 within a few tenths of a ppm for a set of collocated soundings. This agreement is of a similar magnitude as the agreement of either sensor with the two truth proxies, TCCON and the multi-model-median, for which RMSEs are on the order of 0.5 to 1 ppm. An analysis against small areas, contiguous regions smaller than 100 km over which the real uncertainty in XCO_2 is expected to be less than ≈ 0.1 ppm, shows that the retrieval posterior uncertainties are underestimated by 20-40% for land observations, while the uncorrelated relationship between actual and theoretical uncertainties for ocean-glint observations suggests deficiencies in the ACOS L2FP v10 ocean surface model. These deficiencies are expected to be mitigated in the next ACOS algorithm version. Additionally, a set of aggregated land-ocean XCO_2 estimates from coastal crossings, used to deduce the global land and ocean scaling factors during the bias correction procedure, show a global mean land-ocean difference of ≤ 0.1 ppm for both sensors, suggesting that the land-ocean bias has been mitigated.

As the science community continues work to better constrain the global carbon cycle (Crisp et al., 2022; Friedlingstein et al., 2022), top-down flux and inventory estimates utilizing XCO_2 observations from space have demonstrated promise for answering key questions about the present and future response of the system to continued human activities and climate change (e.g., Byrne et al., 2021, 2022; Philip et al., 2022; Kong et al., 2022; Chevallier et al., 2022). The need for an international fleet of robust, dedicated carbon monitoring satellites is paramount to this effort (Ciais et al., 2014; Crisp et al., 2018; Janssens-Maenhout et al., 2020; Palmer et al., 2022). The OCO-2 and OCO-3 records, which began in September 2014 and August 2019, respectively, will only gain in significance over time as an early baseline for globally monitoring CO_2 concentrations from space. Overall, the results presented in this work indicate that a set of consistent estimates of XCO_2 from OCO-2 and OCO-3, derived from a single retrieval algorithm (ACOS v10), compare well with one another. This suggests that the simultaneous assimilation of the two data records into atmospheric inversion systems has the potential to provide additional constraints on carbon fluxes, relative to assimilating a single sensor.

Appendix A: OCO-2 v10 full data record and comparison to v9

While the discussion in Sections 4 and 5 focused on the two and half year overlap period with OCO-3, here, the full seven and a half year OCO-2 v10 data record is examined. The use of the OCO-2 v10 data record has already begun to appear in the published literature. Examples include an evaluation of the CO_2 concentrations against the NOAA in situ network (Rastogi et al., 2021), quantification of power plant emissions (Nassar et al., 2021, 2022), detection of urban XCO_2 gradients (Rißmann et al., 2022), a global and regional carbon budget analysis (Kong et al., 2022; Byrne et al., 2022), and an evaluation of global net carbon exchange based on a multi model inter-comparison project (Byrne et al., 2023).

Figure A1 shows a bar chart of the good quality-flagged data volume for the full OCO-2 v10 data record, spanning 6-Sep-2014 through 28-Feb-2022. Here only 1 of the 8 footprints per frame is represented. This figure highlights the stability in the data volume over the seven and a half year OCO-2 v10 record. During approximately the first year of operations, prior to the op-timization of the scanning strategy implemented on 12-Nov-2015 as detailed in Section 5.2 of Crisp et al. (2017), the volume of good quality-flagged data tended to be lower. Overall, the fractions of ocean-glint and land observations match those of the Earth proportions ($\approx 70\%$ and 30%, respectively). Due to the alternating nadir/glint viewing pattern, there is an even split between land-glint and land-nadir. The fraction of TG data is $\approx 1\%$ of the full science record. The most substantial instrument anomaly took place in August and September 2017 due to the temporary failure of the instrument baffle calibrator assembly door. However, regular planned decontamination cycles often interrupt OCO-2 science data acquisition for several days at a time.

Figure A2 shows the OCO-2 v10 XCO_2 binned by latitude ($10°$) and time (10 day) from September 2014 through February 2022 for both land (A) and ocean (B). The dominant features of the atmospheric carbon cycle are observed, namely the secular increase of ≈ 2.2 ppm per year (> 15 ppm over 7.5 years), the seasonal cycle with higher CO_2 concentrations in the NH win-ter/spring, and lower values in the summer/autumn. In addition, the latitudinal dependence of the seasonal cycle is observed. The seven and a half year OCO-2 v10 XCO_2 data record has the potential to allow for examinations of near-decadal long carbon cycle phenomena, as has been done with the eleven and a half year GOSAT v9 record (Jiang et al., 2022).

Figure A3 provides a brief analysis of the CO_2 concentrations and atmospheric growth rates (AGR) calculated from the OCO-2 v10 seven year record. This figure is a reproduction of Fig. 2 in Buchwitz et al. (2018). Shown in panel (a) are the globally averaged, monthly values of XCO_2 for OCO-2 land observations (orange), along with the most recent ACOS GOSAT XCO_2 (v9, Taylor et al. (2022)) in grey, and the global monthly mean marine surface values reported by NOAA GML (Dlugokencky and Tans, 2022) in blue. Here, a cosine of latitude factor has been applied to the satellite data to weight individual soundings for surface area, i.e., higher (lower) weighting in the tropics (high latitudes). It is important to distinguish differences in the NOAA and satellite products. NOAA's values are calculated from precisely calibrated surface observations at a few select locations (Conway et al., 1994), while OCO-2 and GOSAT provide full column measurements with much larger random errors
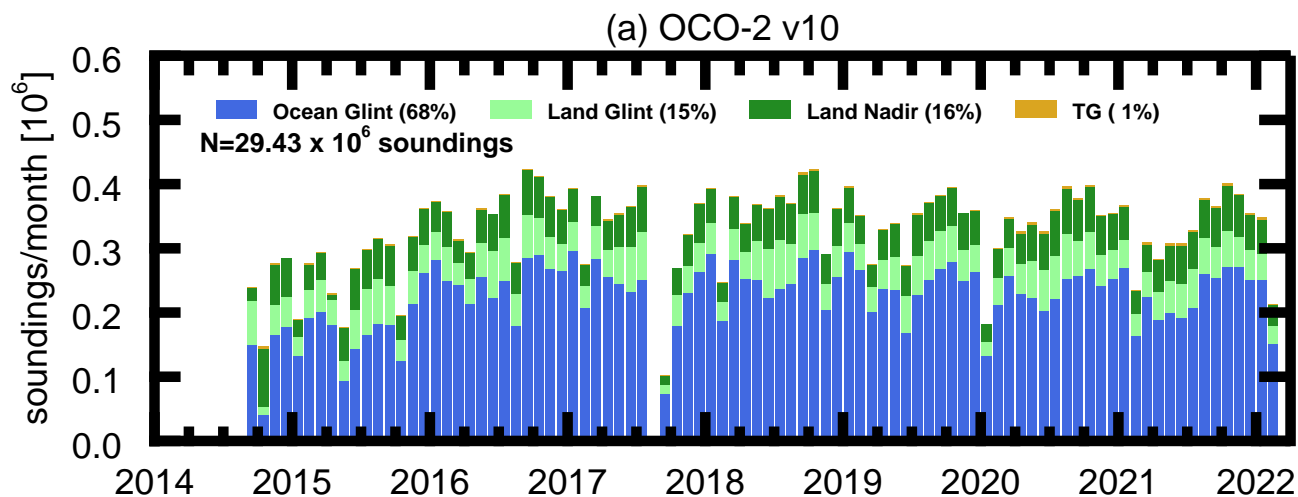
Figure A1. Bar plots of the monthly number of good quality-flagged soundings for a single footprint (4 of 8, 1-based) for the full OCO-2 v10 data record, spanning 6-Sep-2014 through 28-Feb-2022. Observation modes are distinguished by colors. The fractional percent for each observation mode is listed in the legend, along with the total number of soundings (N).
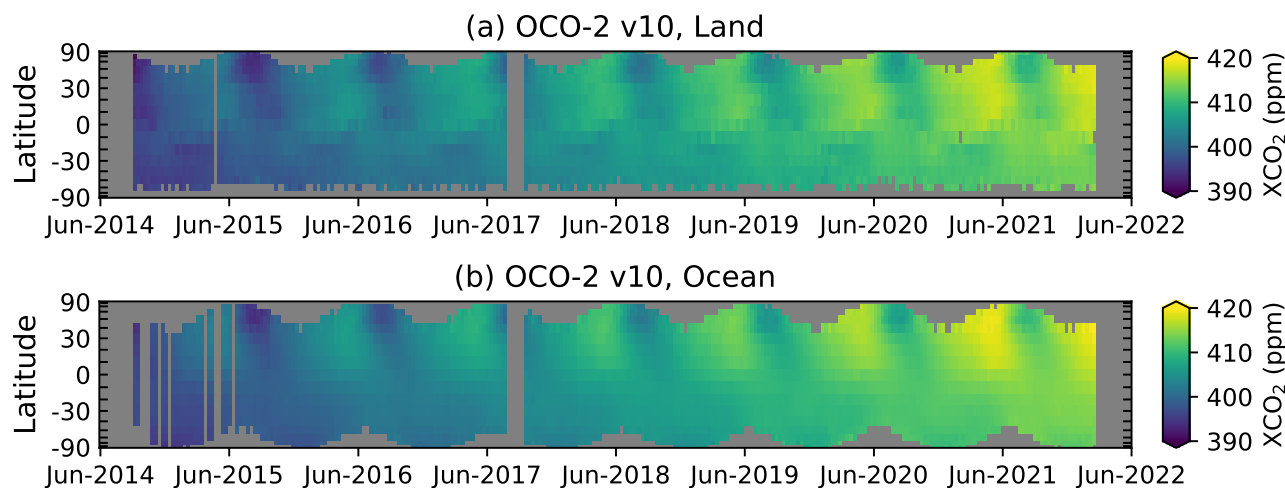
Figure A2. OCO-2 v10 XCO_2 gridded at $10°$ latitude by 10 days for the time period September 2014 through February 2022. Panel (a) includes land-nadir, land-glint, land-TG and land-SAM (Land) soundings, while panel (b) is for ocean-glint soundings. The ordinate axis is scaled by the cosine of the latitude to elucidate the decreasing fractional surface area of the earth with increasing latitude. Grid cells containing less than 10 soundings are colored gray.

720 (instrument plus retrieval), and spatial and temporal sampling biases, but for hundreds to thousands of samples per day.

Panel (b) of Fig. A3 shows the monthly calculated AGRs from the OCO-2 v10 (orange) and GOSAT v9 (gray) data sets. Here the vertical error bars are calculated as the mean of two individual error terms, divided by the number of valid months within a given calendar year. The error terms are (i) the mean value of the XCO_2 uncertainty for individual soundings within the month,

725 and (ii) the mean of the standard deviation of the calculated AGRs within the calendar year. The monthly average OCO-2 AGR over the 7.5 year record is 2.53 ± 0.42 ppm, shown here as a solid line. The dashed lines indicate the $\pm 2\text{-}\sigma$ level. The sharp increase in AGR during the middle of 2015 due to the strong El Niño is observed (Chatterjee et al., 2017; Liu et al., 2017), followed by a slow decreasing period from early 2016 to early 2017. The AGR was then stable through the end of 2018, when a second sharp increase was observed due to the weak 2019 El Niño. After some decline through early 2020, the AGR has

730 remained relatively constant through the end of the reported record (autumn 2021). The GOSAT v9 AGRs agree quite well with the OCO-2 v10 for the overlapping time period.

Panel (c) of Fig. A3 compares the annual growth rates of OCO-2 v10 and GOSAT v9 (the annual mean of the monthly values shown in panel b) to the NOAA GML annual marine surface values. The satellite AGRs generally agrees to within a tenth of a

735 ppm or less. The correlation coefficient across the seven year OCO-2 record is 0.98 with a mean difference of 0.02 ± 0.08 ppm. The maximum difference of 0.13 ppm occurred in 2019, presumably due to the high AGR peak seen by OCO-2 in the first quarter.

To get a sense of the improvement in the OCO-2 v10 XCO_2 product relative to v9, Fig. A4 shows maps of XCO_2 signal

740 ($XCO_2^{OCO} - XCO_2^{MMM}$) at 2.5° latitude by 5° longitude resolution for April (top row) and August (bottom row), 2019 for OCO-2 v9 (left) and OCO-2 v10 (middle). The right column shows the Δsignal (OCO-2 v10 − OCO-2 v9) for grid cells in which both v9 and v10 have valid data. Generally, for April and August 2019, the global bias against models is smaller for OCO-2 v10 (≤ 0.3 ppm) than it was for v9 (≥ 0.5 ppm), with a slight reduction in uncertainty from > 0.65 ppm to ≈ 0.60 ppm. The Δsignal values indicate that OCO-2 v10 XCO_2 is shifted ≈ 0.6 ppm higher than v9. Most of the difference is in the ocean,

745 whereas the changes in land XCO_2 were relatively small between versions. Although the details vary, corresponding plots for other months and years (not shown) look similar.
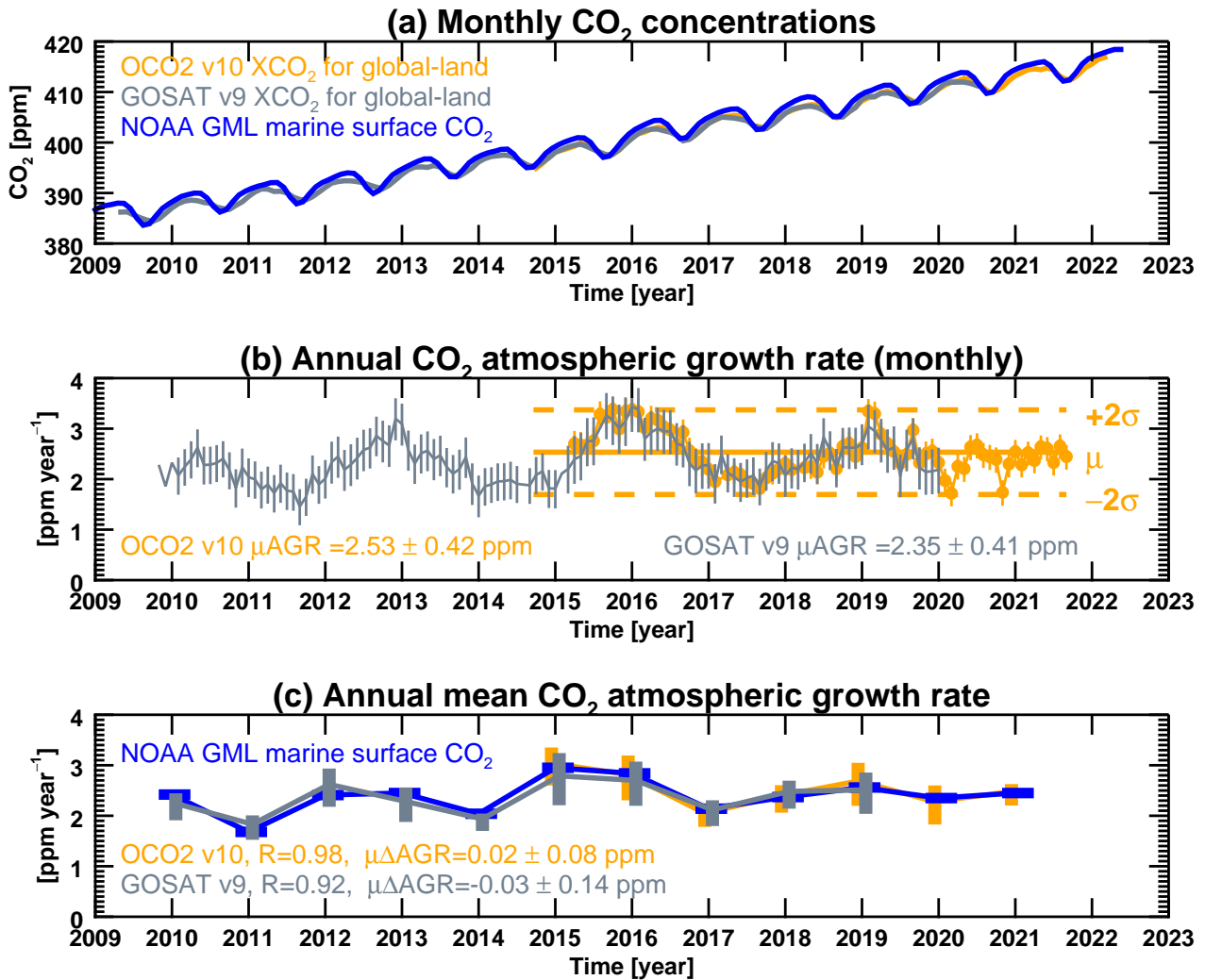
Figure A3. CO_2 concentrations and calculated atmospheric growth rates (AGR) from the OCO-2 v10 data record (orange), with a comparison to ACOS GOSAT v9 (gray) and NOAA GML marine surface values (blue), similar to Fig. 2 in Buchwitz et al. (2018). Panel (a) shows the monthly CO_2 concentrations for each product. Panel (b) shows the calculated monthly values of the AGR with vertical error bars (see text for description of how the error is calculated). The mean (μ) monthly AGR is indicated with corresponding standard deviation. Panel (c) shows the calculated annual AGRs. The linear Pearson correlation coefficient (R) of the satellite versus the NOAA GML values is given, along with the mean difference in the annual AGR ($\mu\Delta$AGR) with corresponding standard deviation.
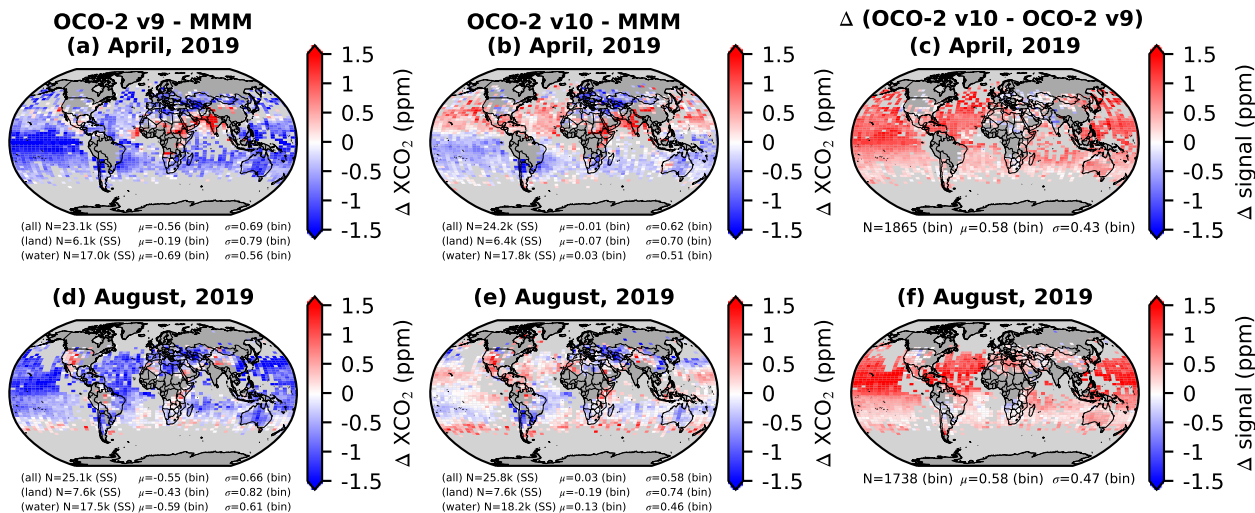
Figure A4. Maps of XCO$_2$ signal (XCO$_2^{OCO}$ − XCO$_2^{MMM}$) at 2.5° latitude by 5° longitude resolution for April 2019 (top row) and August 2019 (bottom row), for OCO-2 v9 (left) and OCO-2 v10 (middle). The number of single soundings (N SS) for all observation modes combined (all), combined land-nadir, land-glint, land-TG and land-SAM (land), and water-glint (water) are given. The mean (μ) and standard deviation (σ) of the binned values (bin) are also given for each observation mode. Grid cells containing less than 5 soundings are colored gray. Panels (c) and (f) show the Δsignal (OCO-2 v10 − OCO-2 v9) for grid cells in which both sensors have valid data. Here, the statistics are given only for all observation modes combined.

Appendix B: OCO-3 v10

B1 OCO-3 operations

750 As was discussed in Taylor et al. (2020), the collection of science data by OCO-3 is often interrupted by either the Hunstville Operations Support Center (HOSC) or the Mission Operations System (MOS) at JPL. The former are generally due to arriving or departing vehicles from the ISS, or other ISS activities such as spacewalks or instrument out-gassing events. OCO-3 also suffers from data drop-outs in ocean-glint viewing due to physical obstructions within the field of view, e.g., solar panels.

755 Table B1 shows the statistics at a per-granule (orbit) level for OCO-3 from August 2019 through February 2022. Over the course of these 31 months, HOSC interrupts occurred for ≈ 9% (1329) of the total number of granules (14,527), while MOS interrupts occurred for ≈ 8% (1038) of the observable granules (13,198), yielding 12,160 granules containing science measurements (≈ 92% of the observable, 84% of total). This well exceeds the mission requirement of 50% data acquisition.

Table B1. Monthly statistics of the OCO-3 collection for the period August 2019 through February 2022.

Month	Total Number of Orbits	Orbits containing HOSC interrupts (% of total)	Number of Observable Orbits (% of total)	Orbits containing MOS interrupts (% of observable)	Number of Collected Orbits (% of observable)
Aug (2019)	402	99 (24.6%)	303 (75.4%)	34 (11.2%)	269 (88.8%)
Sep (2019)	465	34 (7.3%)	431 (92.7%)	60 (13.9%)	371 (86.1%)
Oct (2019)	481	176 (36.6%)	305 (63.4%)	127 (41.6%)	178 (58.4%)
Nov (2019)	465	40 (8.6%)	425 (91.4%)	382 (89.9%)	43 (10.1%)
Dec (2019)	481	92 (19.1%)	389 (80.9%)	0 (0.0%)	389 (100.0%)
Jan (2020)	480	90 (18.8%)	390 (81.2%)	16 (4.1%)	374 (95.9%)
Feb (2020)	449	74 (16.5%)	375 (83.5%)	21 (5.6%)	354 (94.4%)
Mar (2020)	480	34 (7.1%)	446 (92.9%)	6 (1.3%)	440 (98.7%)
Apr (2020)	465	33 (7.1%)	432 (92.9%)	8 (1.9%)	424 (98.1%)
May (2020)	480	21 (4.4%)	459 (95.6%)	9 (2.0%)	450 (98.0%)
Jun (2020)	464	0 (0.0%)	464 (100.0%)	46 (9.9%)	418 (90.1%)
Jul (2020)	480	31 (6.5%)	449 (93.5%)	0 (0.0%)	449 (100.0%)
Aug (2020)	480	8 (1.7%)	472 (98.3%)	0 (0.0%)	472 (100.0%)
Sep (2020)	465	2 (0.4%)	463 (99.6%)	8 (1.7%)	455 (98.3%)
Oct (2020)	480	31 (6.5%)	449 (93.5%)	2 (0.4%)	447 (99.6%)
Nov (2020)	465	7 (1.5%)	458 (98.5%)	0 (0.0%)	458 (100.0%)
Dec (2020)	480	11 (2.3%)	469 (97.7%)	4 (0.9%)	465 (99.1%)
Jan (2021)	480	16 (3.3%)	464 (96.7%)	56 (12.1%)	408 (87.9%)
Feb (2021)	433	36 (8.3%)	397 (91.7%)	26 (6.5%)	371 (93.5%)
Mar (2021)	480	11 (2.3%)	469 (97.7%)	0 (0.0%)	469 (100.0%)
Apr (2021)	465	25 (5.4%)	440 (94.6%)	26 (5.9%)	414 (94.1%)
May (2021)	480	0 (0.0%)	480 (100.0%)	31 (6.5%)	449 (93.5%)
Jun (2021)	464	13 (2.8%)	451 (97.2%)	1 (0.2%)	450 (99.8%)
Jul (2021)	480	71 (14.8%)	409 (85.2%)	0 (0.0%)	409 (100.0%)
Aug (2021)	480	63 (13.1%)	417 (86.9%)	48 (11.5%)	369 (88.5%)
Sep (2021)	464	13 (2.8%)	451 (97.2%)	0 (0.0%)	451 (100.0%)
Oct (2021)	480	38 (7.9%)	442 (92.1%)	0 (0.0%)	442 (100.0%)
Nov (2021)	465	81 (17.4%)	384 (82.6%)	0 (0.0%)	384 (100.0%)
Dec (2021)	480	65 (13.5%)	415 (86.5%)	50 (12.0%)	365 (88.0%)
Jan (2022)	480	88 (18.3%)	392 (81.7%)	31 (7.9%)	361 (92.1%)
Feb (2022)	434	26 (6.0%)	408 (94.0%)	46 (11.3%)	362 (88.7%)
Grand Total	14527	1329 (9.2%)	13198 (90.8%)	1038 (8.3%)	12160 (91.7%)

B2   OCO-3 v10 pointing correction

Although the first public release of OCO-3 XCO$_2$ (vEarly) was derived using the v10 L2FP algorithm, the data set suffered from significant geolocation errors (Taylor et al., 2020). Here, an update in the geolocation for v10 is described.

Precise geolocation of OCO-3 footprints requires knowledge of (i) the position and attitude of the instrument in space, (ii) the position and control of the PMA, and (iii) the effective alignment of the OCO-3 detectors with respect to the instrument reference. Improvements were made in all three areas for v10, as described in Section 2.2 of the OCO-3 v10.4 data quality statement (Chatterjee et al., 2022). OCO-3 attitude data are now taken primarily from the on-board stellar reference unit (SRU), which was not possible for vEarly due to a systems timing error that yielded large geolocation errors early in the mission. When the SRU is not available for attitude information, the OCO-3 processing stream relies on stellar reference data from the CALorimetric Electron Telescope (CALET) (Torii and Marrocchesi, 2019), another instrument aboard the ISS JEM-EF. During early operations, the PMA was calibrated using measurements from the on-board internal context camera (ICC), and an external look-up table was derived for azimuth and elevation angle offsets. For v10, a model fit to the PMA calibration data was implemented directly into the geolocation algorithm. Finally, for OCO-3 v10, the effective alignment of the detectors to the instrument reference was empirically determined using a best-fit static alignment adjustment. An additional rotation element was added to the geolocation algorithm, and the relative alignment space was systematically explored using a metric derived from minimizing surface pressure errors and albedo differences. This removed a systematic pointing error of 1 to 2 km. Overall, adjustments to the OCO-3 geolocation led to an improvement in the pointing errors from 1-2 km in vEarly down to typically less than 1 km in v10. Further refinements to OCO-3 geolocation are expected in future versions.

To confirm the v10 pointing errors, a pointing optimization code was developed to examine the residual errors for individual swaths within a collection of SAMs. The code minimizes a cost function using the difference in retrieved and modeled surface pressure (the L2FP prior), coupled with differences in the weak CO$_2$ surface albedo between the retrieved values from the IDP and the black-sky albedo from MODIS Band 6, using the closest-in-time available MODIS Albedo file (1 km resolution, product MCD43A3, Schaaf (2022)). The primary result of the code is an optimal shift in latitude and longitude for each swath in a given OCO-3 SAM or Target observation, to bring it into alignment with the ancillary data. Note that SAM swaths are not actually displaced by the suggested optimization values within the v10.4 data products, and thus geolocation errors typically up to 1 km remain in OCO-3 v10 data. However, for future reprocessing, a final optimization on all SAMs in the data collection prior to public release may be considered, depending on the residual errors. In specific instances, the project has supported requests to optimize individual SAMs in support of science analysis, as was done for Nassar et al. (2022).

Figure B1 shows analysis of the OCO-3 v10 pointing offset optimization results for a set of a few hundred SAMs collected over an approximate one year period. As each SAM consists of between 4 and 6 swaths, the total swath count is 372, after several quality assurance criteria are applied based on the certainty of the results for each fit. Panel (a) provides the frequency

distribution of the optimization distance (Δ d) for vEarly (pink) and v10 (blue). While the mean/median Δ d was ≈ 1.5 km in vEarly, for v10 the optimization distance has been reduced to ≈ 0.5 km.

795

Panel (b) of Fig. B1 shows the cumulative frequency distribution, which indicates that for vEarly $\approx 65\%$ of the swaths had Δ d > 1.25 km, while for v10 the fraction of swaths with Δ d > 1.25 km has been reduced to $\approx 15\%$. In the vEarly product, more than 7% of the swaths had Δ d < 2.5 km, while for v10, less than 1% of the swaths have a pointing error greater than 2.5 km. Recall that the nominal size of an OCO-3 footprint is 1.6 by 2.2 km. Additional reductions in the OCO-3 pointing error to the

800   sub 0.5 km level, on order with OCO-2 (Kiel et al., 2019) is the nominal goal for a future reprocessing.

B3   OCO-3 v10 ad hoc XCO$_2$ bias correction

The ad hoc correction to OCO-3 v10 XCO$_2$ using collocated OCO-2 data is predicated upon the hypothesis that two sensors measuring the same column of air at the same time should produce the same XCO$_2$ estimate when derived using the same

805   retrieval algorithm. Therefore, a set of spatiotemporal collocations between the OCO-2 and OCO-3 sensors was identified over the time period 6-Aug-2019 through 31-Oct-2021. If the XCO$_2$ from the two sensors are in good agreement, the expectation is for a mean bias close to zero, with low variability, and no time trend.

Each OCO-2/3 collocation consists of a cluster of soundings for each of the two sensors measured within a 25 km radius and

810   ± 4 h time, and containing at least 15 good quality flagged soundings per sensor. The difference in the mean bias corrected XCO$_2$ (μ) for each collocated cluster of soundings (ΔXCO$_2 = \mu$ OCO-3 $- \mu$ OCO-2) provides a reasonably direct comparison between the sensors.

Figure B2 provides two example visualizations of overlapping orbit tracks from OCO-2 and OCO-3 as measured over eastern

815   Europe on 12-August-2019 (A) and over the southwest coast of Africa on 22-September-2021 (B). In example (A) the time difference between the overpasses was < 5 minutes, with a ΔXCO$_2$ of 0.17 ppm. In example (B), the time difference was 25 minutes, with a ΔXCO$_2$ of 0.01 ppm. The variability in XCO$_2$ for the entire scene was about 0.5-0.8 ppm for both sensors.

Time series plots of the ΔXCO$_2$, as shown in panel (a) of Fig. B3 suggests a significant divergence in ΔXCO$_2$ between orbits

820   4339 to 9719 (February 2020 through January 2021). This time period corresponds to a long interval with no instrument decontamination, which are indicated by the shaded areas in the plot. Upon investigation, it was found that the diverging ΔXCO$_2$ correlates with an OCO-3 L1b calibration artifact: the instrument stray light, or zero-level-offset (ZLO), as shown in panel (b). The band-dependent ZLO is derived from measurements of the on-board calibration lamps on the unilluminated pixels of the detector, and is found to increase non-linearly in time since the last decontamination cycle, as shown against the left ordinate

825   in panel (c).
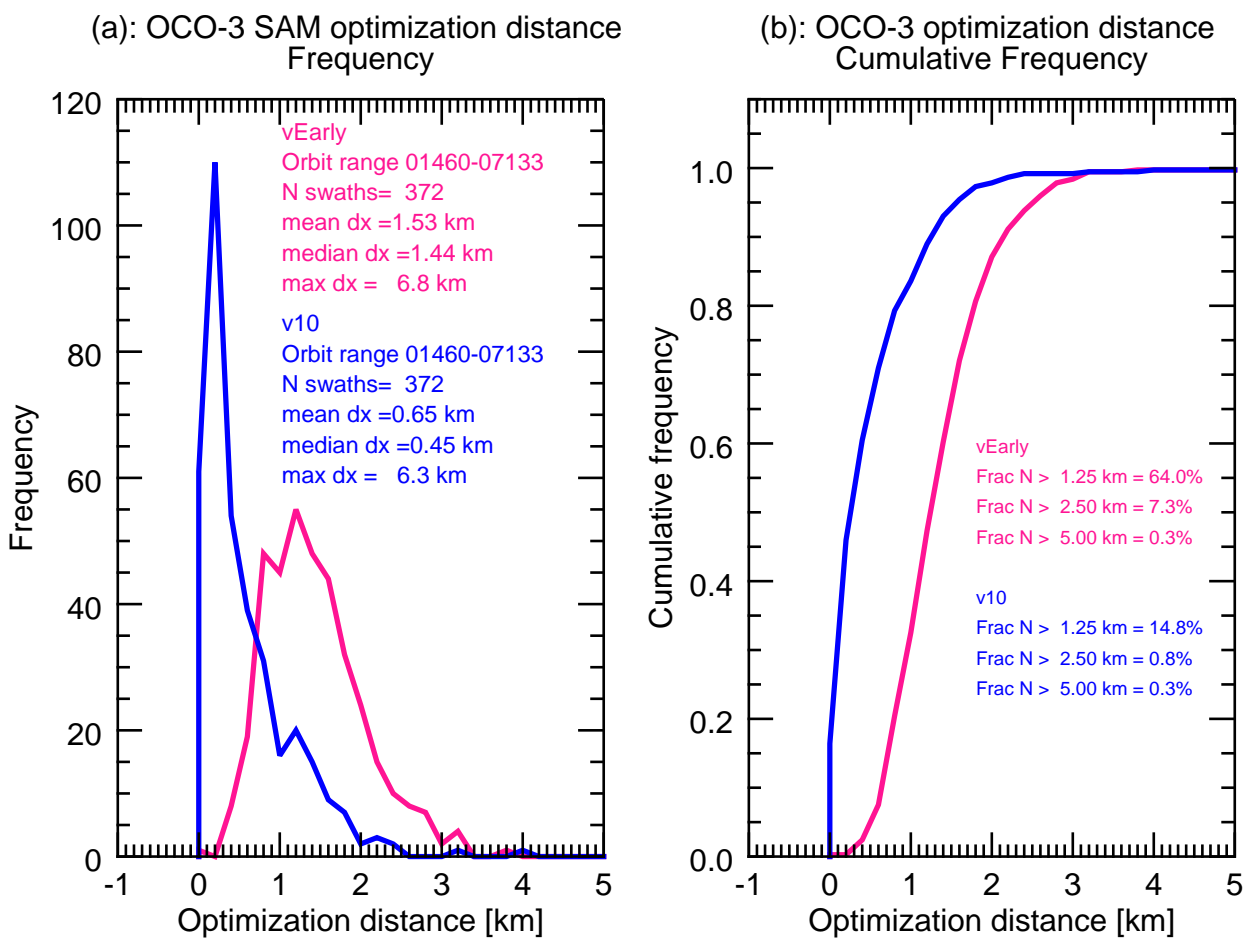
Figure B1. Comparison of OCO-3 pointing optimization for vEarly (pink) and v10 (blue) spanning an approximately one year time period. Panel (a) shows the frequency distribution of the optimization distance. The orbit ranges and number of swaths are indicated in the legend, along with the mean, median, and maximum optimization distances (dx) in kilometers. Panel (b) shows the cumulative frequency distributions. The percent of the swaths (Frac N) with optimization distances greater than 1.25 km, 2.5 km, and 5.0 km are indicated in the legend.
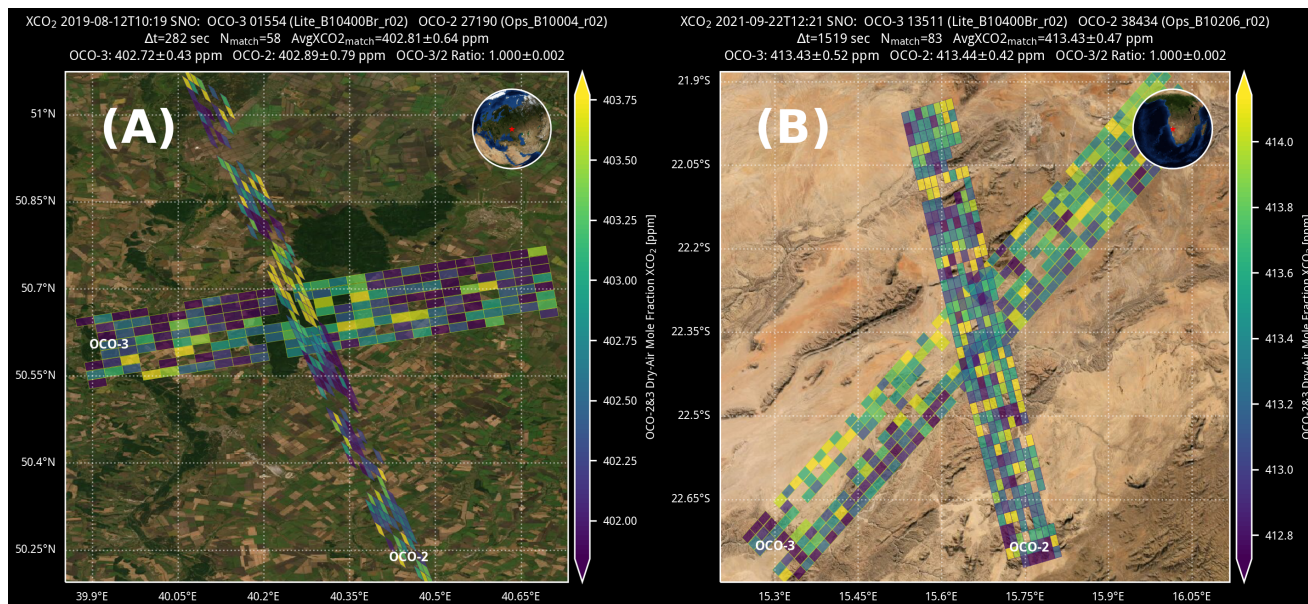
Figure B2. XCO$_2$ from simultaneous nadir overpasses (SNOs) between the OCO-2 and OCO-3 over eastern Europe on 12-August-2019 (A) and over the southwest coast of Africa on 22-September-2021 (B). In example (A) the time difference between the overpasses was 282 s (< 5 m) and the difference in the average XCO$_2$ from the two sensors was 0.17 ppm. In example (B), the time difference was 1519 s (25 m) and the difference in the average XCO$_2$ from the two sensors was 0.01 ppm. The uncertainty in XCO$_2$ for the entire scene was about 0.5 to 0.8 ppm for both sensors. The background for these image comes from ArcGIS, available at https://server.arcgisonline.com/ArcGIS/rest/services. Note that the collocation criteria used in this work (25 km radius and ± 4 h) means that not all collocations were direct simultaneous overpasses, and a mixture of both nadir and glint viewing was used.

A correction to the OCO-3 XCO$_2$ values (right ordinate of panel (c)) is derived from a linear fit of the ΔXCO$_2$ (at a given orbit) versus the WCO$_2$ ZLO at the same orbit (panel b). After application of this ad hoc correction, the time dependence of ΔXCO$_2$ between OCO-2 and OCO-3 is largely mitigated, as shown in panel (d). Fit coefficients were determined separately
830 for each OCO-3 FP and for land and ocean-glint observations. A reprocessing of the OCO-3 L2 Lite product was performed to correct the XCO$_2$ for all reported soundings. The new v10.4 L2 Lite XCO$_2$ files were delivered to the NASA GES DISC in April of 2022 (Chatterjee et al., 2022). The files contain a new variable field, *Retrieval/xco2_zlo_bias*, giving the size of the additive correction made to the XCO$_2$ values. Researchers are urged to use these files, and avoid use of the XCO$_2$ reported in the L2 Standard product which do not have the ad hoc bias correction applied.

835

Figure B5 shows a verification of the OCO-3 XCO$_2$ ad hoc correction as compared to the multi-model-median (MMM) that was discussed in Section 6.2. The top row shows results prior to the ad hoc correction for land-nadir (a) and for ocean-glint (b). Although early in the record, the agreement is quite good, a strong, unexpected time divergence is seen in the uncorrected
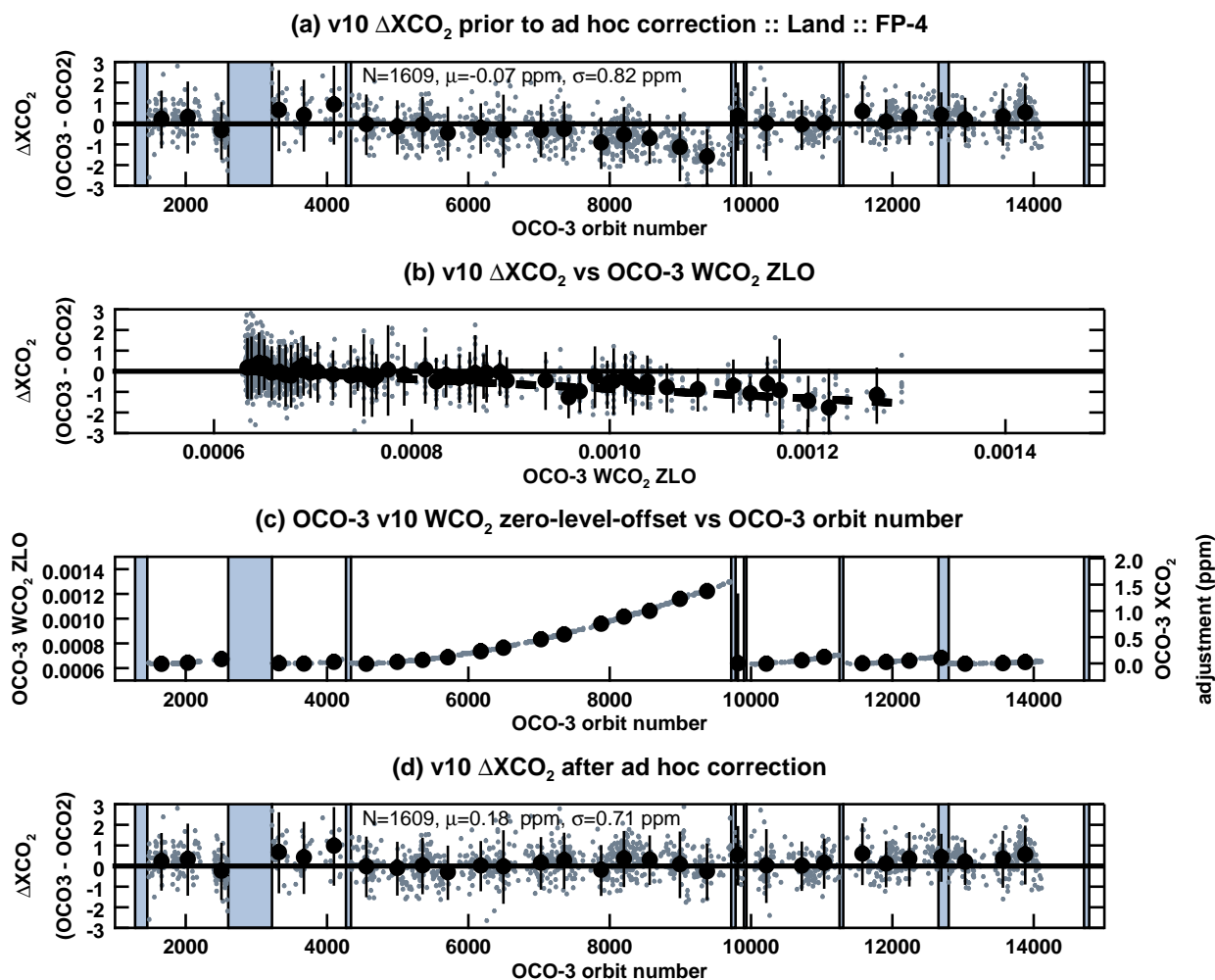
Figure B3. Ad hoc bias correction of OCO-3 v10 XCO_2 for footprint 4 (FP-4) land measurements. Panel (a) shows the ΔXCO_2 (OCO-3 − OCO-2) for a set of collocated clusters of soundings versus the OCO-3 orbit number. The number of collocations (N), and the mean (μ) and standard deviation (σ) of the ΔXCO_2 are given in the legend. Panel (b) shows the correlation between the ΔXCO_2 and the OCO-3 WCO_2 ZLO used to determine the correction. Panel (c) shows the OCO-3 WCO_2 ZLO (left) and magnitude in ppm of the ad hoc XCO_2 bias correction (right) versus OCO-3 orbit number. Panel (d) is similar to panel (a), except with the OCO-3 XCO_2 ad hoc correction applied. In all panels, the small grey dots indicate individual collocations, while the large black dots are binned median values. The vertical shaded regions in panels (a), (c), and (d) indicate the time period during which the OCO-3 instrument was powered down for a decontamination cycle.
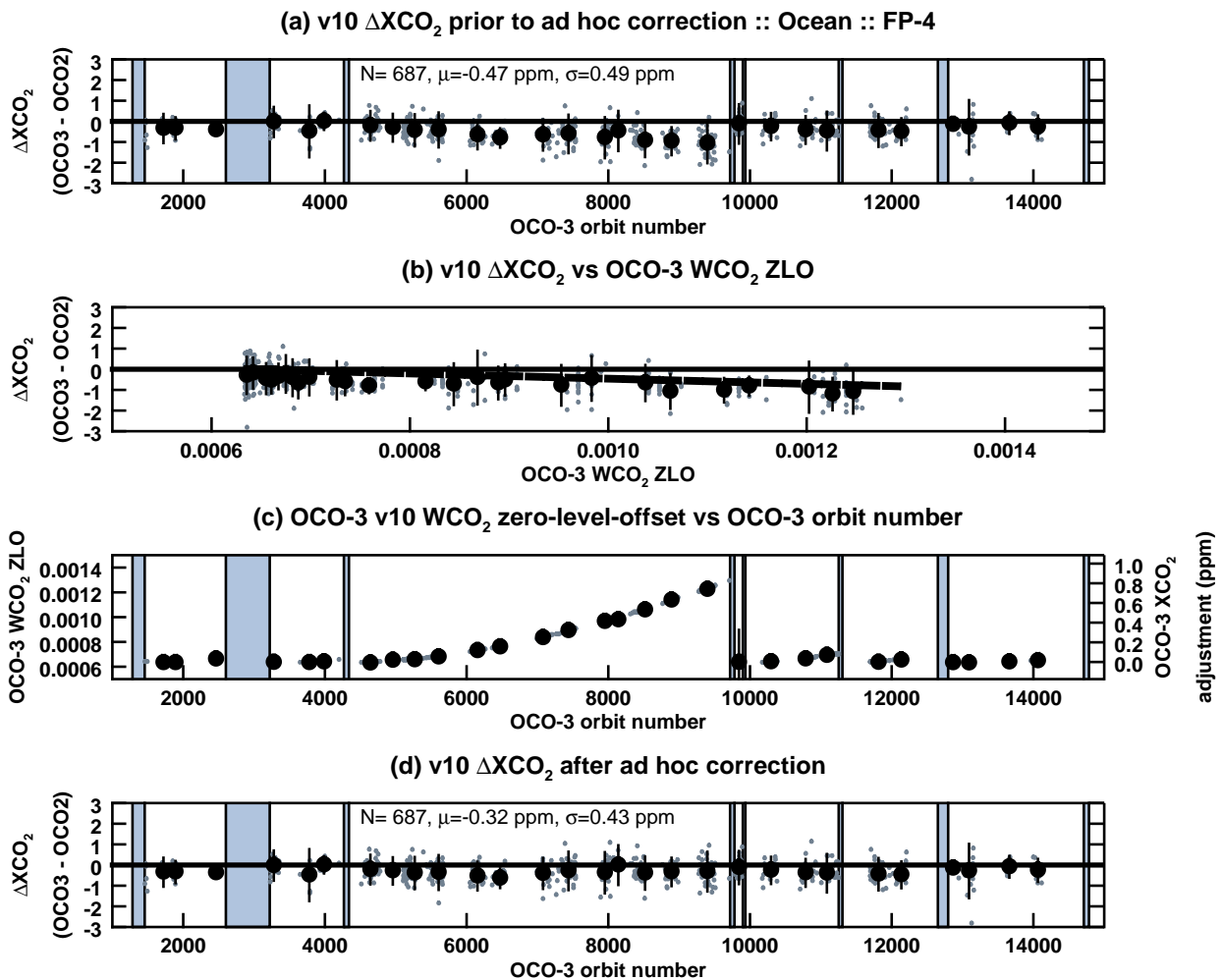
Figure B4. Same as Fig. B3, but for ocean-glint collocations.

data in the second half of 2020. After application of the ad hoc bias correction, as seen in (c) for land and (d) for ocean-glint,
840   the OCO-3 XCO_2 is in better agreement with the MMM, and is on par with expectations based on previous results from both
OCO-2 and GOSAT, e.g., Section 6.2 of this work and Section 4.4 of Taylor et al. (2022).

B4   OCO-3 v10 XCO_2 diurnal signal

The orbit of OCO-3 aboard the ISS precesses in time such that the equator crossing occurs approximately 20 minutes earlier
845   each day. This yields observations spanning all daylight hours over the course of a 63-day repeat cycle (Eldering et al., 2019).
The semi-diurnal nature of the OCO-3 data has potential to allow for interesting science investigations (e.g., Xiao et al., 2021),
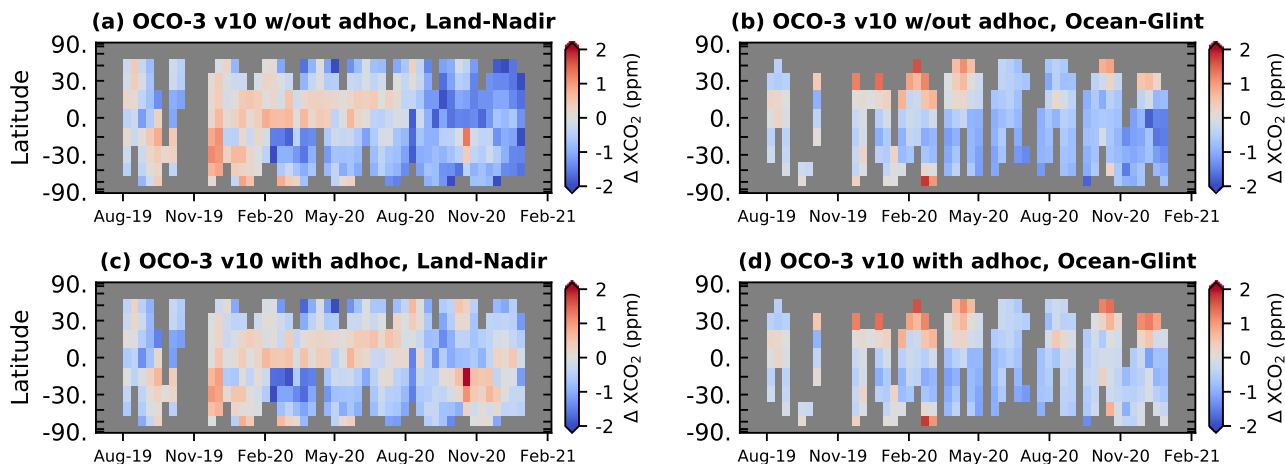
Figure B5. The XCO$_2$ signal (OCO-3 − MMM) gridded at 15° latitude by 10 days for the time period August 2019 through December 2020. Panels (a) and (c) show results before and after the ad hoc XCO$_2$ bias correction for land-nadir observations, while panels (b) and (d) are for ocean-glint observations. The ordinate axis is scaled by the cosine of the latitude to elucidate the decreasing fractional surface area of the earth with increasing latitude. Data cells with less than 10 soundings are colored gray.

that are not possible with data from polar orbiters with a fixed overpass time.

Analysis of OCO-3 XCO$_2$ from a set of more than two thousand same-day paired intersecting orbits, i.e., self-crossings, over land are shown in Fig. B6. The time separation between intersecting orbits ranges from 1.5 h up to approximately 10 h, with a spatial coincidence of 25 km radius. The difference in observed XCO$_2$ between overpasses is a combination of random uncertainty driven by instrument calibration and retrieval uncertainties, plus real changes in XCO$_2$. Over a time scale of hours, local variations in XCO$_2$ are due to a combination of (i) synoptic scale transport, i.e., CO$_2$ weather (Parazoo et al., 2008), (ii) biospheric diurnal effects, i.e., draw down by the terrestrial biosphere (Keppel-Aleks et al., 2011), or (iii) local point source emissions (e.g., Nassar et al., 2021).

Panel (a) of Fig. B6 shows the one to one correspondence in XCO$_2$ between the 2218 pairs of orbits. The mean difference is 0.04 ppm with a 1.1 ppm uncertainty. About one quarter of the samples have a difference smaller than 0.25 ppm, while one quarter have a difference larger than 1 ppm, near the upper end of expected diurnal changes in the column (Torres et al., 2019). The maximum observed difference is > 6.6 ppm! A test using a tighter spatial collocation of 10 km radius yielded indistinguishable differences, but a reduction in the number of collocations to ≈1850 (Results not shown).

Panel (b) of Fig. B6 shows the ΔXCO$_2$ versus the time difference between self-crossings. It might be expected that if the self-crossings were detecting real changes in the column CO$_2$ between overpasses driven by smooth diurnal variations due to

865 biospheric draw down, then larger ΔXCO_2 would be seen at larger Δtime. However, no significant correlation in ΔXCO_2 with Δtime is observed. The largest differences in XCO_2 are about as likely to occur between two orbits 1.5 h apart as they are to occur between two orbits 8 or 9 h apart.

An effort was made to explore geophysical and retrieval covariates in the observed XCO_2 differences. Any significant corre-
870 lations between ΔXCO_2 and L2FP retrieval variables, as is done in the bias correction procedure, could help to understand physical processes. As aerosols are a known source of error in the L2FP (Nelson and O'Dell, 2019; Bell et al., 2023), Panel (c) shows the correlation in ΔXCO_2 with the L2FP retrieved total aerosol optical depth (combined for the two overpasses). Although there is modest increase in spread for higher values of AOD, the median ΔXCO_2 values (heavy filled circles with one sigma error bars) shows no significant correlation. No other L2FP retrieval variables, e.g., albedos, geometries, were found
875 to correlate with ΔXCO_2 (results not shown).

Although additional analysis is warranted, the general conclusion is that the variability in the ΔXCO_2 from the self-crossing analysis is dominated by random uncertainties in the measurements and/or the L2FP retrieval. This conclusion stands in line with reported XCO_2 errors on the order of 0.5 ppm, and with the fidelity of the comparisons against truth proxies.
880
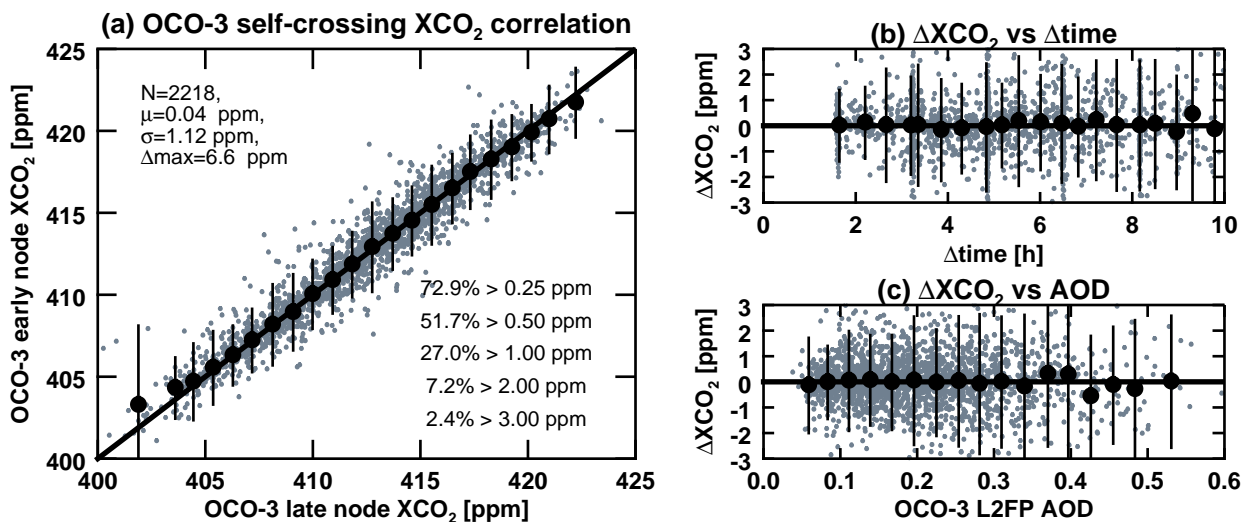
Figure B6. Analysis of OCO-3 XCO_2 from a set of paired intersecting orbits, i.e., self-crossings, over land. Panel (a) shows the one to one correspondence in XCO_2 between the early and late orbits. The number of collocations (N) and the mean (μ), standard deviation (σ) and maximum ΔXCO_2 (Δmax) are given in the legend. Also shown in the legend are the percent of the collocations having ΔXCO_2 greater than 0.25, 0.5, 1.0, 2.0, and 3.0 ppm. Panel (b) shows the ΔXCO_2 versus the time difference between self-crossings. Panel (c) shows the ΔXCO_2 versus the L2FP retrieved total aerosol optical depth (combined for the ascending and descending nodes).

Data availability

The OCO XCO$_2$ and other retrieval properties are publicly available at the NASA Goddard Earth Science Data and Information Services Center (GES-DISC). The full suite of retrieval products in the standard per-orbit format can be obtained at (OCO Science Team et al., 2020b, https://doi.org/10.5067/6SBROTA57TFH) and (OCO Science Team et al., 2021, https://doi.org/10.5067/D9S8ZOCHCADE) for OCO-2 and OCO-3, respectively. The Lite files, which include the quality flag and bias corrected estimates of XCO$_2$, can be obtained at (OCO Science Team et al., 2020a, https://doi.org/10.5067/E4E140XDMPO2) and (OCO Science Team et al., 2022, https://doi.org/10.5067/970BCC4DHH24) for OCO-2 and OCO-3, respectively. For OCO-3, researchers are urged to use the v10.4 Lite files, and avoid use of the XCO$_2$ reported in the v10 L2 Standard product which do not have the ad hoc bias correction applied.

The TCCON data for individual stations are available on the CaltechDATA site (https://data.caltech.edu/). CarbonTracker CT-NRT.v2019-2 and CT-NRT.v2021-3 results provided by NOAA ESRL, Boulder, Colorado, USA from the website at https://carbontracker.noaa.gov. The Jena-Carboscope model data are available at http://www.bgc-jena.mpg.de/CarboScope. The Copernicus Atmosphere Monitoring Service (CAMS) CAMS-INV model data were obtained from https://ads.atmosphere.copernicus.eu/cdsapp#!/dataset/cams-global-greenhouse-gas-inversion?tab=overview, while the CAMS-REAN data were obtained from https://ads.atmosphere.copernicus.eu/cdsapp#!/dataset/cams-global-ghg-reanalysis-egg4?tab=overview. The UoL model data are available at https://www.geos.ed.ac.uk/~lfeng/. The GEOS data used in this study were provided by the Global Modeling and Assimilation Office (GMAO) at NASA Goddard Space Flight Center.

Author contributions. T.E. Taylor conceptualized the study, performed the data analysis, generated the graphics, and wrote the manuscript. C.W.O helped conceptualize the study, lead the ACOS L2FP retrieval algorithm development, performed the quality filtering and bias correction, helped with data analysis, and edited an early draft of the manuscript. C. Bruegge, L. Chapsky, D. Fu, V. Haemmerle, R. Lee, Y. Marchetti, G.K. Rodrigues, R. Rosenberg, and S. Yu performed instrument calibration required for accurate retrievals of XCO$_2$. J. Zong performed the geolocation of the soundings. B. Drouin and F. Oyafuso developed and provided the spectroscopic lookup tables that are crucial for accurate retrievals of XCO$_2$. B. Fisher, M. Kiel, L. Kuai, T. Kurosu, A. Lambert, J. Laughner, L. Mandrake, G. McGarragh, A. Merrelli, R.R. Nelson, G. Osterman, P. Somkuti, G. Spiers, and P.O. Wennberg all contributed in various ways to OCO operations, the v10 ACOS L2FP algorithm testing and development, and the v10 quality filtering and bias correction procedure. A. Chang, C. Cheng, L. Dang, and C. To performed the data testing and maintained the operational pipeline required to produce the XCO$_2$ products. D. Baker provided the ten-second-average XCO$_2$ files used in the evaluation against models and provided valuable insight into the OCO v10 XCO$_2$ products during and after development. F Chevallier, L. Feng, and P.I. Palmer provided model data used in the quality filtering and bias correction and evaluation of the v10 XCO$_2$. V. Payne and A. Chatterjee are the current Project Scientists for OCO-2 and OCO-3, respectively, while M. Gunson and A. Eldering were the former Project Scientists for OCO-2 and OCO-3, respectively. J. Liu is the current OCO-2/3 Science Team Lead, while D. Crisp was the former OCO-2/3 Science Team Lead. D. Crisp also edited a mature version of the manuscript. All coauthors reviewed and provided comments on the draft manuscript prior to submission.

Competing interests. Abhishek Chatterjee and Alyn Lambert are members of the Editorial Board of Copernicus' Atmospheric Measurement

915 Techniques journal.

Acknowledgements. A portion of this research was carried out at the Jet Propulsion Laboratory, California Institute of Technology, under contract with the National Aeronautics and Space Administration (80NM0018D0004). Government sponsorship acknowledged. The CSU/CIRA contribution to this work was supported by JPL subcontracts 1439002 (OCO-2) and 1557985 (OCO-3). A. Merrelli's contributions to this work was supported by JPL subcontract 1577173. P.I. Palmer and L. Feng acknowledge support from the UK National Centre for Earth

920 Observation funded the National Environment Research Council (NE/R016518/1). We gratefully acknowledge the use of TCCON data in this work. We thank the two anonymous reviewers for their time to provide very useful comments on the manuscript. We also thank the journal editor, Joanna Joiner, for her willingness to oversee the review process.

References

Agustí-Panareda, A., Massart, S., Chevallier, F., Boussetta, S., Balsamo, G., Beljaars, A., Ciais, P., Deutscher, N. M., Engelen, R., Jones, L., Kivi, R., Paris, J.-D., Peuch, V.-H., Sherlock, V., Vermeulen, A. T., Wennberg, P. O., and Wunch, D.: Forecasting global atmospheric CO_2, Atmospheric Chemistry and Physics, 14, 11 959–11 983, https://doi.org/10.5194/acp-14-11959-2014, 2014.

Archer, D., Eby, M., Brovkin, V., Ridgwell, A., Cao, L., Mikolajewicz, U., Caldeira, K., Matsumoto, K., Munhoven, G., Montenegro, A., and Tokos, K.: Atmospheric Lifetime of Fossil Fuel Carbon Dioxide, Annual Review of Earth and Planetary Sciences, 37, 117–134, https://doi.org/10.1146/annurev.earth.031208.100206, 2009.

Baker, D. F., Bell, E., Davis, K. J., Campbell, J. F., Lin, B., and Dobler, J.: A new exponentially decaying error correlation model for assimilating OCO-2 column-average CO_2 data using a length scale computed from airborne lidar measurements, Geoscientific Model Development, 15, 649–668, https://doi.org/10.5194/gmd-15-649-2022, 2022.

Basu, S., Guerlet, S., Butz, A., Houweling, S., Hasekamp, O., Aben, I., Krummel, P., Steele, P., Langenfelds, R., Torn, M., Biraud, S., Stephens, B., Andrews, A., and Worthy, D.: Global CO_2 fluxes estimated from GOSAT retrievals of total column CO_2, Atmospheric Chemistry and Physics, 13, 8695–8717, https://doi.org/10.5194/acp-13-8695-2013, 2013.

Bell, E., O'Dell, C. W., Davis, K. J., Campbell, J., Browell, E., Scott Denning, A., Dobler, J., Erxleben, W., Fan, T.-F., Kooi, S., Lin, B., Pal, S., and Weir, B.: Evaluation of OCO-2 XCO_2 variability at local and synoptic scales using lidar and in situ observations from the ACT-America campaigns, Journal of Geophysical Research: Atmospheres, 125, https://doi.org/https://doi.org/10.1029/2019JD031400, 2020.

Bell, E., Taylor, T. E., Merrelli, A., O'Dell, C. W., Nelson, R. R., Kiel, M., Eldering, A., Rosenberg, R., and Fisher, B.: Exploring bias in OCO-3 Snapshot Area Mapping mode via geometry, surface, and aerosol effects, Atmospheric Measurement Techniques, 16, 109–133, https://doi.org/10.5194/amt-16-109-2023, 2023.

Blumenstock, T., Hase, F., Schneider, M., Garcia, O. E., and Sepulveda, E.: TCCON data from Izana (ES), Release GGG2014R1, TCCON data archive, hosted by CaltechDATA, https://doi.org/10.14291/TCCON.GGG2014.IZANA01.R1, 2017.

Bruegge, C. J., Crisp, D., Helmlinger, M. C., Kataoka, F., Kuze, A., Lee, R. A., McDuffie, J. L., Rosenberg, R. A., Schwandner, F. M., Shiomi, K., and Yu, S.: Vicarious Calibration of Orbiting Carbon Observatory-2, IEEE Transactions on Geoscience and Remote Sensing, 57, 5135–5145, https://doi.org/10.1109/TGRS.2019.2897068, 2019.

Buchwitz, M., Reuter, M., Schneising, O., Hewson, W., Detmers, R., Boesch, H., Hasekamp, O., Aben, I., Bovensmann, H., Burrows, J., Butz, A., Chevallier, F., Dils, B., Frankenberg, C., Heymann, J., Lichtenberg, G., De Mazière, M., Notholt, J., Parker, R., Warneke, T., Zehner, C., Griffith, D., Deutscher, N., Kuze, A., Suto, H., and Wunch, D.: Global satellite observations of column-averaged carbon dioxide and methane: The GHG-CCI XCO_2 and XCH_4 CRDP3 data set, Remote Sensing of Environment, 203, 276–295, https://doi.org/10.1016/j.rse.2016.12.027, earth Observation of Essential Climate Variables, 2017.

Buchwitz, M., Reuter, M., Schneising, O., Noël, S., Gier, B., Bovensmann, H., Burrows, J. P., Boesch, H., Anand, J., Parker, R. J., Somkuti, P., Detmers, R. G., Hasekamp, O. P., Aben, I., Butz, A., Kuze, A., Suto, H., Yoshida, Y., Crisp, D., and O'Dell, C.: Computation and analysis of atmospheric carbon dioxide annual mean growth rates from satellite observations during 2003–2016, Atmospheric Chemistry and Physics, 18, 17 355–17 370, https://doi.org/10.5194/acp-18-17355-2018, 2018.

Byrne, B., Liu, J., Lee, M., Yin, Y., Bowman, K. W., Miyazaki, K., Norton, A. J., Joiner, J., Pollard, D. F., Griffith, D. W. T., Velazco, V. A., Deutscher, N. M., Jones, N. B., and Paton-Walsh, C.: The Carbon Cycle of Southeast Australia During 2019–2020: Drought, Fires, and Subsequent Recovery, AGU Advances, 2, https://doi.org/10.1029/2021AV000469, 2021.

960 Byrne, B., Liu, J., Yi, Y., Chatterjee, A., Basu, S., Cheng, R., Doughty, R., Chevallier, F., Bowman, K. W., Parazoo, N. C., Crisp, D., Li, X., Xiao, J., Sitch, S., Guenet, B., Deng, F., Johnson, M. S., Philip, S., McGuire, P. C., and Miller, C. E.: Multi-year observations reveal a larger than expected autumn respiration signal across northeast Eurasia, Biogeosciences, 19, 4779–4799, https://doi.org/10.5194/bg-19-4779-2022, 2022.

Byrne, B., Baker, D. F., Basu, S., Bertolacci, M., Bowman, K. W., Carroll, D., Chatterjee, A., Chevallier, F., Ciais, P., Cressie, N., Crisp, D.,
965 Crowell, S., Deng, F., Deng, Z., Deutscher, N. M., Dubey, M. K., Feng, S., García, O. E., Griffith, D. W. T., Herkommer, B., Hu, L., Jacobson, A. R., Janardanan, R., Jeong, S., Johnson, M. S., Jones, D. B. A., Kivi, R., Liu, J., Liu, Z., Maksyutov, S., Miller, J. B., Miller, S. M., Morino, I., Notholt, J., Oda, T., O'Dell, C. W., Oh, Y.-S., Ohyama, H., Patra, P. K., Peiro, H., Petri, C., Philip, S., Pollard, D. F., Poulter, B., Remaud, M., Schuh, A., Sha, M. K., Shiomi, K., Strong, K., Sweeney, C., Té, Y., Tian, H., Velazco, V. A., Vrekoussis, M., Warneke, T., Worden, J. R., Wunch, D., Yao, Y., Yun, J., Zammit-Mangion, A., and Zeng, N.: National CO_2 budgets (2015–2020) inferred from
970 atmospheric CO_2 observations in support of the global stocktake, Earth System Science Data, 15, 963–1004, https://doi.org/10.5194/essd-15-963-2023, https://essd.copernicus.org/articles/15/963/2023/, 2023.

CAMS-INV: Copernicus Atmosphere Monitoring Service, https://atmosphere.copernicus.eu/sites/default/files/2019-08/CAMS73_2018SC1_D73.1.4.1-2018-v1_201907_v1.pdf, 2021.

CAMS-REAN: ECMWF: Copernicus Atmosphere Monitoring Service, https://doi.org/10.24380/438c-4597, 2021.

975 CarboScope: Max Planck Institute for Biogeochemistry, http://www.bgc-jena.mpg.de/CarboScope, 2021.

Chahine, M., Chen, L., Dimotakis, P., Jiang, X., Li, Q., Olsen, E., Pagano, T., Randerson, J., and Yung, Y.: Satellite remote sensing of mid-tropospheric CO_2, Geophysical Research Letters, 35, https://doi.org/10.1029/2008GL035022, 2008.

Chatterjee, A., Gierach, M. M., Sutton, A. J., Feely, R. A., Crisp, D., Eldering, A., Gunson, M. R., O'Dell, C. W., Stephens, B. B., and Schimel, D. S.: Influence of El Niño on atmospheric CO_2 over the tropical Pacific Ocean: Findings from NASA's OCO-2 mission,
980 Science, 358, https://doi.org/10.1126/science.aam5776, 2017.

Chatterjee, A., Payne, V., Eldering, A., Rosenberg, R., Kiel, M., Fisher, B., Nelson, R., Dang, L., Rodrigues, G. K., O'Dell, C., Taylor, T., and Osterman, G.: Orbiting Carbon Observatory-2 & 3 Data Quality Statement, v10, v10r, v10.4, Tech. rep., Jet Propulsion Laboratory, https://docserver.gesdisc.eosdis.nasa.gov/public/project/OCO/OCO3_L2_DQ_Statement_v10_v104.pdf, 2022.

Chevallier, F., Engelen, R. J., and Peylin, P.: The contribution of AIRS data to the estimation of CO_2 sources and sinks, Geophysical Research
985 Letters, 32, https://doi.org/10.1029/2005GL024229, 2005.

Chevallier, F., Bréon, F.-M., and Rayner, P. J.: Contribution of the Orbiting Carbon Observatory to the estimation of CO_2 sources and sinks: Theoretical study in a variational data assimilation framework, Journal of Geophysical Research: Atmospheres, 112, https://doi.org/10.1029/2006JD007375, 2007.

Chevallier, F., Ciais, P., Conway, T. J., Aalto, T., Anderson, B. E., Bousquet, P., Brunke, E. G., Ciattaglia, L., Esaki, Y., Fröhlich, M., Gomez,
990 A., Gomez-Pelaez, A. J., Haszpra, L., Krummel, P. B., Langenfelds, R. L., Leuenberger, M., Machida, T., Maignan, F., Matsueda, H., Morguí, J. A., Mukai, H., Nakazawa, T., Peylin, P., Ramonet, M., Rivier, L., Sawa, Y., Schmidt, M., Steele, L. P., Vay, S. A., Vermeulen, A. T., Wofsy, S., and Worthy, D.: CO_2 surface fluxes at grid point scale estimated from a global 21 year reanalysis of atmospheric measurements, Journal of Geophysical Research: Atmospheres, 115, https://doi.org/10.1029/2010JD013887, 2010.

Chevallier, F., Palmer, P. I., Feng, L., Boesch, H., O'Dell, C. W., and Bousquet, P.: Toward robust and consistent regional CO_2
995 flux estimates from in situ and spaceborne measurements of atmospheric CO_2, Geophysical Research Letters, 41, 1065–1070, https://doi.org/10.1002/2013GL058772, 2014.

Chevallier, F., Broquet, G., Zheng, B., Ciais, P., and Eldering, A.: Large CO_2 Emitters as Seen From Satellite: Comparison to a Gridded Global Emission Inventory, Geophysical Research Letters, 49, https://doi.org/10.1029/2021GL097540, 2022.

Ciais, P., Dolman, A. J., Bombelli, A., Duren, R., Peregon, A., Rayner, P. J., Miller, C., Gobron, N., Kinderman, G., Marland, G., Gruber, N., Chevallier, F., Andres, R. J., Balsamo, G., Bopp, L., Bréon, F.-M., Broquet, G., Dargaville, R., Battin, T. J., Borges, A., Bovensmann, H., Buchwitz, M., Butler, J., Canadell, J. G., Cook, R. B., DeFries, R., Engelen, R., Gurney, K. R., Heinze, C., Heimann, M., Held, A., Henry, M., Law, B., Luyssaert, S., Miller, J., Moriyama, T., Moulin, C., Myneni, R. B., Nussli, C., Obersteiner, M., Ojima, D., Pan, Y., Paris, J.-D., Piao, S. L., Poulter, B., Plummer, S., Quegan, S., Raymond, P., Reichstein, M., Rivier, L., Sabine, C., Schimel, D., Tarasova, O., Valentini, R., Wang, R., van der Werf, G., Wickland, D., Williams, M., and Zehner, C.: Current systematic carbon-cycle observations and the need for implementing a policy-relevant carbon observing system, Biogeosciences, 11, 3547–3602, https://doi.org/10.5194/bg-11-3547-2014, 2014.

Coddington, O. M., Richard, E. C., Harber, D., Pilewskie, P., Woods, T. N., Chance, K., Liu, X., and Sun, K.: The TSIS-1 Hybrid Solar Reference Spectrum, Geophysical Research Letters, 48, https://doi.org/10.1029/2020GL091709, 2021.

Connor, B., Bösch, H., McDuffie, J., Taylor, T., Fu, D., Frankenberg, C., O'Dell, C., Payne, V. H., Gunson, M., Pollock, R., Hobbs, J., Oyafuso, F., and Jiang, Y.: Quantification of uncertainties in OCO-2 measurements of XCO_2: simulations and linear error analysis, Atmospheric Measurement Techniques, 9, 5227–5238, https://doi.org/10.5194/amt-9-5227-2016, 2016.

Connor, B. J., Boesch, H., Toon, G., Sen, B., Miller, C., and Crisp, D.: Orbiting Carbon Observatory: Inverse method and prospective error analysis, Journal of Geophysicall Research: Atmospheres, 113, https://doi.org/10.1029/2006JD008336, 2008.

Conway, T. J., Tans, P. P., Waterman, L. S., Thoning, K. W., Kitzis, D. R., Masarie, K. A., and Zhang, N.: Evidence for interannual variability of the carbon cycle from the National Oceanic and Atmospheric Administration/Climate Monitoring and Diagnostics Laboratory Global Air Sampling Network, Journal of Geophysical Research: Atmospheres, 99, 22 831–22 855, https://doi.org/10.1029/94JD01951, 1994.

Crisp, D., Pollock, H. R., Rosenberg, R., Chapsky, L., Lee, R. A., Oyafuso, F. A., Frankenberg, C., O'Dell, C. W., Brueffe, C. J., Doran, G. B., Eldering, A., Fisher, B. M., Fu, D., Gunson, M. R., Mandrake, L., Osterman, G. B., Schwandner, F. M., Sun, K., Taylor, T. E., , Wennberg, P. O., and Wunch, D.: The on-orbit performance of the Orbiting Carbon Observatory-2 (OCO-2) instrument and its radiometrically calibrated products, Atmospheric Measurement Techniques, 10, 59–81, https://doi.org/10.5194/amt-10-59-2017, 2017.

Crisp, D., Meijer, Y., Munro, R., Bowman, K., and Chatterjee, A.: A constellation architecture for monitoring carbon dioxide and methane from space, Tech. rep., Committee on Earth Observation Satellites, https://ceos.org/document_management/Virtual_Constellations/ACC/Documents/CEOS_AC-VC_GHG_White_Paper_Publication_Draft2_20181111.pdf, 2018.

Crisp, D., O'Dell, C., Eldering, A., Fisher, B., Oyafuso, F., Payne, V., Drouin, B., Toon, G., Laughner, J., Somkuti, P., McGarragh, G., Merrelli, A., Nelson, R., Gunson, M., Frankenberg, C., Osterman, G., Boesch, H., Brown, L., Castano, R., Christi, M., Connor, B., McDuffie, J., Miller, C., Natraj, V., O'Brien, D., Polonsky, I., Smyth, M., Thompson, D., and Granat, R.: Orbiting Carbon Observatory-2 & 3 Level 2 Full Physics Retrieval Algorithm Theoretical Basis, v10, Tech. rep., Jet Propulsion Laboratory, https://docserver.gesdisc.eosdis.nasa.gov/public/project/OCO/OCO_L2_ATBD.pdf, 2020.

Crisp, D., Rosenberg, R., Chapsky, L., Rodrigues, G. R. K., Lee, R., Merrelli, A., Osterman, G., Oyafuso, F., Pollock, R., Spiers, G., Yu, S., Zong, J., and Eldering, A.: Orbiting Carbon Observatory-2 & 3 Level 1B Algorithm Theoretical Basis, v10, Tech. rep., Jet Propulsion Laboratory, https://docserver.gesdisc.eosdis.nasa.gov/public/project/OCO/OCO_L1B_ATBD.pdf, 2021.

Crisp, D., Dolman, H., Tanhua, T., McKinley, G. A., Hauck, J., Bastos, A., Sitch, S., Eggleston, S., and Aich, V.: How Well Do We Understand the Land-Ocean-Atmosphere Carbon Cycle?, Reviews of Geophysics, 60, https://doi.org/10.1029/2021RG000736, 2022.

Crowell, S., Baker, D., Schuh, A., Basu, S., Jacobson, A. R., Chevallier, F., Liu, J., Deng, F., Feng, L., McKain, K., Chatterjee, A., Miller, J. B., Stephens, B. B., Eldering, A., Crisp, D., Schimel, D., Nassar, R., O'Dell, C. W., Oda, T., Sweeney, C., Palmer, P. I., and Jones, D. B. A.: The 2015–2016 carbon cycle as seen from OCO-2 and the global in situ network, Atmospheric Chemistry and Physics, 19, 9797–9831, https://doi.org/10.5194/acp-19-9797-2019, 2019.

De Mazière, M., Sha, M. K., Desmet, F., Hermans, C., Scolas, F., Kumps, N., Metzger, J.-M., Duflot, V., and Cammas, J.-P.: TCCON data from Réunion Island (RE), Release GGG2014.R1, TCCON data archive, hosted by CaltechDATA, https://doi.org/10.14291/TCCON.GGG2014.REUNION01.R1, 2017.

Deutscher, N. M., Notholt, J., Messerschmidt, J., Weinzierl, C., Warneke, T., Petri, C., and Grupe, P.: TCCON data from Bialystok (PL), Release GGG2014.R2, TCCON data archive, hosted by CaltechDATA, https://doi.org/10.14291/TCCON.GGG2014.BIALYSTOK01.R2, 2017.

Dlugokencky, E. and Tans, P.: Trends in atmospheric carbon dioxide, NOAA/GML, https://gml.noaa.gov/ccgg/trends/, last accessed May 8, 2023, 2022.

Doughty, R., Kurosu, T. P., Parazoo, N., Köhler, P., Wang, Y., Sun, Y., and Frankenberg, C.: Global GOSAT, OCO-2, and OCO-3 solar-induced chlorophyll fluorescence datasets, Earth System Science Data, 14, 1513–1529, https://doi.org/10.5194/essd-14-1513-2022, 2022.

Drouin, B. J., Benner, D. C., Brown, L. R., Cich, M. J., Crawford, T. J., Devi, V. M., Guillaume, A., Hodges, J. T., Mlawer, E. J., Robichaud, D. J., Oyafuso, F., Payne, V. H., Sung, K., Wishnow, E. H., and Yu, S.: Multispectrum analysis of the oxygen A-band, Journal of Quantitative Spectroscopy and Radiative Transfer, 186, 118–138, https://doi.org/10.1016/j.jqsrt.2016.03.037, 2017.

Eldering, A., O'Dell, C. W., Wennberg, P. O., Crisp, D., Gunson, M. R., Viatte, C., Avis, C., Braverman, A., Castano, R., Chang, A., Chapsky, L., Cheng, C., Connor, B., Dang, L., Doran, G., Fisher, B., Frankenberg, C., Fu, D., Granat, R., Hobbs, J., Lee, R. A., Mandrake, L., McDuffie, J., Miller, C. E., Myers, V., Natraj, V., O'Brien, D., Osterman, G. B., Oyafuso, F., Payne, V. H., Pollock, H. R., Polonsky, I., Roehl, C. M., Rosenberg, R., Schwandner, F., Smyth, M., Tang, V., Taylor, T. E., To, C., Wunch, D., and Yoshimizu, J.: The Orbiting Carbon Observatory-2: first 18 months of science data products, Atmospheric Measurement Techniques, 10, 549–563, https://doi.org/10.5194/amt-10-549-2017, 2017.

Eldering, A., Taylor, T. E., O'Dell, C. W., and Pavlick, R.: The OCO-3 mission: measurement objectives and expected performance based on 1 year of simulated data, Atmospheric Measurement Techniques, 12, 2341–2370, https://doi.org/10.5194/amt-12-2341-2019, 2019.

Feist, D. G., Arnold, S. G., John, N., and Geibel, M. C.: TCCON data from Ascension Island (SH), Release GGG2014.R0, TCCON data archive, hosted by CaltechDATA, https://doi.org/10.14291/TCCON.GGG2014.ASCENSION01.R0/1149285, 2017.

Feng, L., Palmer, P. I., Bösch, H., and Dance, S.: Estimating surface CO_2 fluxes from space-borne CO_2 dry air mole fraction observations using an ensemble Kalman Filter, Atmospheric Chemistry and Physics, 9, 2619–2633, https://doi.org/10.5194/acp-9-2619-2009, 2009.

Feng, L., Palmer, P. I., Parker, R. J., Deutscher, N. M., Feist, D. G., Kivi, R., Morino, I., and Sussmann, R.: Estimates of European uptake of CO_2 inferred from GOSAT X_{CO_2} retrievals: sensitivity to measurement bias inside and outside Europe, Atmospheric Chemistry and Physics, 16, 1289–1302, https://doi.org/10.5194/acp-16-1289-2016, 2016.

Frankenberg, C., Platt, U., and Wagner, T.: Iterative maximum a posteriori (IMAP)-DOAS for retrieval of strongly absorbing trace gases: Model studies for CH_4 and CO_2 retrieval from near infrared spectra of SCIAMACHY onboard ENVISAT, Atmospheric Chemistry and Physics, 5, 9–22, https://doi.org/10.5194/acp-5-9-2005, 2005.

Frankenberg, C., O'Dell, C., Guanter, L., and McDuffie, J.: Remote sensing of near-infrared chlorophyll fluorescence from space in scattering atmospheres: implications for its retrieval and interferences with atmospheric CO_2 retrievals, Atmospheric Measurement Techniques, 5, 2081–2094, https://doi.org/10.5194/amt-5-2081-2012, 2012.

Friedlingstein, P., O'Sullivan, M., Jones, M. W., Andrew, R. M., Gregor, L., Hauck, J., Le Quéré, C., Luijkx, I. T., Olsen, A., Peters, G. P., Peters, W., Pongratz, J., Schwingshackl, C., Sitch, S., Canadell, J. G., Ciais, P., Jackson, R. B., Alin, S. R., Alkama, R., Arneth, A., Arora, V. K., Bates, N. R., Becker, M., Bellouin, N., Bittig, H. C., Bopp, L., Chevallier, F., Chini, L. P., Cronin, M., Evans, W., Falk, S., Feely, R. A., Gasser, T., Gehlen, M., Gkritzalis, T., Gloege, L., Grassi, G., Gruber, N., Gürses, O., Harris, I., Hefner, M., Houghton, R. A., Hurtt, G. C., Iida, Y., Ilyina, T., Jain, A. K., Jersild, A., Kadono, K., Kato, E., Kennedy, D., Klein Goldewijk, K., Knauer, J., Korsbakken, J. I., Landschützer, P., Lefèvre, N., Lindsay, K., Liu, J., Liu, Z., Marland, G., Mayot, N., McGrath, M. J., Metzl, N., Monacci, N. M., Munro, D. R., Nakaoka, S.-I., Niwa, Y., O'Brien, K., Ono, T., Palmer, P. I., Pan, N., Pierrot, D., Pocock, K., Poulter, B., Resplandy, L., Robertson, E., Rödenbeck, C., Rodriguez, C., Rosan, T. M., Schwinger, J., Séférian, R., Shutler, J. D., Skjelvan, I., Steinhoff, T., Sun, Q., Sutton, A. J., Sweeney, C., Takao, S., Tanhua, T., Tans, P. P., Tian, X., Tian, H., Tilbrook, B., Tsujino, H., Tubiello, F., van der Werf, G. R., Walker, A. P., Wanninkhof, R., Whitehead, C., Willstrand Wranne, A., Wright, R., Yuan, W., Yue, C., Yue, X., Zaehle, S., Zeng, J., and Zheng, B.: Global Carbon Budget 2022, Earth System Science Data, 14, 4811–4900, https://doi.org/10.5194/essd-14-4811-2022, 2022.

Gelaro, R., McCarty, W., Suárez, M. J., Todling, R., Molod, A., Takacs, L., Randles, C. A., Darmenov, A., Bosilovich, M. G., Reichle, R., Wargan, K., Coy, L., Cullather, R., Draper, C., Akella, S., Buchard, V., Conaty, A., da Silva, A. M., Gu, W., Kim, G.-K., Koster, R., Lucchesi, R., Merkova, D., Nielsen, J. E., Partyka, G., Pawson, S., Putman, W., Rienecker, M., Schubert, S. D., Sienkiewicz, M., and Zhao, B.: The Modern-Era Retrospective Analysis for Research and Applications, Version 2 (MERRA-2), Journal of Climate, 30, 5419 – 5454, https://doi.org/10.1175/JCLI-D-16-0758.1, 2017.

Goo, T.-Y., Oh, Y.-S., and Velazco, V. A.: TCCON data from Anmeyondo (KR), Release GGG2014.R0, TCCON data archive, hosted by CaltechDATA, https://doi.org/10.14291/TCCON.GGG2014.ANMEYONDO01.R0/1149284, 2017.

Griffith, D. W., Deutscher, N. M., Velazco, V. A., Wennberg, P. O., Yavin, Y., Aleks, G. K., Washenfelder, R. a., Toon, G. C., Blavier, J.-F., Murphy, C., Jones, N., Kettlewell, G., Connor, B. J., Macatangay, R., Roehl, C., Ryczek, M., Glowacki, J., Culgan, T., and Bryant, G.: TCCON data from Darwin (AU), Release GGG2014R0, TCCON data archive, hosted by CaltechDATA, https://doi.org/10.14291/tccon.ggg2014.darwin01.R0/1149290, 2014a.

Griffith, D. W., Velazco, V. A., Deutscher, N. M., Murphy, C., Jones, N., Wilson, S., Macatangay, R., Kettlewell, G., Buchholz, R. R., and Riggenbach, M.: TCCON data from Wollongong (AU), Release GGG2014R0, TCCON data archive, hosted by CaltechDATA, https://doi.org/10.14291/tccon.ggg2014.wollongong01.R0/1149291, 2014b.

Gurney, K. R., Law, R. M., Denning, S., Rayner, P. J., Baker, D., Bousquet, P., Bruhwiler, L., Chen, Y.-H., Ciais, P., Fan, S., Fung, I. Y., Gloor, M., Heimann, M., Higuchi, K., John, J., Maki, T., Maksyutov, S., Masarie, K., Peylin, P., Prather, M., Pak, B. C., Randerson, J., Sarmiento, J., Taguchi, S., Takahashi, T., and Yuen, C.-W.: Towards robust regional estimates of CO_2 sources and sinks using atmospheric transport models, Nature, 415, 626–630, https://doi.org/10.1038/415626a, 2002.

Hase, F., Blumenstock, T., Dohe, S., Gross, J., and Kiel, M.: TCCON data from Karlsruhe (DE), Release GGG2014R1, TCCON data archive, hosted by CaltechDATA, https://doi.org/10.14291/tccon.ggg2014.karlsruhe01.R1/1182416, 2015.

Hobbs, J., Braverman, A., Cressie, N., Granat, R., and Gunson, M.: Simulation-Based Uncertainty Quantification for Estimating Atmospheric CO_2 from Satellite Data, SIAM/ASA Journal on Uncertainty Quantification, 5, 956–985, https://doi.org/10.1137/16M1060765, 2017.

Iraci, L. T., Podolske, J., Hillyard, P. W., Roehl, C., Wennberg, P. O., Blavier, J.-F., Allen, N., Wunch, D., Osterman, G. B., and Albertson, R.: TCCON data from Edwards (US), Release GGG2014R1, TCCON data archive, hosted by CaltechDATA, https://doi.org/10.14291/tccon.ggg2014.edwards01.R1/1255068, 2016.

Jacobs, N., Simpson, W. R., Wunch, D., O'Dell, C. W., Osterman, G. B., Hase, F., Blumenstock, T., Tu, Q., Frey, M., Dubey, M. K., Parker, H. A., Kivi, R., and Heikkinen, P.: Quality controls, bias, and seasonality of CO_2 columns in the boreal forest with Orbiting Carbon

Observatory-2, Total Carbon Column Observing Network, and EM27/SUN measurements, Atmospheric Measurement Techniques, 13, 5033–5063, https://doi.org/10.5194/amt-13-5033-2020, https://amt.copernicus.org/articles/13/5033/2020/, 2020.

Jacobson, A. R., Schuldt, K. N., Miller, J. B., Tans, P., Andrews, A., Mund, J., Aalto, T., Abshire, J. B., Aikin, K., Aoki, S., Apadula, F., Baier, B., Bakwin, P., Bartyzel, J., Bentz, G., Bergamaschi, P., Beyersdorf, A., Biermann, T., Biraud, S. C., Bowling, D., Brailsford, G., Van Den Bulk, P., Chen, G., Chen, H., Chmura, L., Clark, S., Coletta, J. D., Colomb, A., Commane, R., Conil, S., Cox, A., Cristofanelli, P., Cuevas, E., Curcoll, R., Daube, B., Davis, K., Delmotte, M., DiGangi, J. P., Van Dinther, D., Dlugokencky, E., Elkins, J. W., Emmenegger, L., Fischer, M. L., Forster, G., Frumau, A., Galkowski, M., Gatti, L. V., Gheusi, F., Gloor, E., Gomez-Trueba, V., Goto, D., Griffis, T., Hammer, S., Hanson, C., Haszpra, L., Hatakka, J., Heliasz, M., Hensen, A., Hermanssen, O., Hintsa, E., Holst, J., Jaffe, D., Joubert, W., Karion, A., Kawa, S. R., Kazan, V., Keeling, R., Keronen, P., Kolari, P., Kominkova, K., Kort, E., Krummel, P., Kubistin, D., Labuschagne, C., Langenfelds, R., Laurent, O., Laurila, T., Lauvaux, T., Law, B., Lee, J., Lehner, I., Leuenberger, M., Levin, I., Levula, J., Lin, J., Lindauer, M., Loh, Z., Lopez, M., Machida, T., Mammarella, I., Manca, G., Manning, A., Manning, A., Marek, M. V., Martin, M. Y., Matsueda, H., De Maziäre, M., McKain, K., Meijer, H., Meinhardt, F., Merchant, L., N. Mihalopoulos, Miles, N., Miller, C. E., Mitchell, L., Malder, M., Montzka, S., Moore, F., Morgan, E., Josep-Anton Morgui, Morimoto, S., Maeller-Williams, J., Munger, B., Myhre, C. L., Jaroslaw Necki, Newman, S., Nichol, S., Niwa, Y., O'Doherty, S., Paplawsky, B., Peischl, J., Peltola, O., Piacentino, S., Pichon, J. M., Piper, S., Plass-Duelmer, C., Plass-Duelmer, C., Ramonet, M., Ramos, R., Reyes-Sanchez, E., Richardson, S., Riris, H., Rivas, P. P., Ryerson, T., Saito, K., Sargent, M., Di Sarra, A. G., Sawa, Y., Say, D., Scheeren, B., Schmidt, M., Schumacher, M., Sha, M. K., Shepson, P., Shook, M., Sloop, C. D., Smith, P., Steinbacher, M., Stephens, B., Sweeney, C., Thoning, K., Torn, M., Tarseth, K., Trisolino, P., Turnbull, J., Vermeulen, A., Viner, B., Vitkova, G., Walker, S., De Wekker, S., Wofsy, S., Worthy, D., Dickon Young, and Miroslaw Zimnoch: CarbonTracker Near-Real Time, CT-NRT.v2021-3, https://doi.org/10.25925/ED7S-M661, 2021.

Janssens-Maenhout, G., Pinty, B., Dowell, M., Zunker, H., Andersson, E., Balsamo, G., Bézy, J.-L., Brunhes, T., Bösch, H., Bojkov, B., Brunner, D., Buchwitz, M., Crisp, D., Ciais, P., Counet, P., Dee, D., van der Gon, H. D., Dolman, H., Drinkwater, M. R., Dubovik, O., Engelen, R., Fehr, T., Fernandez, V., Heimann, M., Holmlund, K., Houweling, S., Husband, R., Juvyns, O., Kentarchos, A., Landgraf, J., Lang, R., Löscher, A., Marshall, J., Meijer, Y., Nakajima, M., Palmer, P. I., Peylin, P., Rayner, P., Scholze, M., Sierk, B., Tamminen, J., and Veefkind, P.: Toward an operational anthropogenic CO_2 emissions monitoring and verification support capacity, Bulletin of the American Meteorological Society, 101, E1439 – E1451, https://doi.org/10.1175/BAMS-D-19-0017.1, 2020.

Jiang, F., Ju, W., He, W., Wu, M., Wang, H., Wang, J., Jia, M., Feng, S., Zhang, L., and Chen, J. M.: A 10-year global monthly averaged terrestrial net ecosystem exchange dataset inferred from the ACOS GOSAT v9 XCO_2 retrievals (GCAS2021), Earth System Science Data, 14, 3013–3037, https://doi.org/10.5194/essd-14-3013-2022, 2022.

Keller, G. R., Rosenberg, R. A., Spiers, G. D., Yu, S., Merrelli, A., O'Dell, C. W., Lee, R. A., Crisp, D., Eldering, A., and Chatterjee, A.: Inflight radiometric calibration and performance of the Orbiting Carbon Observatory 3 for version 10 products, IEEE Transactions on Geoscience and Remote Sensing, 60, 1–18, https://doi.org/10.1109/TGRS.2022.3216825, 2022.

Keppel-Aleks, G., Wennberg, P. O., and Schneider, T.: Sources of variations in total column carbon dioxide, Atmospheric Chemistry and Physics, 11, 3581–3593, https://doi.org/10.5194/acp-11-3581-2011, 2011.

Kiel, M., O'Dell, C. W., Fisher, B., Eldering, A., Nassar, R., MacDonald, C. G., and Wennberg, P. O.: How bias correction goes wrong: measurement of XCO_2 affected by erroneous surface pressure estimates, Atmospheric Measurement Techniques, 12, 2241–2259, https://doi.org/10.5194/amt-12-2241-2019, 2019.

Kiel, M., Eldering, A., Roten, D. D., Lin, J. C., Feng, S., Lei, R., Lauvaux, T., Oda, T., Roehl, C. M., Blavier, J.-F., and Iraci, L. T.: Urban-focused satellite CO_2 observations from the Orbiting Carbon Observatory-3: A first look at the Los Angeles megacity, Remote Sensing of Environment, 258, 112 314, https://doi.org/10.1016/j.rse.2021.112314, 2021.

Kivi, R., Heikkinen, P., and Kyrö, E.: TCCON data from Sodankylä, Finland, Release GGG2014R1, TCCON data archive, hosted by CaltechDATA, https://doi.org/10.14291/tccon.ggg2014.sodankyla01.R1, 2020.

Kong, Y., Zheng, B., Zhang, Q., and He, K.: Global and regional carbon budget for 2015–2020 inferred from OCO-2 based on an ensemble Kalman filter coupled with GEOS-Chem, Atmospheric Chemistry and Physics, 22, 10 769–10 788, https://doi.org/10.5194/acp-22-10769-2022, 2022.

Kulawik, S., Wunch, D., O'Dell, C., Frankenberg, C., Reuter, M., Oda, T., Chevallier, F., Sherlock, V., Buchwitz, M., Osterman, G., Miller, C. E., Wennberg, P. O., Griffith, D., Morino, I., Dubey, M. K., Deutscher, N. M., Notholt, J., Hase, F., Warneke, T., Sussmann, R., Robinson, J., Strong, K., Schneider, M., De Mazière, M., Shiomi, K., Feist, D. G., Iraci, L. T., and Wolf, J.: Consistent evaluation of ACOS-GOSAT, BESD-SCIAMACHY, CarbonTracker, and MACC through comparisons to TCCON, Atmospheric Measurement Techniques, 9, 683–709, https://doi.org/10.5194/amt-9-683-2016, 2016.

Kulawik, S. S., O'Dell, C., Nelson, R. R., and Taylor, T. E.: Validation of OCO-2 error analysis using simulated retrievals, Atmospheric Measurement Techniques, 12, 5317–5334, https://doi.org/10.5194/amt-12-5317-2019, 2019.

Kuze, A., Suto, H., Nakajima, M., and Hamazaki, T.: Thermal and near infrared sensor for carbon observation Fourier-transform spectrometer on the Greenhouse Gases Observing Satellite for greenhouse gases monitoring, Appl. Opt., 48, 6716–6733, https://doi.org/10.1364/AO.48.006716, 2009.

Lan, X., Dlugokencky, E., Mund, J., Crotwell, A., Crotwell, M., Moglia, E., Madronich, M., Neff, D., and Thoning, K.: Atmospheric Carbon Dioxide Dry Air Mole Fractions from the NOAA GML Carbon Cycle Cooperative Global Air Sampling Network, 1968-2021, Version: 2022-11-21, https://doi.org/10.15138/wkgj-f215, 2022.

Laughner, J. L., Roche, S., Kiel, M., Toon, G. C., Wunch, D., Baier, B. C., Biraud, S., Chen, H., Kivi, R., Laemmel, T., McKain, K., Quéhé, P.-Y., Rousogenous, C., Stephens, B. B., Walker, K., and Wennberg, P. O.: A new algorithm to generate a priori trace gas profiles for the GGG2020 retrieval algorithm, Atmospheric Measurement Techniques, 16, 1121–1146, https://doi.org/10.5194/amt-16-1121-2023, https://amt.copernicus.org/articles/16/1121/2023/, 2023.

L'Ecuyer, T. and Jiang, J.: Touring the atmosphere aboard the A-Train, Physics Today, 63, 36–41, https://doi.org/10.1063/1.3463626, 2010.

Lee, R. A., O'Dell, C. W., Wunch, D., Roehl, C. M., Osterman, G. B., Blavier, J.-F., Rosenberg, R., Chapsky, L., Frankenberg, C., Hunyadi-Lay, S. L., Fisher, B. M., Rider, D. M., Crisp, D., and Pollock, R.: Preflight spectral calibration of the Orbiting Carbon Observatory-2, TGRS, 55, 2499–2508, https://doi.org/10.1109/TGRS.2016.2645614, 2017.

Lei, R., Feng, S., Danjou, A., Broquet, G., Wu, D., Lin, J. C., O'Dell, C. W., and Lauvaux, T.: Fossil fuel CO_2 emissions over metropolitan areas from space: A multi-model analysis of OCO-2 data over Lahore, Pakistan, Remote Sensing of Environment, 264, 112 625, https://doi.org/10.1016/j.rse.2021.112625, 2021.

Liu, J., Bowman, K. W., Schimel, D. S., Parazoo, N. C., Jiang, Z., Lee, M., Bloom, A. A., Wunch, D., Frankenberg, C., Sun, Y., O'Dell, C. W., Gurney, K. R., Menemenlis, D., Gierach, M., Crisp, D., and Eldering, A.: Contrasting carbon cycle responses of the tropical continents to the 2015–2016 El Niño, Science, 358, https://doi.org/10.1126/science.aam5690, 2017.

Marchetti, Y., Rosenberg, R., and Crisp, D.: Classification of Anomalous Pixels in the Focal Plane Arrays of Orbiting Carbon Observatory-2 and -3 via Machine Learning, Remote Sensing, 11, https://doi.org/10.3390/rs11242901, 2019.

Massie, S. T., Cronk, H., Merrelli, A., O'Dell, C., Schmidt, K. S., Chen, H., and Baker, D.: Analysis of 3D cloud effects in OCO-2 X_{CO_2} retrievals, Atmospheric Measurement Techniques, 14, 1475–1499, https://doi.org/10.5194/amt-14-1475-2021, 2021.

Massie, S. T., Cronk, H., Merrelli, A., Schmidt, S., and Mauceri, S.: Insights into 3D cloud radiative transfer effects for the Orbiting Carbon Observatory, Atmospheric Measurement Techniques, 16, 2145–2166, https://doi.org/10.5194/amt-16-2145-2023, https://amt.copernicus.org/articles/16/2145/2023/, 2023.

Mauceri, S., Massie, S., and Schmidt, S.: Correcting 3D cloud effects in X_{CO_2} retrievals from the Orbiting Carbon Observatory-2 (OCO-2), Atmospheric Measurement Techniques, 16, 1461–1476, https://doi.org/10.5194/amt-16-1461-2023, https://amt.copernicus.org/articles/16/1461/2023/, 2023.

Miller, C. E., Crisp, D., DeCola, P. L., Olsen, S. C., Randerson, J. T., Michalak, A. M., Alkhaled, A., Rayner, P., Jacob, D. J., Suntharalingam, P., Jones, D. B. A., Denning, A. S., Nicholls, M. E., Doney, S. C., Pawson, S., Boesch, H., Connor, B. J., Fung, I. Y., O'Brien, D., Salawitch, R. J., Sander, S. P., Sen, B., Tans, P., Toon, G. C., Wennberg, P. O., Wofsy, S. C., Yung, Y. L., and Law, R. M.: Precision requirements for space-based X_{CO_2} data, Journal of Geophysical Research: Atmospheres, 112, https://doi.org/10.1029/2006JD007659, 2007.

Morino, I., Matsuzaki, T., and Horikawa, M.: TCCON data from Tsukuba (JP), 125HR, Release GGG2014R2, TCCON data archive, hosted by CaltechDATA, https://doi.org/10.14291/TCCON.GGG2014.TSUKUBA02.R2, 2018a.

Morino, I., Velazco, V. A., Hori, A., Uchino, O., and Griffith, D. W. T.: TCCON data from Burgos, Ilocos Norte (PH), Release GGG2014.R0, TCCON data archive, hosted by CaltechDATA, https://doi.org/10.14291/TCCON.GGG2014.BURGOS01.R0, 2018b.

Morino, I., Yokozeki, N., Matzuzaki, A., and Shishime, A.: TCCON data from Rikubetsu, Hokkaido, Japan, Release GGG2014R2, TCCON data archive, hosted by CaltechDATA, https://doi.org/10.14291/TCCON.GGG2014.RIKUBETSU01.R2, 2018c.

Müller, A., Tanimoto, H., Sugita, T., Machida, T., Nakaoka, S., Patra, P. K., Laughner, J., and Crisp, D.: New approach to evaluate satellite-derived XCO2 over oceans by integrating ship and aircraft observations, Atmospheric Chemistry and Physics, 21, 8255–8271, https://doi.org/10.5194/acp-21-8255-2021, https://acp.copernicus.org/articles/21/8255/2021/, 2021.

Nassar, R., Hill, T. G., McLinden, C. A., Wunch, D., Jones, D. B. A., and Crisp, D.: Quantifying CO_2 Emissions From Individual Power Plants From Space, Geophysical Research Letters, 44, 10,045–10,053, https://doi.org/10.1002/2017GL074702, 2017.

Nassar, R., Mastrogiacomo, J.-P., Bateman-Hemphill, W., McCracken, C., MacDonald, C. G., Hill, T., O'Dell, C. W., Kiel, M., and Crisp, D.: Advances in quantifying power plant CO_2 emissions with OCO-2, Remote Sensing of Environment, 264, 112 579, https://doi.org/10.1016/j.rse.2021.112579, 2021.

Nassar, R., Moeini, O., Mastrogiacomo, J.-P., O'Dell, C. W., Nelson, R. R., Kiel, M., Chatterjee, A., Eldering, A., and Crisp, D.: Tracking CO_2 emission reductions from space: A case study at Europe's largest fossil fuel power plant, Frontiers in Remote Sensing, 3, https://doi.org/10.3389/frsen.2022.1028240, 2022.

Nelson, R. R. and O'Dell, C. W.: The impact of improved aerosol priors on near-infrared measurements of carbon dioxide, Atmospheric Measurement Techniques, 12, 1495–1512, https://doi.org/10.5194/amt-12-1495-2019, 2019.

Notholt, J., Petri, C., Warneke, T., Deutscher, N. M., Palm, M., Buschmann, M., Weinzierl, C., Macatangay, R. C., and Grupe, P.: TCCON data from Bremen (DE), Release GGG2014.R1, TCCON data archive, hosted by CaltechDATA, https://doi.org/10.14291/TCCON.GGG2014.BREMEN01.R1, 2019.

OCO Science Team, Gunson, M., and Eldering, A.: OCO-2 Level 2 bias-corrected X_{CO_2} and other select fields from the full-physics retrieval aggregated as daily files, Retrospective processing V10r, Goddard Earth Sciences Data and Information Services Center (GES DISC), Greenbelt, MD, USA, https://doi.org/10.5067/E4E140XDMPO2, last accessed May 8, 2023, 2020a.

1220 OCO Science Team, Gunson, M., and Eldering, A.: OCO-2 Level 2 geolocated XCO$_2$ retrievals results, physical model, Retrospective Processing V10r, Goddard Earth Sciences Data and Information Services Center (GES DISC), Greenbelt, MD, USA, https://doi.org/10.5067/6SBROTA57TFH, last accessed May 8, 2023, 2020b.

OCO Science Team, Gunson, M., and Eldering, A.: OCO-3 Level 2 geolocated XCO$_2$ retrievals results, physical model, Forward Processing V10, Goddard Earth Sciences Data and Information Services Center (GES DISC), Greenbelt, MD, USA, https://doi.org/10.5067/D9S8ZOCHCADE, last accessed May 8, 2023, 2021.

OCO Science Team, Chatterjee, A., and Payne, V.: OCO-3 Level 2 bias-corrected XCO$_2$ and other select fields from the full-physics retrieval aggregated as daily files, Retrospective processing v10.4r, Goddard Earth Sciences Data and Information Services Center (GES DISC), Greenbelt, MD, USA, https://doi.org/10.5067/970BCC4DHH24, last accessed May 8, 2023, 2022.

O'Dell, C. W., Connor, B., Bösch, H., O'Brien, D., Frankenberg, C., Castano, R., Christi, M., Crisp, D., Eldering, A., Fisher, B., Gunson, M., McDuffie, J., Miller, C. E., Natraj, V., Oyafuso, F., Polonsky, I., Smyth, M., Taylor, T., Toon, G. C., Wennberg, P. O., and Wunch, D.: The ACOS CO$_2$ retrieval algorithm–Part 1: Description and validation against synthetic observations, Atmospheric Measurement Techniques, 5, 99–121, https://doi.org/10.5194/amt-5-99-2012, 2012.

O'Dell, C. W., Eldering, A., Wennberg, P. O., Crisp, D., Gunson, M. R., Fisher, B., Frankenberg, C., Kiel, M., Lindqvist, H., Mandrake, L., Merrelli, A., Natraj, V., Nelson, R. R., Osterman, G. B., Payne, V. H., Taylor, T. E., Wunch, D., Drouin, B. J., Oyafuso, F., Chang, A., McDuffie, J., Smyth, M., Baker, D. F., Basu, S., Chevallier, F., Crowell, S. M. R., Feng, L., Palmer, P. I., Dubey, M., García, O. E., Griffith, D. W. T., Hase, F., Iraci, L. T., Kivi, R., Morino, I., Notholt, J., Ohyama, H., Petri, C., Roehl, C. M., Sha, M. K., Strong, K., Sussmann, R., Te, Y., Uchino, O., and Velazco, V. A.: Improved retrievals of carbon dioxide from Orbiting Carbon Observatory-2 with the version 8 ACOS algorithm, Atmospheric Measurement Techniques, 11, 6539–6576, https://doi.org/10.5194/amt-11-6539-2018, 2018.

Osterman, G., O'Dell, C., Eldering, A., Fisher, B., Crisp, D., Cheng, C., Frankenberg, C., Lambert, A., Gunson, M., Mandrake, L., and Wunch, D.: Orbiting Carbon Observatory-2 & 3 Data Product User's Guide, v10, Tech. rep., Jet Propulsion Laboratory, https://docserver.gesdisc.eosdis.nasa.gov/public/project/OCO/OCO2_OCO3_B10_DUG.pdf, 2020.

Oyafuso, F., Payne, V. H., Drouin, B. J., Devi, V. M., Benner, D. C., Sung, K., Yu, S., Gordon, I. E., Kochanov, R., Tan, Y., Crisp, D., Mlawer, E. J., and Guillaume, A.: High accuracy absorption coefficients for the Orbiting Carbon Observatory-2 (OCO-2) mission: Validation of updated carbon dioxide cross-sections using atmospheric spectra, Journal of Quantitative Spectroscopy and Radiative Transfer, 203, 213–223, https://doi.org/10.1016/j.jqsrt.2017.06.012, 2017.

Palmer, P. I., Feng, L., Baker, D., Chevallier, F., Bösch, H., and Somkuti, P.: Net carbon emissions from African biosphere dominate pan-tropical atmospheric CO$_2$ signal, Nature Communications, 10, 3344, https://doi.org/10.1038/s41467-019-11097-w, 2019.

Palmer, P. I., Woodwark, A. J. P., Finch, D., Taylor, T. E., Butz, A., Tamminen, J., Bösch, H., Eldering, A., and Vincent-Bonnieu, S.: Role of space station instruments for improving tropical carbon flux estimates using atmospheric data, npj Microgravity, 8, 51, https://doi.org/10.1038/s41526-022-00231-6, 2022.

Parazoo, N. C., Denning, A. S., Kawa, S. R., Corbin, K. D., Lokupitiya, R. S., and Baker, I. T.: Mechanisms for synoptic variations of atmospheric CO$_2$ in North America, South America and Europe, Atmospheric Chemistry and Physics, 8, 7239–7254, https://doi.org/10.5194/acp-8-7239-2008, 2008.

Payne, V., Chatterjee, A., Rosenberg, R., Kiel, M., Fisher, B., Dang, L., O'Dell, C., Taylor, T., and Osterman, G.: Orbiting Carbon Observatory-2 & 3 Data Product User's Guide, OCO-2 v11 and OCO-3 v10.4, Tech. rep., Jet Propulsion Laboratory, https://docserver.gesdisc.eosdis.nasa.gov/public/project/OCO/OCO2_V11_OCO3_V10_DUG.pdf, 2022.

Payne, V. H., Drouin, B. J., Oyafuso, F., Kuai, L., Fisher, B. M., Sung, K., Nemchick, D., Crawford, T. J., Smyth, M., Crisp, D., Adkins, E., Hodges, J. T., Long, D. A., Mlawer, E. J., Merrelli, A., Lunny, E., and O'Dell, C. W.: Absorption coefficient (ABSCO) tables for the Orbiting Carbon Observatories: Version 5.1, Journal of Quantitative Spectroscopy and Radiative Transfer, 255, 107 217, https://doi.org/10.1016/j.jqsrt.2020.107217, 2020.

Peiro, H., Crowell, S., Schuh, A., Baker, D. F., O'Dell, C., Jacobson, A. R., Chevallier, F., Liu, J., Eldering, A., Crisp, D., Deng, F., Weir, B., Basu, S., Johnson, M. S., Philip, S., and Baker, I.: Four years of global carbon cycle observed from the Orbiting Carbon Observatory 2 (OCO-2) version 9 and in situ data and comparison to OCO-2 version 7, Atmospheric Chemistry and Physics, 22, 1097–1130, https://doi.org/10.5194/acp-22-1097-2022, 2022.

Peters, W., Jacobson, A. R., Sweeney, C., Andrews, A. E., Conway, T. J., Masarie, K., Miller, J. B., Bruhwiler, L. M. P., Pétron, G., Hirsch, A. I., Worthy, D. E. J., van der Werf, G. R., Randerson, J. T., Wennberg, P. O., Krol, M. C., and Tans, P. P.: An atmospheric perspective on North American carbon dioxide exchange: CarbonTracker, Proceedings of the National Academy of Sciences, 104, 18 925–18 930, https://doi.org/10.1073/pnas.0708986104, 2007.

Petri, C., Vrekoussis, M., Rousogenous, C., Warneke, T., Sciare, J., and Notholt, J.: TCCON data from Nicosia (CY), Release GGG2014R0, TCCON data archive, hosted by CaltechDATA, https://doi.org/10.14291/tccon.ggg2014.nicosia01.R0, 2020.

Philip, S., Johnson, M. S., Baker, D. F., Basu, S., Tiwari, Y. K., Indira, N. K., Ramonet, M., and Poulter, B.: OCO-2 Satellite-Imposed Constraints on Terrestrial Biospheric CO_2 Fluxes Over South Asia, Journal of Geophysical Research: Atmospheres, 127, https://doi.org/10.1029/2021JD035035, 2022.

Pollard, D. F., Robinson, J., and Shiona, H.: TCCON data from Lauder (NZ), Release GGG2014.R0, TCCON data archive, hosted by CaltechDATA, https://doi.org/10.14291/TCCON.GGG2014.LAUDER03.R0, 2017.

Rastogi, B., Miller, J. B., Trudeau, M., Andrews, A. E., Hu, L., Mountain, M., Nehrkorn, T., Baier, B., McKain, K., Mund, J., Guan, K., and Alden, C. B.: Evaluating consistency between total column CO_2 retrievals from OCO-2 and the in situ network over North America: implications for carbon flux estimation, Atmospheric Chemistry and Physics, 21, 14 385–14 401, https://doi.org/10.5194/acp-21-14385-2021, 2021.

Richard, E., Harber, D., Coddington, O., Drake, G., Rutkowski, J., Triplett, M., Pilewskie, P., and Woods, T.: SI-traceable Spectral Irradiance Radiometric Characterization and Absolute Calibration of the TSIS-1 Spectral Irradiance Monitor (SIM), Remote Sensing, 12, https://doi.org/10.3390/rs12111818, 2020.

Rienecker, M. M., Suarez, M. J., Todling, R., Bacmeister, J., Takacs, L., Liu, H.-C., Gu, W., Sienkiewicz, M., Koster, R. D., Gelaro, R., Stajner, I., and Nielsen, J. E.: The GEOS-5 Data Assimilation System-Documentation of Versions 5.0.1, 5.1.0, and 5.2.0, Tech. rep., NASA Goddard Space Flight Center, Greenbelt, MD, https://ntrs.nasa.gov/archive/nasa/ntrs.nasa.gov/20120011955.pdf, 2008.

Rienecker, M. M., Suarez, M. J., Gelaro, R., Todling, R., Bacmeister, J., Liu, E., Bosilovich, M. G., Schubert, S. D., Takacs, L., Kim, G.-K., Bloom, S., Chen, J., Collins, D., Conaty, A., da Silva, A., Gu, W., Joiner, J., Koster, R. D., Lucchesi, R., Molod, A., Owens, T., Pawson, S., Pegion, P., Redder, C. R., Reichle, R., Robertson, F. R., Ruddick, A. G., Sienkiewicz, M., and Woollen, J.: MERRA: NASA's Modern-Era Retrospective Analysis for Research and Applications, Journal of Climate, 24, 3624 – 3648, https://doi.org/10.1175/JCLI-D-11-00015.1, 2011.

Rißmann, M., Chen, J., Osterman, G., Zhao, X., Dietrich, F., Makowski, M., Hase, F., and Kiel, M.: Comparison of OCO-2 target observations to MUCCnet – is it possible to capture urban X_{CO_2} gradients from space?, Atmospheric Measurement Techniques, 15, 6605–6623, https://doi.org/10.5194/amt-15-6605-2022, 2022.

Rödenbeck, C., Zaehle, S., Keeling, R., and Heimann, M.: How does the terrestrial carbon exchange respond to inter-annual climatic variations? A quantification based on atmospheric CO_2 data, Biogeosciences, 15, 2481–2498, https://doi.org/10.5194/bg-15-2481-2018, 2018.

Rodgers, C. D.: Inverse Methods for Atmospheric Sounding: Theory and Practice, World Scientific Publishing Co. Pte. Ltd., 5 Toh Tuck Link, Singapore 596224, reprint edn., 2004.

Rosenberg, R., Maxwell, S., Johnson, B. C., Chapsky, L., Lee, R., and Pollock, R.: Preflight radiometric calibration of the Orbiting Carbon Observatory 2, Trans. Geosci. Remote Sensing, 55, 1994–2006, https://doi.org/10.1109/TGRS.2016.2634023, 2017.

Rosenberg, R., Chapsky, L., Crisp, D., Keller, G., Lee, R., Marchetti, Y., Yu, S., and Eldering, A.: OCO-2 Calibration Refinement Across Versions and Plans for OCO-3, in: IGARSS 2020 - 2020 IEEE International Geoscience and Remote Sensing Symposium, pp. 6381–6384, https://doi.org/10.1109/IGARSS39084.2020.9324511, 2020.

Roten, D., Lin, J. C., Kunik, L., Mallia, D., Wu, D., Oda, T., and Kort, E. A.: The Information Content of Dense Carbon Dioxide Measurements from Space: A High-Resolution Inversion Approach with Synthetic Data from the OCO-3 Instrument, Atmospheric Chemistry and Physics Discussions, 2022, 1–43, https://doi.org/10.5194/acp-2022-315, 2022.

Schaaf, C.: MODIS User Guide v006 and v006.1: MCD43A3 albedo product, Tech. rep., University of Massachusetts, Boston, https://www.umb.edu/spectralmass/terra_aqua_modis/v006/mcd43a3_albedo_product, last accessed May 8, 2023, 2022.

Shiomi, K., Kawakami, S., Ohyama, H., Arai, K., Okumura, H., Taura, C., Fukamachi, T., and Sakashita, M.: TCCON data from Saga, Japan, Release GGG2014R0, TCCON data archive, hosted by CaltechDATA, https://doi.org/10.14291/tccon.ggg2014.saga01.R0/1149283, 2014.

Sussmann, R. and Rettinger, M.: TCCON data from Garmisch (DE), Release GGG2014R2, TCCON data archive, hosted by CaltechDATA, https://doi.org/10.14291/TCCON.GGG2014.GARMISCH01.R2, 2018a.

Sussmann, R. and Rettinger, M.: TCCON data from Zugspitze (DE), Release GGG2014.R1, TCCON data archive, hosted by CaltechDATA, https://doi.org/10.14291/TCCON.GGG2014.ZUGSPITZE01.R1, 2018b.

Taylor, T. E., O'Dell, C. W., O'Brien, D. M., Kikuchi, N., Yokota, T., Nakajima, T. Y., Ishida, H., Crisp, D., and Nakajima, T.: Comparison of cloud-screening methods applied to GOSAT near-infrared spectra, 50, 295–309, https://doi.org/10.1109/TGRS.2011.2160270, 2012.

Taylor, T. E., O'Dell, C. W., Frankenberg, C., Partain, P. T., Cronk, H. Q., Savtchenko, A., Nelson, R. R., Rosenthal, E. J., Chang, A., Fisher, B. M., Osterman, G. B., Pollock, R. H., Crisp, D., Eldering, A., and Gunson, M. R.: Orbiting Carbon Observatory-2 (OCO-2) cloud screening algorithms: validation against collocated MODIS and CALIOP data, Atmospheric Measurement Techniques, 9, 973–989, https://doi.org/10.5194/amt-9-973-2016, 2016.

Taylor, T. E., Eldering, A., Merrelli, A., Kiel, M., Somkuti, P., Cheng, C., Rosenberg, R., Fisher, B., Crisp, D., Basilio, R., Bennett, M., Cervantes, D., Chang, A., Dang, L., Frankenberg, C., Haemmerle, V. R., Keller, G. R., Kurosu, T., Laughner, J. L., Lee, R., Marchetti, Y., Nelson, R. R., O'Dell, C. W., Osterman, G., Pavlick, R., Roehl, C., Schneider, R., Spiers, G., To, C., Wells, C., Wennberg, P. O., Yelamanchili, A., and Yu, S.: OCO-3 early mission operations and initial (vEarly) XCO_2 and SIF retrievals, Remote Sensing of Environment, 251, 112 032, https://doi.org/10.1016/j.rse.2020.112032, 2020.

Taylor, T. E., O'Dell, C. W., Crisp, D., Kuze, A., Lindqvist, H., Wennberg, P. O., Chatterjee, A., Gunson, M., Eldering, A., Fisher, B., Kiel, M., Nelson, R. R., Merrelli, A., Osterman, G., Chevallier, F., Palmer, P. I., Feng, L., Deutscher, N. M., Dubey, M. K., Feist, D. G., García, O. E., Griffith, D. W. T., Hase, F., Iraci, L. T., Kivi, R., Liu, C., De Mazière, M., Morino, I., Notholt, J., Oh, Y.-S., Ohyama, H., Pollard, D. F., Rettinger, M., Schneider, M., Roehl, C. M., Sha, M. K., Shiomi, K., Strong, K., Sussmann, R., Té, Y., Velazco, V. A., Vrekoussis, M., Warneke, T., and Wunch, D.: An 11-year record of XCO_2 estimates derived from GOSAT measurements using the NASA ACOS version 9 retrieval algorithm, Earth System Science Data, 14, 325–360, https://doi.org/10.5194/essd-14-325-2022, 2022.

TCCON: wiki page, Tech. rep., https://tccon-wiki.caltech.edu/Main/DataDescriptionGGG2020, "last accessed May 8, 2023".

Te, Y., Jeseck, P., and Janssen, C.: TCCON data from Paris (FR), Release GGG2014R0, TCCON data archive, hosted by CaltechDATA, https://doi.org/10.14291/tccon.ggg2014.paris01.R0/1149279, 2014.

Thuillier, G., Hersé, M., Labs, D., Foujols, T., Peetermans, W., Gillotay, D., Simon, P., and Mandel, H.: The Solar Spectral Irradiance from 200 to 2400 nm as Measured by the SOLSPEC Spectrometer from the Atlas and Eureca Missions, Solar Physics, 214, 1–22, https://doi.org/10.1023/A:1024048429145, 2003.

Toon, G. C.: Solar line list for GGG2014, Tech. rep., TCCON data archive, hosted by the carbon dioxide information analysis center, Oak Ridge National Laboratory, https://doi.org/10.14291/tccon.ggg2014.solar.R0/1221658, 2014.

Torii, S. and Marrocchesi, P. S.: The CALorimetric Electron Telescope (CALET) on the International Space Station, Advances in Space Research, 64, 2531–2537, https://doi.org/10.1016/j.asr.2019.04.013, 2019.

Torres, A. D., Keppel-Aleks, G., Doney, S. C., Fendrock, M., Luis, K., De Mazière, M., Hase, F., Petri, C., Pollard, D. F., Roehl, C. M., Sussmann, R., Velazco, V. A., Warneke, T., and Wunch, D.: A Geostatistical Framework for Quantifying the Imprint of Mesoscale Atmospheric Transport on Satellite Trace Gas Retrievals, Journal of Geophysical Research: Atmospheres, 124, 9773–9795, https://doi.org/10.1029/2018JD029933, 2019.

UoE: University of Edinburgh Atmospheric Composition Modelling Group Package for Observation System Simulation Experiments, https://www.geos.ed.ac.uk/~lfeng/, 2021.

Warneke, T., Messerschmidt, J., Notholt, J., Weinzierl, C., Deutscher, N. M., Petri, C., and Grupe, P.: TCCON data from Orléans (FR), Release GGG2014R1, TCCON data archive, hosted by CaltechDATA, https://doi.org/10.14291/TCCON.GGG2014.ORLEANS01.R1, 2014.

Weir, B., Ott, L. E., Collatz, G. J., Kawa, S. R., Poulter, B., Chatterjee, A., Oda, T., and Pawson, S.: Bias-correcting carbon fluxes derived from land-surface satellite data for retrospective and near-real-time assimilation systems, Atmospheric Chemistry and Physics, 21, 9609–9628, https://doi.org/10.5194/acp-21-9609-2021, 2021.

Wennberg, P. O., Wunch, D., Roehl, C., Blavier, J.-F., Toon, G. C., and Allen, N.: TCCON data from Caltech (US), Release GGG2014R1, TCCON data archive, hosted by CaltechDATA, https://doi.org/10.14291/tccon.ggg2014.pasadena01.R1/1182415, 2015.

Wennberg, P. O., Wunch, D., Roehl, C., Blavier, J.-F., Toon, G. C., Allen, N., Dowell, P., Teske, K., Martin, C., and Martin., J.: TCCON data from Lamont (US), Release GGG2014R1, TCCON data archive, hosted by CaltechDATA, https://doi.org/10.14291/tccon.ggg2014.lamont01.R1/1255070, 2016.

Wennberg, P. O., Roehl, C., Wunch, D., Toon, G. C., Blavier, J.-F., Washenfelder, R. a., Keppel-Aleks, G., Allen, N., and Ayers, J.: TCCON data from Park Falls (US), Release GGG2014R1, TCCON data archive, hosted by CaltechDATA, https://doi.org/10.14291/TCCON.GGG2014.PARKFALLS01.R1, 2017a.

Wennberg, P. O., Roehl, C. M., Blavier, J.-F., Wunch, D., and Allen, N. T.: TCCON data from Jet Propulsion Laboratory (US), 2011, Release GGG2014.R1, TCCON data archive, hosted by CaltechDATA, https://doi.org/10.14291/TCCON.GGG2014.JPL02.R1/1330096, 2017b.

Worden, J. R., Doran, G., Kulawik, S., Eldering, A., Crisp, D., Frankenberg, C., O'Dell, C., and Bowman, K.: Evaluation and attribution of OCO-2 XCO$_2$ uncertainties, Atmospheric Measurement Techniques, 10, 2759–2771, https://doi.org/10.5194/amt-10-2759-2017, 2017.

Wu, D., Liu, J., Wennberg, P. O., Palmer, P. I., Nelson, R. R., Kiel, M., and Eldering, A.: Towards sector-based attribution using intra-city variations in satellite-based emission ratios between CO$_2$ and CO, Atmospheric Chemistry and Physics, 22, 14547–14570, https://doi.org/10.5194/acp-22-14547-2022, 2022.

Wunch, D., Toon, G. C., Blavier, J.-F. L., Washenfelder, R. A., Notholt, J., Connor, B. J., Griffith, D. W. T., Sherlock, V., and Wennberg, P. O.: The Total Carbon Column Observing Network, Philosophical Transactions of the Royal Society A: Mathematical, Physical and Engineering Sciences, 369, https://doi.org/10.1098/rsta.2010.0240, 2011a.

1370   Wunch, D., Wennberg, P., Toon, G., Connor, B., Fisher, B., Osterman, G., Frankenberg, C., Mandrake, L., O'Dell, C., P.Ahonen, Biraud, S., Castano, R., Cressie, N., Crisp, D., Deutsher, N., Eldering, A., Fisher, M., Griffith, D., Gunson, M., Heikkinen, P., Keppel-Aleks, G., Kyro, E., Lindenmaier, R., Macatangay, R., Mendonca, J., Messerschmidt, J., Miller, C., Morino, I., Notholt, J., Oyafuso, F., Rettinger, M., Robinson, J., Roehl, C., Salawitch, R., Sherlock, V., Strong, K., Sussmann, R., Tanaka, T., Thompson, D., Uchino, O., Warneke, T., and Wofsy, S.: A method for evaluating bias in global measurements of CO_2 total columns from space, Atmospheric Chemistry and Physics,

1375   11, 12 317–12 337, https://doi.org/10.5194/acp-11-12317-2011, 2011b.

Wunch, D., Toon, G. C., Sherlock, V., Deutscher, N. M., Liu, C., Feist, D. G., and Wennberg, P. O.: Documentation for the 2014 TCCON Data Release, Tech. rep., CaltechDATA, https://doi.org/10.14291/TCCON.GGG2014.DOCUMENTATION.R0/1221662, 2015.

Wunch, D., Wennberg, P. O., Osterman, G., Fisher, B., Naylor, B., Roehl, C. M., O'Dell, C., Mandrake, L., Viatte, C., Kiel, M., Griffith, D. W. T., Deutscher, N. M., Velazco, V. A., Notholt, J., Warneke, T., Petri, C., De Maziere, M., Sha, M. K., Sussmann, R., Rettinger, M.,

1380   Pollard, D., Robinson, J., Morino, I., Uchino, O., Hase, F., Blumenstock, T., Feist, D. G., Arnold, S. G., Strong, K., Mendonca, J., Kivi, R., Heikkinen, P., Iraci, L., Podolske, J., Hillyard, P. W., Kawakami, S., Dubey, M. K., Parker, H. A., Sepulveda, E., García, O. E., Te, Y., Jeseck, P., Gunson, M. R., Crisp, D., and Eldering, A.: Comparisons of the Orbiting Carbon Observatory-2 (OCO-2) X_{CO_2} measurements with TCCON, Atmospheric Measurement Techniques, 10, 2209–2238, https://doi.org/10.5194/amt-10-2209-2017, 2017.

Wunch, D., Mendonca, J., Colebatch, O., Allen, N. T., Blavier, J.-F., Springett, S., Neufeld, G., Strong, K., Kessler, R., and Wor-

1385   thy, D.: TCCON data from East Trout Lake, SK (CA), Release GGG2014.R1, TCCON data archive, hosted by CaltechDATA, https://doi.org/10.14291/TCCON.GGG2014.EASTTROUTLAKE01.R1, 2018.

Xiao, J., Fisher, J. B., Hashimoto, H., Ichii, K., and Parazoo, N. C.: Emerging satellite observations for diurnal cycling of ecosystem processes, Nature Plants, 7, 877–887, https://doi.org/10.1038/s41477-021-00952-8, 2021.

Zhang, L. L., Yue, T. X., Wilson, J. P., Zhao, N., Zhao, Y. P., Du, Z. P., and Liu, Y.: A comparison of satellite observations with the XCO$_2$

1390   surface obtained by fusing TCCON measurements and GEOS-Chem model outputs, Science of The Total Environment, 601-602, 1575– 1590, https://doi.org/10.1016/j.scitotenv.2017.06.018, 2017.